UNIVERSITY OF CALIFORNIA SAN DIEGO

HIGH TEMPERATURE MATERIALS FOR THERMAL ENERGY STORAGE, CONVERSION AND MANAGEMENT

A dissertation submitted in partial satisfaction of the
requirements for the degree Doctor of Philosophy

in

Materials Science and Engineering

by

Ka Man Chung

Committee in charge:

Professor Renkun Chen, Chair
Professor Javier E. Garay
Professor Olivia A. Graeve
Professor Jian Luo
Professor Yu Qiao

2024

The Dissertation of Ka Man Chung is approved, and it is acceptable in quality and form for publication on microfilm and electronically.

University of California San Diego

2024

DEDICATION

To my love, Janet Cheung

TABLE OF CONTENTS

LIST OF FIGURES

LIST OF TABLES

ACKNOWLEDGEMENTS

First of all, I would like to take this opportunity to express my thankfulness and gratitude to my advisor, Prof. Renkun Chen. Not only his immeasurable support during my entire doctoral study at the University of California San Diego (UC San Diego), but his teaching and research philosophy have greatly influenced me, turning me into a wiser scientist in progress. He is a respectful role model for me who demonstrates how an excellent scientist, and a heartwarming educator, is. During my five-year doctoral journey, he has inspired me with countless intellectual conversations and creative ideas. It is my pleasure to learn and work with him. He always provides timely assistance and advice on every single aspect of my doctoral study. Without his constant support and advice, the dissertation and my research work would not have been possible.

I would like to express my thankfulness to my dissertation committee members who have provided me with tremendous guidance and research opportunities. Prof. Javier Garay has guided me through our collaborative work on molten salt thermal conductivity. His insightful interpretation of high-temperature measurements for fluids has been one of the important inspirations for my work. Prof. Olivia Graeve, the director of the program in Materials Science and Engineering, demonstrated excellent leadership and engagement in the program by creating various learning, research, and teaching opportunities. I was fortunate to be able to participate in ENLACE, a summer research program directed by Prof. Graeve, for multiple years to gain valuable mentoring and teaching experiences. I am thankful to have Prof. Jian Luo as one of my research collaborators. While working with him on projects about high-entropy ceramics and compositionally complex ceramics, I gained more sophisticated training in Materials Science research. It has broadened my understanding and interest in structure-property relationships of complex materials. I would like to thank Prof. Yu Qiao for his teaching in the course, Processing

of Polymers and Composites. His knowledge and understanding of polymers and composites have led me to a new Materials Science field that I was never familiar with before. That knowledge would be invaluable, providing me with a strong foundation for my future research.

Prof. Perry Li from the University of Arizona (UA), Prof. Peter Loutzenhiser from Georgia Institute of Technology (Georgia Tech), and Prof. Shang Zhai from the Ohio State University (OSU) have also been taking an important role in my research journey and have contributed to the research work presented in my thesis. Thanks to the collaboration with Prof. Li's group for realizing the first *in-situ* flowing molten salt measurement using our optical-based thermal characterization technique. Without the help of his team, this work would not have been successful. The collaborative work with Prof. Loutzenhiser's group was exciting. It always leads to novel and intriguing results that are beneficial to the solar-thermal energy research communities. Thank Prof. Zhai for his advice on thermochemical materials for sustainable fuel production. It motivates me to explore the possibility of designing high-entropy ceramics for better catalytic performance. I am also grateful for his research group's effort in testing our high-entropy ceramic samples.

I am sincerely thankful to receive the support and help from the TEMP lab's members. They include former members, Dr. Sahngki Hong, Dr. Elizabeth Rubin, Dr. Sunmi Shin, Dr. Yang Shi, Dr. Qingyang Wang, and Dr. Jian Zeng. They were my mentors when I was a new member at the TEMP lab, passing me experimental skills and knowledge in Heat Transfer and Thermal Science. In particular, I would like to show my gratitude to Dr. Jian Zeng. We have been working on the Gen 3 project for the past 5 years which has led to fruitful research results. It was a tough but rewarding journey when I always look back. I would also like to express my appreciation to the current members, including Tianshi Feng, Yu Pei, Sarath Adapa, and Xintong

Zhang. I am thankful to have my lab mates around to support each other and help maintain laboratory safety and operation.

Collaborators from other institutions and research groups are another driving force to make my research work complete. I would like to thank Drs. Ye Zhang and Xiaoxin Wang, former graduate research students at UA, for our collaborative work in molten salt measurements. Our day-to-night effort has yielded intriguing research output. I would like to thank Dr. Malavika Bagepalli for preparing pelletized ceramic particle samples for thermal diffusivity measurements. I would like to thank Nhu Nguyen from Georgia Tech for preparing thermochemical materials and sharing the materials characterization data. I would like to thank Drs. Clifford Ho and Kevin J Albrecht from Sandia National Laboratories (SNL) for helpful discussion on topics related to heat transfer in particle beds. I would like to thank Dr. Youyang Zhao from National Renewable Energy Laboratories (NREL) for providing salt samples. I also thank Drs. Zhiwen Ma and Patrick Davenport from NREL, and Dr. Megan Kirschmeier from Brayton Energy for sharing quartz sand samples for our study. I would like to thank Prof. Zhaowei Liu and Li Chen from UC San Diego for their help in obtaining the optical property data of our high-entropy spinel oxide samples.

Finally, I would like to thank my parents and families for their unlimited support and love while I was studying abroad. Their love and caring have turned into the fuel of my heart, motivating me to accomplish each seemingly impossible challenge one by one. I would like to share my joy with them.

The context of my dissertation includes my publications with my collaborators. Permissions are granted for including the publications in my dissertation.

Chapter 2 is a full reprint of **K. M. Chung**, T. Feng, J. Zeng, S. R. Adapa, X. Zhang, A. Z. Zhao, Y. Zhang, P. Li, Y. Zhao, J. E. Garay, and R. Chen. "Thermal Conductivity Measurement of Nitrate and Chloride Molten Salts Using Modulated Photothermal Radiometry " International Journal of Heat and Mass Transfer 217 (2023): 124652.

Chapter 3 is a full reprint of **K. M. Chung**, Y. Zhang, J. Zeng, F. Haddad, S. R. Adapa, T. Feng, P. Li, R. Chen. "*In-situ* Thermophysical Measurement of Flowing Molten Chloride Salt Using Modulated Photothermal Radiometry" Solar Energy 256 (2023): 112124.

Chapter 4 is currently being prepared for submission as **K. M. Chung**, N. P. Nguyen, S. R. Adapa, P. G. Loutzenhiser, R. Chen " *In-situ Thermal Conductivity Measurement Revealing Kinetics of Thermochemical Reactions* ". *in Prep.*

Chapter 5 is a full reprint of **K. M. Chung**, and R. Chen. "Black coating of quartz sand towards low-cost solar-absorbing and thermal energy storage material for concentrating solar power." Solar Energy 249 (2023): 98-106.

Chapter 6 is currently being prepared for submission as **K. M. Chung**, S. R. Adapa, L. Chen, J. Luo, Z. Liu, R. Chen. "Realizing Ultra-low Thermal Conductivity and Diffusivity at High Temperatures using Packed High-Entropy Spinel Oxide Nanoparticles". *in Prep*.

VITA

2016 Bachelor of Science, Chinese University of Hong Kong

2018 Master of Philosophy, Chinese University of Hong Kong

2024 Doctor of Philosophy, University of California San Diego

PUBLICATIONS

# These authors contributed equally to this work.

1. A.J. Wright, Q. Wang, S.T. Ko, **K.M. Chung**, R. Chen, and J. Luo. "Size disorder as a descriptor for predicting reduced thermal conductivity in medium-and high-entropy pyrochlore oxides." *Scripta Materialia* 181 (2020): 76-81.
2. J. Zeng#, **K. M. Chung#**, Q. Wang, X. Wang, Y. Pei, P. Li, and R. Chen. "Measurement of high temperature thermophysical properties of bulk and coatings using modulated photothermal radiometry." *International Journal of Heat and Mass Transfer* 170 (2021): 120989.
3. **K.M. Chung#**, J. Zeng#, S. R. Adapa, T. Feng, M. Bagepalli, P. G. Loutzenhiser, K. J. Albrecht, C.K. Ho, and R. Chen. "Measurement and analysis of thermal conductivity of ceramic particle beds for solar thermal energy storage." *Solar Energy Materials and Solar Cells* 230 (2021): 111271. # These authors contribute equally
4. J. Zeng#, **K. M. Chung#**, X. Zhang#, S. R. Adapa, T. Feng, Y. Pei, and R. Chen. "Thermal conductivity modelling of monodispersed microspheres using discrete element method." *Journal of Applied Physics* 130.16 (2021): 165104.
5. J. Zheng, Y. Kodera, X. Xu, S. Shin, **K. M. Chung**, T. Imai, R. Ihnfeldt, J. E. Garay, and R. Chen. "Suppressing thermal conductivity of nano-grained thermoelectric

material using acoustically hard nanoparticles." *Journal of Applied Physics* 130.23 (2021): 235106.

6. J. Zeng#, **K.M. Chung#**, S. R. Adapa, T. Feng, and R. Chen. "In-situ thermal transport measurement of flowing fluid using modulated photothermal radiometry." *International Journal of Heat and Mass Transfer* 180 (2021): 121767.
7. J. Zeng#, **K. M. Chung#**, X. Zhang, T. Feng, S. R. Adapa, and R. Chen. "Characterization and Understanding of Thermal Transport in Stationary and Moving Particle Beds for Concentrating Solar Power." *Annual Review of Heat Transfer* 25. (2022)
8. **K. M. Chung**, and R. Chen. "Black coating of quartz sand towards low-cost solar-absorbing and thermal energy storage material for concentrating solar power." *Solar Energy* 249 (2023): 98-106.
9. J. Zeng, X. Zhang, **K. M. Chung**, T. Feng, H. Zhang, R. S. Prasher, and R Chen. "Moisture thermal battery with autonomous water harvesting for passive electronics cooling." *Cell Reports Physical Science* (2023): 101250.
10. **K. M. Chung**, T. Feng, J. Zeng, S. R. Adapa, X. Zhang, A. Z. Zhao, Y. Zhang, P. Li, Y. Zhao, J. E. Garay, and R. Chen. "Thermal Conductivity Measurement of Nitrate and Chloride Molten Salts Using Modulated Photothermal Radiometry " *International Journal of Heat and Mass Transfer* 217 (2023): 124652.
11. **K. M. Chung#**, Y. Zhang#, J. Zeng, F. Haddad, S.R. Adapa, T. Feng, P. Li, R. Chen. "*In-situ* Thermophysical Measurement of Flowing Molten Chloride Salt Using Modulated Photothermal Radiometry" *Solar Energy* 256 (2023): 112124.

12. T. Feng, B. Pati, **K. M. Chung**, Y. Pei, R. Chen. "Ceramic-to-metal bonding using rare-earth containing Sn–Bi solder". *J Mater Sci: Mater Electron* **35**, 369 (2024).
13. X. Zhang, S. Adapa, T. Feng, J. Zeng, **K. M. Chung**, C. Ho, K. Albrecht, R. Chen. "Micromechanical Origin of Heat Transfer to Granular Flow". *Submitted*.
14. S. R. Adapa, X Zhang, T. Feng, **K. M. Chung**, K. J. Albrecht, C. K. Ho, D. A. Madden, R. Chen. "Thermophysical Properties and Heat Transfer Coefficients for Flowing Packed Particle Beds". *Submitted*.
15. A. J. Wright, **K. M. Chung**, Q. Wang, T. Feng, Y.T. Yeh, R. Chen, J. Luo. "Molten Chloride Salt Corrosion of Compositionally Complex Fluorite-Based Oxides". *In Prep*.
16. K. Song, D. Zhang, **K. M. Chung**, R. Chen, J. Luo. "Fluorite-Pyrochlore-Weberite Phase Transitions in a Series of 20-Component Ultrahigh-Entropy Compositionally Complex Ceramics". *in Prep.*
17. **K. M. Chung**, N. P. Nguyen, S. R. Adapa, P. G. Loutzenhiser, R. Chen "*In-situ* Thermal Conductivity Measurement Revealing Kinetics of Thermochemical Reactions ". *in Prep.*
18. **K. M. Chung**, S. R. Adapa, L. Chen, J. Luo, Z. Liu, R. Chen. "Realizing Ultra-low Thermal Conductivity and Diffusivity at High Temperatures using Packed High-Entropy Spinel Oxide Nanoparticles". *in Prep*.

ABSTRACT OF THE DISSERTATION

HIGH TEMPERATURE MATERIALS FOR THERMAL ENERGY STORAGE, CONVERSION AND MANAGEMENT

By

Ka Man Chung

Doctor of Philosophy in Materials Science and Engineering

University of California San Diego, 2024

Professor Renkun Chen, Chair

According to the Second Law of Thermodynamics, the Carnot engine gives the highest possible efficiency of a power cycle, which is defined as the ratio between the temperature difference between the hot reservoir and the cold reservoir and the hot reservoir temperature.

Operating a power cycle at high temperatures is the key to increasing the overall efficiency of a power plant. Concentrating solar power (CSP) is one of the emerging solar-thermal technologies that utilizes the collected concentrated sunlight for generating electricity with zero carbon emission. In the 3rd generation (Gen 3) CSP plants, the target operating temperature is at least 700 ^{o}C to achieve higher thermal efficiency and lower levelized cost of electricity (LCOE). In light of this, it is necessary to elucidate our fundamental understanding of the high-temperature materials being used in next-generation CSP plants, including HTFs, thermal energy storage (TES) materials, thermochemical materials, and thermal barrier materials. **Chapter 1** is a review of CSP technology and the current research opportunities and challenges at measurement and materials levels. **Chapter 2** presents the thermal conductivity measurement of molten salts, including molten nitrate and chloride salts, using novel optical-based thermal characterization, namely, modulated photothermal radiometry (MPR). **Chapter 3** presents the first *in-situ* thermal conductivity measurement for flowing molten salt using MPR. The relative thermal conductivity enhancement due to the forced convection and the heat transfer coefficient (HTC) of flowing molten salts are measured for the first time using MPR. **Chapter 4** presents the first *in-situ* monitoring of thermochemical reactions of hydroxides and perovskites using MPR. The thermal characterization results are correlated to the kinetics of the thermochemical reactions. **Chapter 5** presents the surface modification of quartz sand using black spinel oxide nanoparticles for low-cost solar-absorbing and TES applications. **Chapter 6** presents the realization of ultra-low thermal conductivity and diffusivity using high-entropy spinel oxide nanoparticles (HESO NPs) at high temperatures. **Chapter 7** is the conclusion and outlook of the dissertation, providing future research directions related to thermal evaluations of energy devices using non-contact

characterization techniques and the design of high-entropy ceramics (HECs) for catalytic, carbon capture, and thermal barrier applications.

Chapter 1. High temperature materials for CSP technology: opportunities and challenges

1.1. Overview of CSP technology

Human activities that involve fossil fuel consumption have generated extra greenhouse gases (GHGs), particularly carbon dioxide (CO_2). They accumulated in the atmosphere, leading to a gradual increase in the global surface temperature, namely global warming. According to the Intergovernmental Panel on Climate Change (IPCC) Sixth Assessment Report (AR6), the global average temperature has reached a record high temperature, 1.1 ^oC higher than preindustrial levels (*1*). To limit global warming to 1.5 ^oC, by 2030, the global CO_2 emission needs to be reduced by 48% based on the recorded emission levels in 2019.

To mitigate global warming, the deployment of different forms of zero-emission renewable energy is significantly important. Among different forms of renewable energy sources, solar energy is one of the promising options. First, solar energy is the most abundant resource on Earth. The Earth's surface receives around 360 x 10^{14} W per year, a number that is much larger than global annual power consumption (*2*, *3*). It implies that by capturing all available solar energy, in principle, the worldwide energy demand can be satisfied. Second, it is convenient to convert solar energy to other forms of energy for electricity generation. For instance, with the aid of photovoltaic materials, solar energy is converted to electricity by electro-hole pair creations; solar energy can also be stored in the form of thermal energy for later use.

Concentrating solar power (CSP) is one of the emerging solar-thermal technologies that can provide reliable and dispatchable electricity with zero carbon emission. In a CSP power, sunlight is collected and concentrated by an array of mirrors, namely, heliostats, for heating the

heat transfer fluids (HTFs) circulating in the power plants. The HTFs store the energy in the form of heat and then release the collected energy in a heat exchanger. The energy released is then transferred to other working circulating fluids for powering the turbine and generating electricity (**Figure 1.1**). CSP has shown technological success and has been commercialized for the realization of decarbonized energy production. The 1st generation CSP plants typically use oil or stream as the HTFs. They operate at 240- 440 ^{o}C with a power cycle efficiency of around 28- 38 % (*4*); the 2nd generation CSP plants were pushed to higher operating temperatures of up to 550 ^{o}C with the alternative of using molten salts as HTFs. A higher efficiency, thus, can be achieved (38- 44%) (*4*). It is worth mentioning that most of the 1st and 2nd CSP plants have no or limited thermal energy capability. It affects the reliability of CSP technology in providing a stable electricity supply when sunlight is not available (*5*, *6*).

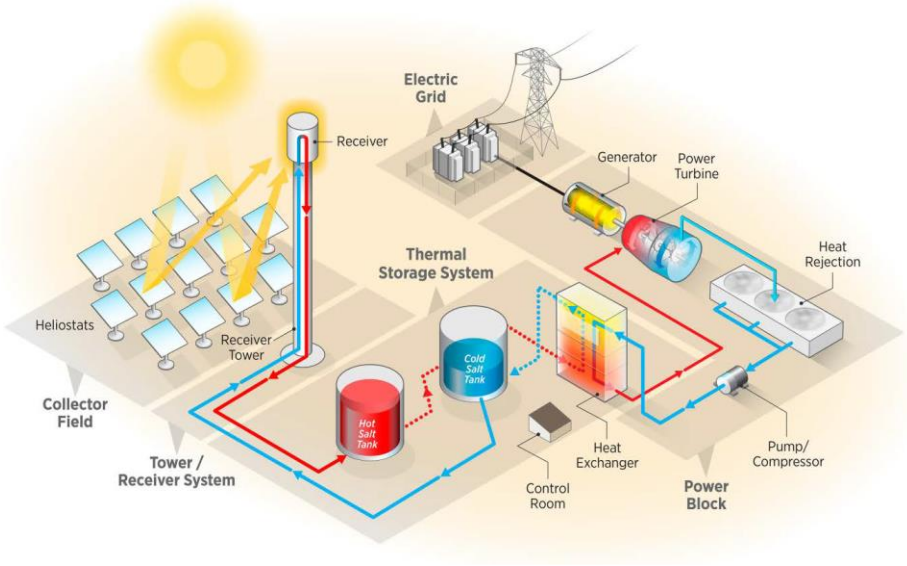

Figure 1.1 Illustration of a molten salt-based CSP plant (*7*)

According to the second law of thermodynamics, the efficiency of a power cycle can be increased by operating at higher temperatures. To further lower the levelized cost of electricity

(LCOE) ($ 0.05 per kWh or lower) by increasing the efficiency of the power cycle (> 50 %), the3rd generation (Gen 3) CSP plants aim to operate at least 700 ^{o}C or higher (*8, 9*). It is both exciting and challenging, mainly because of the technological barriers to the stability of materials at high temperatures and our unclear understanding of the material's properties at high temperatures. It is necessary to elucidate our fundamental understanding of the high-temperature sub-components at the CSP systems, including HTFs, thermal energy storage (TES) materials, thermochemical materials (TCMs), and thermal insulation materials (*10*). In the following section, we briefly discuss the research opportunities and challenges in each aspect.

1.2. High temperature HTFs

HTFs are one of the crucial sub-components in all thermal systems for transferring the collected energy, from a hot reservoir to a cold reservoir, via a heat exchange unit. The CSP community has been searching for ideal HTFs that have desirable properties, for example, high thermal conductivity, high stability, and low viscosity (*11*).

Air, water/stream, and thermal oils serve as HTFs in commercialized CSP plants. The advantages of using air as HTF are its abundance in the atmosphere and its wide operating temperature. Air and water/steam also have well-established thermophysical properties, enabling a relatively simplified power system design for generating electricity. However, both have their own disadvantages. Air has poor thermal transport properties, limiting its heat transfer performance even at high temperatures. Water/stream also has limited operating temperature below 300 ^{o}C (*11*). Thermal oils, such as XCELTHERM 600 © and Therminol VP-1, are commercialized thermal oils that provide promising heat transfer performance at elevated temperatures (300- 400 ^{o}C) with high thermal stability (*11*). Owing to their low thermal

conductivity and instability at high temperatures (> 500 ^{o}C), they are not compatible with 3rd CSP plants. There is an urge to look for next-generation HTFs.

Molten salts are identified as one of the next-generation HTFs because of their high thermal stability and promising thermophysical properties at high temperatures. The most common molten salt-based HTF is Solar Salt, a mixture of $NaNO_3$-KNO_3. It allows a maximum operating temperature of about 560 ^{o}C (*12, 13*). It enables high thermal efficiency of the CSP plants by increasing the operating temperature compared to air, water/stream, and oil-based CSP. In addition, molten salts provide the function of storing thermal energy in the form of latent heat, making them excellent next-generation HTFs and thermal energy storage materials for CSP application. While researchers are actively looking for molten salts, for example, molten chloride salts and fluoride salts, as the next-generation high-temperature HTFs for CSP and other thermal system applications, accurate thermal transport properties of molten salts, in general, are of little known. It is because of our incomprehensive understanding of thermal transport theory for liquids, as well as the lack of reliable molten salt thermal conductivity data (*14*). Molten salts are usually difficult and challenging to measure because of their corrosivity to the confinement materials, and the possible errors at high-temperature fluid measurements, including natural convection and radiation (*15-17*). It can be revealed from **Figure 1-2**, a summary plot of molten salt thermal conductivity of molten $NaNO_3$-KNO_3 from ref (*15*) which shows scattered thermal conductivity data of Solar Salt. To deepen our understanding of the thermal transport properties of molten salts and other high-temperature fluids, novel techniques and instruments must be developed for extracting more reliable thermophysical properties.

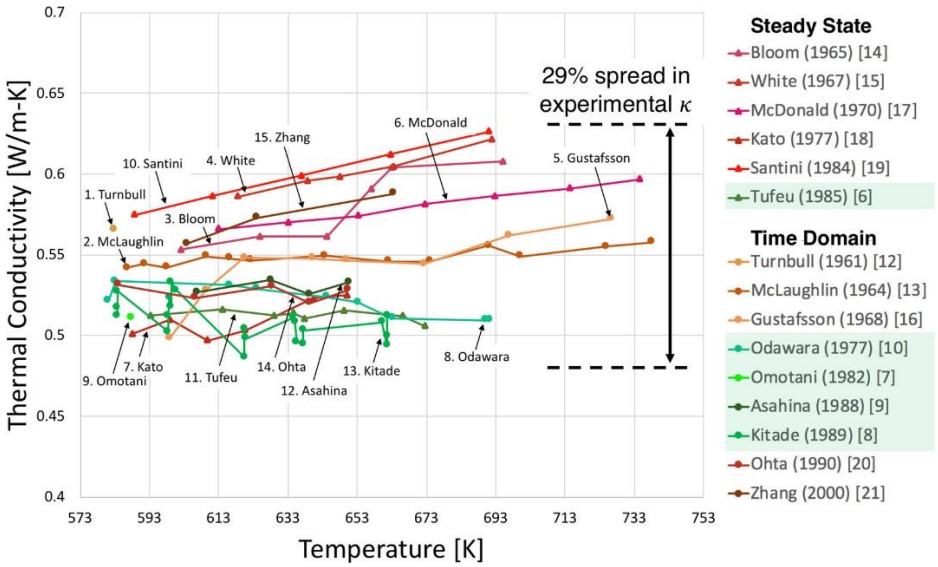

Figure 1.2 Summary of thermal conductivity data of Solar Salt (*15*)

1.3. Thermochemical materials for thermal energy storage and conversion

The next-generation CSP must be coupled with TES systems to enable a long-term reliable electricity supply. There are three pathways for TES, including sensible, latent, and thermochemical energy storage. While sensible heat and latent heat-based TES are more common because of their technological maturity, thermochemical energy storage has recently shown more momentum and potential to provide more efficient thermal energy storage capability (*18*). As shown in **Figure 1-3**, thermochemical energy storage through the formation and breakage of chemical bonding shows the highest energy density among all the other forms of TES (*19*).

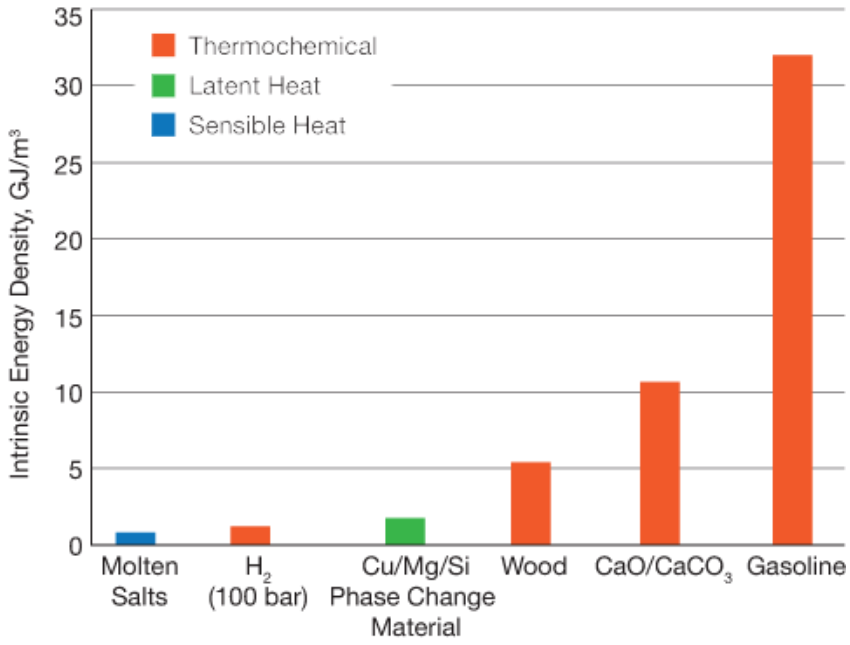

Figure 1.3 Summary of energy densities based on different types of TES materials (*19*)

Consider a reversible thermochemical reaction of AB, and the resultant products are A and B, the reaction can be expressed in the following formula:

$$AB + \Delta H_{reaction} \rightleftharpoons A + B \qquad (1.1)$$

The reactant AB absorbs the required thermochemical energy $\Delta H_{reaction}$ in charging mode, allowing the forward reaction from $AB \longrightarrow A + B$. The energy is stored in a form of thermochemical energy until there is a need to release $\Delta H_{reaction}$ during the discharging mode, from $A + B \longrightarrow AB$. In a perfect closed system, there is no heat loss to the surrounding environment during the charging and discharging, making it a more efficient thermal system. The state-of-the-art thermochemical materials (TCMs) for thermal energy storage applications are redox-active solid metal oxides (*20-24*), metal carbonates (*25*, *26*), and metal hydroxides (*25*, *27-30*). However, thermochemical-based TES is still beyond the stage for commercial scale due to technical immaturity. One of the major issues is the design of the thermal system for high

thermal efficiency (*27, 31, 32*). The lack of standard measurement techniques and reliable thermophysical property data of TCMs hinder the development and modeling study of the technology to a large and commercialized scale (*33*). Other than hand, by utilizing concentrated sunlight to provide thermal energy to trigger two-step or multiple-step thermochemical processes, value-added fuels can be generated. The process is called solar-thermochemical fuel production (*34*). The well-known solar-thermochemical fuel production examples are carbon dioxide dissociation (*35, 36*), water splitting (*35, 37, 38*), and ammonia production (*39*). Similar to the development of thermochemical-based TES technology, owing to the lack of understanding of the kinetics of thermochemical processes (i.e., rate limiting steps of thermochemical reactions) and the thermal transport properties of TCMs. Considering it, reliable high-throughput instruments are needed to truly capture both the reaction kinetics and the thermophysical properties of TCMs in their operating conditions.

1.4. Thermal insulation materials

Thermal insulation materials play a vital role in improving the thermal energy storage capability and the overall thermal efficiency of CSP plants by minimizing the heat loss of the thermal energy storage tank and other components of CSP plants, such as HTF pipes and solar receivers (*40-42*). To enable the functionality of minimizing heat loss without deterioration, promising thermal insulating materials have to possess ultra-low thermal conductivity at high temperatures and excellent resistivity to extreme conditions.

Conventionally, dense materials with intrinsic low thermal conductivity, such as refractory bricks, are the candidates. Although they are cheap and abundant, their thermal conductivity is still high at very high temperatures (*43*). Porous materials, such as aerogel,

fiberglass, and foam are other suitable candidates (*44*). The realization of low-thermal conductivity heavily relies on the introduction of porous structures to the insulation materials. However, at high temperatures, the thermal conductivity (or effective thermal conductivity) of the porous insulation materials inevitably increases because of the radiative thermal conduction (*40*, *44*). It limits the capability of insulation materials to protect insulated objects from thermal impacts under very extreme conditions.

Considering this, there is an urge to discover new materials that show transcendent materials properties to be the next generation of thermal insulation materials. Since 2015, high-entropy ceramics (HECs) have emerged as a new class of materials that show unique and excellent mechanical and thermal transport properties in the family of high-entropy materials (HEMs) (*45*). It was found that, by varying the key parameters, for example, size disorder of cations and compositional complexity, one can manipulate the thermal conductivity of HECs for optimal mechanical performance and thermal insulation ability (*46*). There is a great potential to apply HECs as the internal insulation for thermal energy storage systems, and infrastructures that confines high-temperature HTFs.

1.5. Summary and outlook

Based on the previous discussion, there are two levels of challenges hindering the development of next-generation CSP technology, and in general, high-temperature science and technology related to thermal energy storage, conversion, and thermal management. At measurement and instrumentation levels, there is an urgent need for innovative and reliable measurement tools for high-temperature materials. At materials levels, more sophisticated

materials design with desirable structure-property relationships is needed for high-temperature applications.

In the following chapters, I present my research work that can address the challenges of as mentioned beforehand. **Chapter 2** presents the thermal conductivity measurement of molten salts, including molten nitrate and chloride salts, using novel optical-based thermal characterization, namely, modulated photothermal radiometry (MPR). The MPR technique emerges as an innovative method to accurately capture the thermal conductivity of high-temperature molten salts with minimal measurement errors in all forms. **Chapter 3** presents the first *in-situ* thermal conductivity measurement for flowing molten salt using MPR. The relative thermal conductivity enhancement due to the forced convection and the heat transfer coefficient (HTC) of flowing molten salts are measured for the first time using MPR. It demonstrates the capability of the MPR technique as a real-time diagnostic tool of high-temperature flowing fluids. **Chapter 4** presents the first *in-situ* monitoring of thermochemical reactions of hydroxides and perovskites using MPR. The thermal characterization results are correlated to the kinetics of the thermochemical reactions. It would be useful for both industrial and research communities to monitor the kinetics of thermochemical reactions using a non-invasive tool in real-time. **Chapter 5** presents the surface modification of quartz sand using black spinel oxide nanoparticles for low-cost solar-absorbing and TES applications. It provides a cost-effective alternative for TES and heat transfer media for CSP applications. **Chapter 6** presents the realization of ultra-low thermal conductivity and diffusivity using high-entropy spinel oxide nanoparticles (HESO NPs) at high temperatures. It combines the novelty of high-entropy materials and the unique heat transfer in nano-constriction to realize ultra-low thermal conductivity and diffusivity at high temperatures under ambient environments. **Chapter 7** is the conclusion and outlook of the dissertation,

providing future research directions related to thermal evaluations of energy devices using non-contact characterization techniques and the design of HECs for catalytic, carbon capture, and thermal barrier applications.

Chapter 2. Thermal conductivity measurement of nitrate and chloride molten salts using modulated photothermal radiometry

2.1. Introduction

Molten salts are an important class of heat transfer fluids (HTFs) in high-temperature thermal energy systems including concentrating solar power (CSP), nuclear power plants, and thermal energy storage (TES). Solar salt ($NaNO_3$–KNO_3 mixture with wt.% 60–40) is being used in the state-of-the-art CSP plants with TES capability at temperatures up to 550 ^oC (*47, 48*). Eutectic chloride salts with stability above 800 ^oC are being evaluated for next-generation CSP plants operating at high temperatures for higher energy conversion efficiency (*4, 49, 50*). In these cases, molten salts are used as both the HTFs collecting the concentrated solar heat and as high-temperature TES media. Molten fluoride salts have gained great attention in the development of generation-IV nuclear power plants as nuclear reactor coolants (*51, 52*). These salts, such as LiF–BeF_2 and LiF–NaF–KF, have high thermal stability, satisfactory specific heat and thermal conductivity at temperatures higher than 700 ^oC (*53, 54*), thus making them well suited for molten salt reactors (MSRs).

Thermal conductivity of molten salts is important for the performance and cost of these systems. For instance, the thermal conductivity of molten salts dictates the size and thus the cost of molten salt-steam heat exchangers in a CSP power plant. However, reliable thermal conductivity data of molten salts are difficult to obtain. Even common nitrate salts have shown large discrepancies as reported in the literature. For example, there is around ~ 40 % difference among the reported thermal conductivity values for the solar salt (*55*), despite its widespread use in commercial CSP plants. Reliable data on the emerging high temperature chloride salts are

even more scarce. Molten salts are difficult to measure using conventional contact methods because of their corrosive and conductive nature (*15, 17*). In the commonly used transient hot-wire (THW) method, an electrically insulated and corrosion-resistant coating is needed for metallic hot wires (*56, 57*), which complicates the sample preparation process. The corrosion-resistant coating can only slow down and minimize the corrosion effect. However, the hot wires and sensors would eventually be damaged, leading to measurement errors. In steady state methods, natural convection could introduce substantial errors when there is a large molten salt volume contained in test sections (*15, 17, 58-60*). The transient thermal signals in both the steady state and THW methods could also be highly influenced by the ambient temperature fluctuations. Radiative heat loss could affect the thermal conductivity measurements in the steady state techniques as well (*61*). Recently, laser flash analysis (LFA) is becoming increasingly popular for molten salts measurements due to its non-contact nature and ease of operation. However, LFA data on molten salts have also witnessed large scattering, due to many factors including the salt creeping effect (*62, 63*). When the creeping occurs, salts tend to form precipitates on the wall of crucibles used to hold the molten salts, leading to uneven thickness of the molten salt layer in the crucible and large uncertainty in the LFA data. The time domain nature of the LFA also makes it susceptible to convection and radiation heat loss from the crucible at high temperature, especially if the time window used for data fitting is not properly chosen (*64-67*). Zhao *et al.* (*15*) recently developed a frequency-domain hot-wire technique for measuring molten nitrate salts. The thermal penetration depth of the modulated heating power on the hot wires is confined to about 100 mm within the molten salt volume to minimize the convection and other heat loss effects. Their thermal conductivity results of molten nitrate salts are ~11 to 15 % higher than the existing reference values obtained from conventional steady state and time domain measurements,

including the THW and LFA methods. Their results show more reasonable temperature dependence of thermal conductivity compared to previously reported values and are consistent with their predictions by a phonon gas model for dense and strongly interacting liquids (*68*). This study demonstrates the value of frequency-domain technique for obtaining accurate results. Nevertheless, the use of a hot wire makes it less convenient, especially for corrosive high-temperature chloride salts.

Recently, we have developed a non-contact modulated photothermal radiometry (MPR) technique to measure bulk solids and coatings at high temperatures (*69, 70*). It is a front side sensing photothermal radiometry in which the oscillating thermal emission induced by an intensity-modulated heating laser is utilized for thermometry. The technique was further applied to the measurements of stationary and flowing HTFs such as water and thermal oil up to ~170 ^{o}C (*70*). In this work, it is applied for molten salt measurements for the first time. A special molten salt holder with a vertical configuration is designed for the MPR setup to address several issues in the LFA, in particular, the salt creeping effect. Measurement errors due to the natural convection effect can be minimized in the MPR method by carefully controlling thermal penetration depth into the molten salt layers. With this new technique, the thermal conductivity of molten nitrate and chloride salts up to 700 ^{o}C, with less than 10 % uncertainty is obtained. The selected molten salts for measurements include pure nitrate salts ($NaNO_3$ and KNO_3), solar salt ($NaNO_3$–KNO_3 mixture) and ternary chloride salt (NaCl–KCl–$MgCl_2$). The measured data are also compared with the values from the LFA, and other techniques reported in the literature. Our results demonstrate the reliability of the MPR method for measuring thermal conductivity of molten salts. Therefore, the MPR technique can serve as a useful and convenient tool to obtain accurate thermophysical properties of molten salts.

2.2. Experimental procedure

2.2.1. MPR Setup

Figure 2.1 shows the principle of the MPR measurement and the schematic of the molten salt holder in the MPR setup. The photographs of the setup are shown in **Figure 2.2**. A continuous-wave laser with its intensity modulated at an angular frequency ω ($q(t) = q_s e^{j\omega t}$) is heating the front surface of the sample holder. The temperature response of the same surface is measured using a high-speed infrared (IR) detector. The MPR setup is the same as in our earlier work (*69, 70*). The laser profile is converted from Gaussian to a top-hat (uniform) using a homogenizer. The diameter of the uniform intensity portion of the laser beam is about 15 mm. In this work, we used either a liquid-nitrogen-cooled Hg-Cd-Te (MCT) detector (Kolmar Technologies, Inc., KMPV11-0.25-J1/DC70, 62 ns response time) or an uncooled PbSe detector (Thorlabs, PDA20H-EC, 34 ms response time). The IR detection area is about 0.5 mm and 2 mm respectively for these two detectors. The voltage reading from either detector is converted to temperature through a calibration using a pyrometer (Lumasense Technologies IGA 320/23- LO). We confirmed that both detectors yielded equivalent results when using their respective calibration curves. The heat flux q_s in the measurements is calibrated by using a known reference sample. Borosilicate glass is chosen as the reference sample because it has well-known and stable thermophysical properties (*71, 72*). The c_p of molten salts is additionally verified by us using differential scanning calorimetry (DSC). For each temperature point, the measurement takes about 20 minutes, as a sufficiently long data collection time was used to reduce the noise at each frequency point within the frequency range (e.g., 0.1 to 10 Hz).

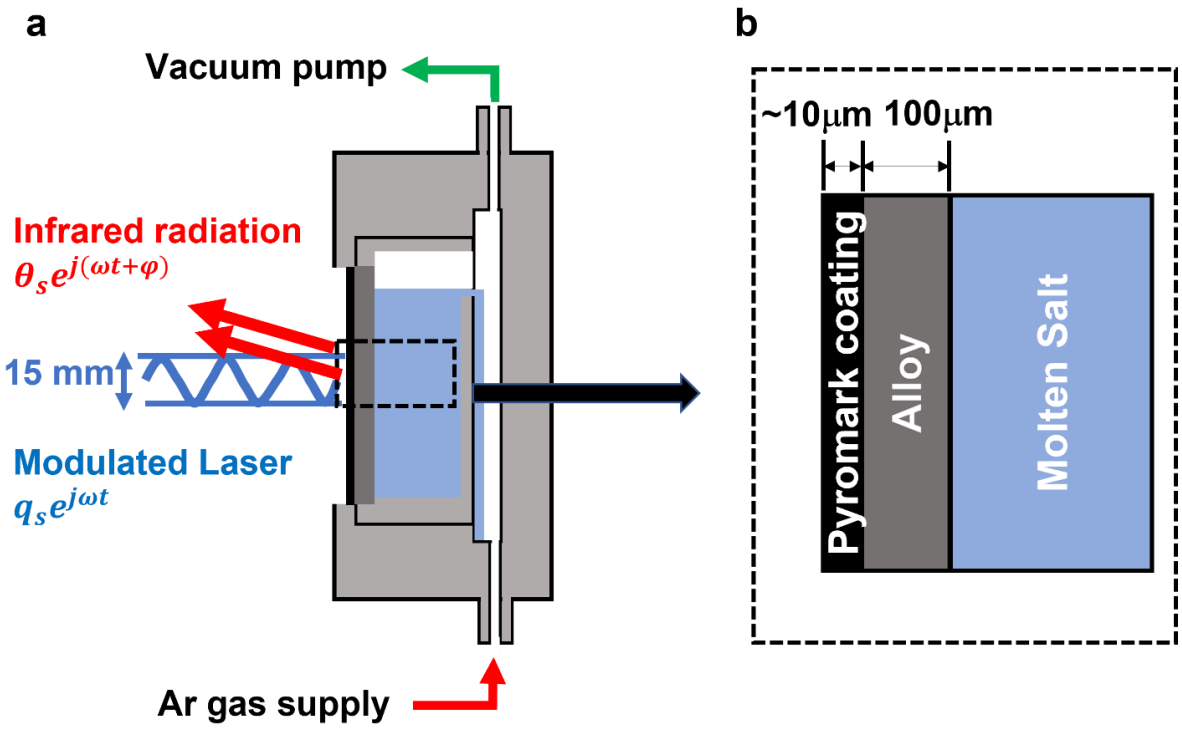

Figure 2.1 Schematics of the MPR molten salt measurement. **(a)** In the MPR measurement, the molten salt holder is vertically positioned. The thermal response from the front side of the molten salt holder is detected. The small cavity on the backside of the holder allows the overflow of the molten salt; **(b)** the three-layer structure formed by the molten salt, Inconel 625 cover and the Pyromark coating used for the heat transfer model in MPR.

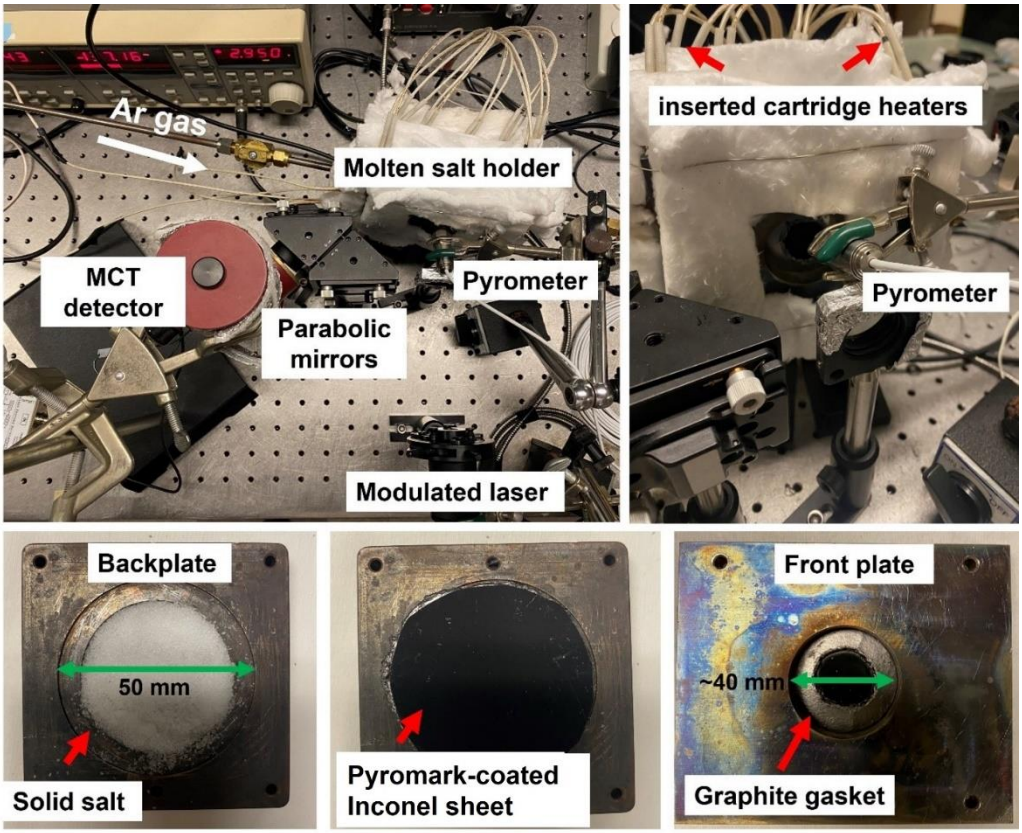

Figure 2.2 Photographs showing the MPR experimental setup and the salt loading process

A special MPR holder is custom-made for molten salt measurements at high temperatures (up to ~700 ^{o}C). The design is beneficial for front side sensing and vertical configuration. The vertical configuration can eliminate the salt creeping effect which is one of the challenging issues commonly observed in molten salt thermophysical property measurement. A detailed discussion of the benefits of the molten salt holder design and the comparison of the MPR method to the other measurement techniques will be discussed in *section 2.4*. The holder contains three main components: an Inconel 625 backplate with a small cavity on the front side and a larger cavity on the backside, a thin (100 μm thick) Inconel 625 sheet covering the salt, and an Inconel front plate with a middle opening that secures the Inconel 625 cover to the Inconel backplate with screws. The front cavity within the backplate has a depth of ~ 3 mm and a diameter of 50 mm and it is

used for holding the salt during the measurements. Inconel was selected as the holder material because it is a corrosion-resistant containment material. The back cavity in the backplate is connected to Argon (Ar) gas flow and a vacuum pump. There is a small hole around the top edge connecting the two cavities, which allows the gas to flow to the front cavity and overflow of molten salt to the back cavity. Purging Ar gas throughout the measurement enables the salt samples to be free of oxygen and moisture contamination. The backplate contains inserted cartridge heaters to reach the measurement temperature. The front plate has an opening of ~ 40 mm-diameter in the middle for optical access to the Inconel 625 cover. The front surface of the Inconel 625 cover is coated with a thin (~ 10-15 μm) layer of a high-temperature black coating made of Pyromark 2500 for laser photothermal absorption and thermal emission (*69*). The back side of the Inconel 625 cover (in contact with the molten salt) is coated with a 200 nm thick Pt layer to avoid possible corrosion by the salts. Graphite gaskets, serving as mechanical seals, are inserted between the front and back plates.

2.2.2. Heat transfer model and data fitting

In the MPR measurement, the molten salt, Inconel 625 cover, and the Pyromark coating form a three-layer structure (**Figure 2.1b**). The intensity-modulated continuous laser serves as periodic heat flux and is applied on the top surface of the three-layer structure. Since the laser heating spot size (~ 15 mm) is much larger than the sample thickness (~ 3 mm) or the thermal penetration depth (< 2 mm) within the modulation frequency used in this study, we can assume the heat transfer is one-dimensional (1D). The 1D heat transfer model for a multi-layer sample with a heat flux imposed on the top surface is given by (*69, 70*),

$$\begin{bmatrix}\theta_b \\ q_b\end{bmatrix} = M_n M_{n-1} \cdots M_i \cdots M_1 \begin{bmatrix}\theta_s \\ q_s\end{bmatrix} = \begin{bmatrix}a(i\omega) & b(i\omega) \\ c(i\omega) & d(i\omega)\end{bmatrix}\begin{bmatrix}\theta_s \\ q_s\end{bmatrix} \quad (2.1)$$

where θ_s and q_s are the surface temperature oscillation and the heat flux on the top surface, respectively. θ_b and q_b, on the other hand, are the temperature oscillation and the heat flux on the bottom layer, respectively. The transfer matrix M_i is given by:

$$M_i = \begin{bmatrix} \cosh(D_i\sqrt{j\omega}) & -\frac{\sinh(D_i\sqrt{j\omega})}{e_i\sqrt{j\omega}} \\ -e_i\sqrt{j\omega}\sinh(D_i\sqrt{j\omega}) & \cosh(D_i\sqrt{j\omega}) \end{bmatrix} \quad (2.2)$$

where $D_i = \frac{l_i}{\sqrt{\alpha_i}}$, l_i and α_i are the thickness and the thermal diffusivity of the i th layer respectively; e_i is the thermal effusivity of the i th layer, defined as $e_i = \sqrt{\rho_i c_{pi} k_i}$, where ρ_i, $c_{pi}$and k_i are the density, specific heat capacity and thermal conductivity of the i th layer. In the current three-layer case, the 1st, 2 nd and, 3 rd layer are the Pyromark coating, Inconel 625 sheet, and the molten salt layer, respectively. $a(i\omega)$, $b(i\omega)$, $c(i\omega)$, and $d(i\omega)$ are the matrix elements of the lumped transfer matrix. With the adiabatic boundary conditions, Eq. (2.1) is simplified as:

$$q_b = c(i\omega)\theta_s + d(i\omega)q_s = 0 \quad (2.3)$$

At a low angular frequency, the thermal penetration depth ($\delta_p = \sqrt{\frac{2k}{\rho c_p \omega}}$) is long enough to probe into the molten salt layer. The thermal response from the sample is mainly determined by the thermophysical properties of the molten salt layer. When the angular frequency increases, the thermal penetration depth is shortened. It allows us to probe into the layers that are closer to the top surface, which corresponds to the Inconel 625 cover and the Pyromark coating. The thermal response from the sample is then determined by the thermophysical properties of the alloy and the coating.

The heat loss due to the radiative heat transfer from the laser window is considered in our model. The surface temperature T_s at the laser window is the sum of a D.C. component and an

A.C. component of the temperature, $T_s = T_{DC} + \theta_s$, where T_{DC} is the mean surface temperature. The radiation heat loss thus can be decomposed into the D.C. and A.C. components of radiation heat loss. The D.C. component is defined as

$$q_{loss,DC} = \varepsilon\sigma(T_{DC}^4 - T_0^4) \tag{2.4}$$

where ε and σ are the emissivity of the laser window and the Stefan–Boltzmann constant. T_0 is the ambient temperature (20 ^{o}C). The A.C. component can be approximated as:

$$q_{loss,AC} \approx 4\varepsilon\sigma T_{DC}^3\theta_s \tag{2.5}$$

Considering the heat loss through thermal radiation, Eq. (2.3) is further modified by including the radiative heat flux:

$$c(i\omega)\theta_s + d(i\omega)(q_s - q_{loss,AC}) = 0 \tag{2.6}$$

An iterative process is introduced to extract the exact radiation heat loss, as shown in **Figure 2.3a**. Initially, temperature oscillation $\theta_{s,0}$ based on Eq. (2.3) with a known q_s is applied to estimate radiation heat loss in Eq. (2.5). Considering the radiation heat loss at top surface, the net heat flux flowing into the multi-layer structure needs to be modified by subtracting radiation heat loss from q_s at top surface, as instructed in Eq. (2.6). Based on Eq. (2.6), $\theta_{s,1}$ for the next round iteration can be estimated. Within each iteration step i, the difference in $\theta_{s,i}$ and $\theta_{s,i+1}$ between two consecutive steps is monitored. Once the difference is less than a tolerance, e, the radiation heat loss and temperature oscillation, $\theta_{s,end}$, in the last step will be considered as an accurate solution. The surface temperature oscillation amplitude with radiation heat loss can therefore be estimated by the iteration using Eq. (2.6).

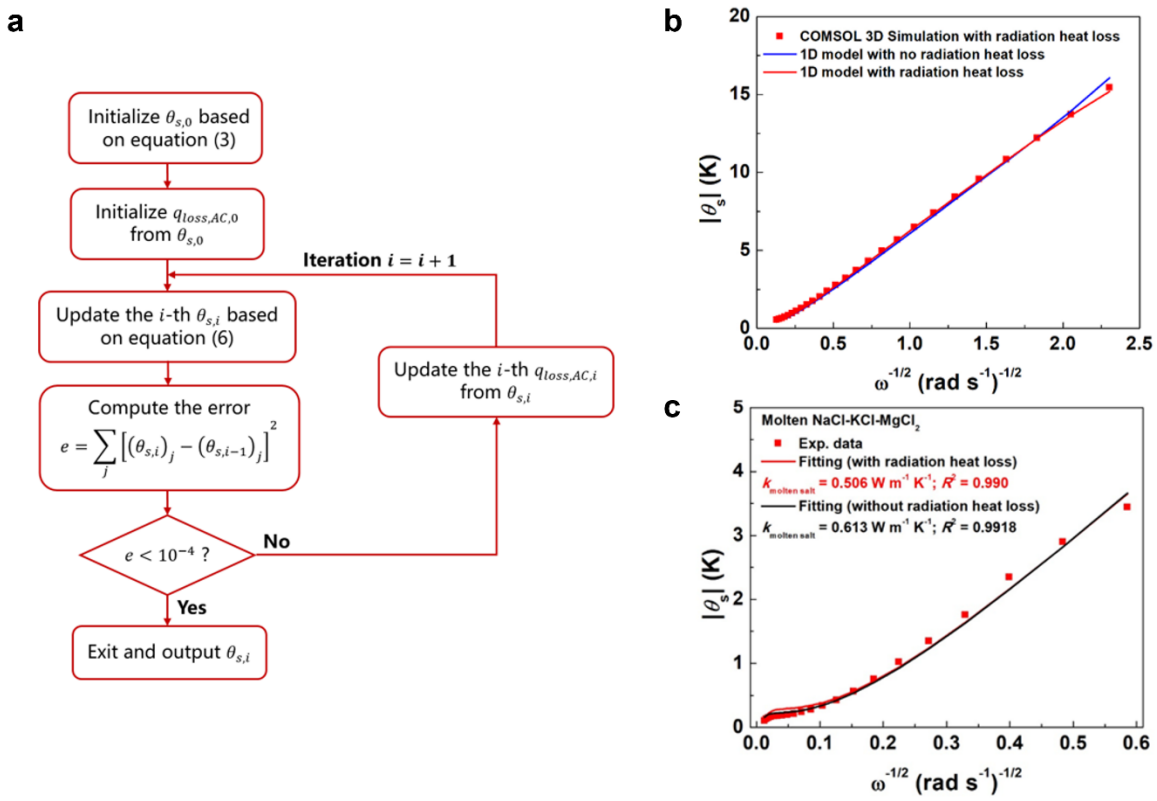

Figure 2.3 (**a**) Iterative process of radiation loss in 1D MPR analytical model. **(b)** COMSOL simulation of the MPR experimental data compared with the 1-D three-layer model fitting results with and without radiation heat loss, for a molten salt with its holder shown in Fig. 2.1b. **(c)** Fitting to the MPR experimental data of $|\theta_s|$ *vs.* $\omega^{-\frac{1}{2}}$ of molten NaCl–KCl–$MgCl_2$ at 450 °C. The model-fitted results with and without radiation heat loss are plotted alongside for comparison. If the radiation heat loss was not considered, the fitting result would considerably overestimate the molten salt thermal conductivity (0.613 *vs.* 0.506 W m^{-1} K^{-1}).

Without considering the radiation heat loss, the fitting result using Eq. (2.3) would overestimate the best-fitted thermal conductivity of molten salts. To illustrate this, MPR experimental data results were simulated using a 3D finite element model FEM using COMSOL to compare the 1D model fitting results with and without radiation heat loss with a sample temperature of 450 °C. **Figure 2.3b** shows that the 1D analytical model with the radiation heat loss have excellent agreement with the 3D FEM model, whereas the 1D analytical model without considering the radiation heat loss predicts a higher surface temperature rise at low frequency (to the right of the *x*-axis). This is because the radiation heat loss at this temperature is not negligible

relative to the conduction heat transfer into the molten salt (a low thermal conductivity material) when the thermal penetration depth is long. The model fitting results of molten NaCl–KCl–$MgCl_2$ at 450 ^oC with and without considering the radiation heat loss were also compared (**Figure 2.3c**). The comparison shows that while both models can fit the data where, the model without considering the radiation heat loss overestimated the molten salt thermal conductivity by about 20 % (0.613 *vs.* 0.506 W m^{-1} K^{-1}). Therefore, it can be concluded that radiation heat loss needs to be included in the model when measuring low thermal conductivity materials at high temperatures.

In this work, the MPR experimental data were fitted with the analytical model shown in Eq. (2.6). Levenberg-Marquardt method was selected as the fitting method. It is a general approach for solving inverse heat transfer problems (*73*). The thermal conductivity of molten salt (k) is the unknown to be estimated in this method and will be solved iteratively by an optimization algorithm. The thermophysical property of the 1st and the 2nd layers (i.e., Pyromark coating and Inconel 625), including ρ, c_p, and k are the known input parameters. They can be found in refs (*69, 74*). For the 3rd layer (i.e., paraffin wax, molten sulfur, and molten salts), ρ and c_p are the known input parameters from refs (*12, 75-77*). The thermal conductivity of molten salt k is set as the fitting parameter. The aim of the method is to minimize the following least squares equation:

$$S = \sum_{i=1}^{N} (\theta_{s_{exp-i}} - \theta_{s_{sim-i}})^2 \quad (2.7)$$

where $\theta_{s_{exp-i}}$ is the measured surface temperature oscillation at a frequency point and $\theta_{s_{sim-i}}$ is the simulated surface temperature oscillation based on the known parameters and the initial

guess value of the thermal conductivity. The iterative fitting algorithm is based on the following equation (2.8-2.9):

$$P^{n+1} = P^n + ((J^n)^{Tr}J^n + \mu^n\Omega^n)^{-1}(J^n)^{Tr}(\theta_{s_{exp}} - \theta_{s_{sim}}(P^n)) \quad (2.8)$$

$$\Omega^n = diag[(J^n)^{Tr}J^n] \quad (2.9)$$

where P is the fitting parameters (k of molten salt here), J is the Jacobin Matrix of fitted parameters, μ is the damping factor, and n indicates the iteration step. The iteration would stop and output the optimal value when the error S is smaller than the specified error allowance, 1^{-4}. More details about the iterative algorithm could be found elsewhere (*78*).

2.2.3. Sample preparation and loading

Two phase change materials (PCMs), namely, paraffin wax and sulfur, with established thermophysical properties were measured for calibration purpose. Paraffin wax (melting point of 53-58 °C, CAS no. 8002-74-2) was purchased from Sigma-Aldrich and sulfur (-325 mesh, purity ≥ 99.5 %, CAS no. 7704-34-9) from Spectrum. Three nitrate salts and one chloride salt were measured: $NaNO_3$, KNO_3, Solar salt ($NaNO_3$–KNO_3 mixture with wt.% 60–40), and NaCl–KCl–$MgCl_2$. $NaNO_3$ (purity ≥ 99 %, CAS reg. no. 7631-99-4) and KNO_3 (purity ≥ 99 %, CAS reg. no. 7757-79-1) were obtained from Sigma-Aldrich and used as the precursors of the solar salt. The solar salt was prepared by mixing the two pure nitrate salts based on the specified weight ratio. The salt mixture was melted and mixed repeatably in a clean glass crucible heated by a hot plate to ensure the uniformity of the composition. The entire procedure was performed inside a glovebox with < 0.5 ppm oxygen level. For the chloride salt, NaCl–KCl–$MgCl_2$ was prepared by NREL according to the published protocol (ref (*75*)). **Table 2.1** summarizes the molten salts measured in this work.

Table 2.1 Summary of molten salts measured in this work

Sample No.	Salt Composition	Reported melting point (°C) (*12, 75*)	Measured melting point (°C)
1	$NaNO_3$ (>99 %)	308	-
2	KNO_3 (>99 %)	334	-
3	$NaNO_3$–KNO_3 (wt.% 60–40)	220	225
4	NaCl–KCl–$MgCl_2$ (wt.% 15.11–38.91–45.98)	401	401

Right before an MPR measurement, a solid salt was transferred from the glovebox and loaded to the MPR holder under ambident condition. The salt was then covered by the Pyromark-coated Inconel sheet, which was further anchored to the bottom plate with the top plate using screws and the graphite gaskets sealing. The holder was then connected with the vacuum pump and flowing Ar gas. The salt was purged with flowing Ar gas at a temperature about 50 °C higher than its melting point for one hour to thoroughly remove the moisture that might have been introduced during the salt loading process. Afterward, the measurement started from slightly above the melting points with temperature increment of 25 or 50 °C until the highest measurement temperature was reached. During the measurements, the salt-filled cavity was also continuously purged with the Ar gas. A gaseous pressure of 780 Torr, slightly above the atmospheric pressure, was maintained throughout the measurement.

The systematic errors could come from the uncertainty in the instruments (IR detector, lock-in amplifier, etc), uncertainty of laser heat flux, the calibration curve converting the IR detection voltage to temperature. Specific to molten salt or other liquid measurements, there could be errors introduced by the natural convection effect. For the heat flux, we used a standard

reference sample (borosilicate glass) to calibrate the heat flux, which is proportional to the thermal effusivity of the reference sample. The uncertainties due to the heat flux and the instruments were determined to be ~ 6 % in our earlier work (*69, 70*). The natural convection effect could occur when the thermal penetration depth (δ_p) is large enough, leading to a high Rayleigh number (Ra) and a Nusselt number (Nu) much higher than 1. Rayleigh number is defined as $Ra = \frac{\beta \Delta T g \delta_p^3}{\nu \alpha}$, where β is the thermal expansion coefficient of the fluid, α is the thermal diffusivity of the fluid, ν is the kinematic viscosity of the fluid g is the gravitational constant, ΔT is the characteristic temperature rise (AC amplitude) during the measurements. Here, we can modulate the frequency of the laser intensity to control the thermal penetration depth ($\delta_p = \sqrt{\frac{\alpha}{\pi f}}$) such that Nu is close to one (i.e., $Nu \cong 1$) to have negligible natural convection effect. Based on the natural convection analysis of fluids in a vertical enclosure (*79*), the average Nusselt number of a vertical plate with a gap spacing L is given by:

$$\overline{Nu_L} = \max\{Nu_1, Nu_2, Nu_3\} \tag{2.10}$$

$$Nu_1 = 0.0605 {Ra_L}^{\frac{1}{3}}$$

$$Nu_2 = \left\{ 1 + \left[\frac{0.104 {Ra_L}^{0.293}}{1 + \left(\frac{6310}{Ra_L} \right)^{1.36}} \right]^3 \right\}^{\frac{1}{3}}$$

$$Nu_3 = 0.242 \left(\frac{Ra_L}{\frac{H}{L}} \right)^{0.272};$$

where H is the height of the enclosure, and the average Rayleigh number Ra_L is given by $Ra_L = \frac{\rho g \beta (\Delta T) L^3}{\mu \alpha}$, where β is the thermal expansion coefficient of the fluid, α is the thermal diffusivity

of the fluid, ν is the kinematic viscosity of the fluid g is the gravitational constant, ΔT is the characteristic temperature rise (AC amplitude) during the measurements. Equation (S1) is valid for $10^3 < Ra_L < 10^7$. When $Nu_L \cong 1$, the heat conduction from the wall to the fluid is purely conduction and the natural convection effect is negligible. **Table 2.2** shows the cutoff frequency for each fluid measured in this work.

Table 2.2 Summary of the thermophysical properties of each fluid, the cutoff frequency f for the measurement and the corresponding estimated thermal penetration depth δ_p. The thermophysical properties are extracted from ref (*76, 80-82*) for paraffin wax; ref (*77, 83-85*) for sulfur; ref (*12, 86*) for $NaNO_3$, KNO_3 and the solar salt; and ref (*63, 75, 87*) for NaCl–KCl–$MgCl_2$

Fluid	T (°C)	ρ (kg m^{-3})	C_p (J kg^{-1}K^{-1})	β (10^{-4} K^{-1})	μ (Pa.s)	Estimated k (W m^{-1} K^{-1})	δ_p and f when $Nu_L \cong 1$	
							δ_p (mm)	f (Hz)
Paraffin wax	100	760	2510	2.04	2.50×10^{-3}	0.200	0.268	0.46
Sulfur	200	1886	1262	3.07	706	0.157	0.647	0.05
	375	1925	1034	3.70	2.06	0.187	0.773	0.05
$NaNO_3$	325	1880	1663	4.07	2.66×10^{-3}	0.562	0.338	0.50
	450	1773	1624	4.30	1.53×10^{-3}	0.540	0.324	0.50
KNO_3	350	1852	1389	3.90	2.77×10^{-3}	0.488	0.347	0.50
	450	1777	1389	4.05	1.79×10^{-3}	0.443	0.324	0.50
Solar salt	250	1924	1539	3.90	5.04×10^{-3}	0.510	0.331	0.50
	425	1810	1552	4.05	1.88×10^{-3}	0.477	0.317	0.50
NaCl–KCl–$MgCl_2$	450	1707	1076	$3-4$	3.79×10^{-3}	0.472	0.361	0.46
	700	1566	951	$3-4$	2.50×10^{-3}	0.407	0.463	0.46

Random error could be caused by optical misalignment for each measurement which could cause small deviation of the heat flux from the calibrated one as well as small deviation of view factor from the sample surface to the IR detector. To minimize this error, we mounted the laser, sample holder, and IR detectors to fixed positions on an optical table. The random uncertainties are determined from the standard deviation of multiple measurements on the same sample, as shown in **Table 2.3**. The random error is around 7.40 %. Considering both the

systematic and random uncertainties, the total uncertainty of the molten salt thermal conductivity measurement in our work is 9.40 %.

Table 2.3 The thermal conductivity measurement result, the average thermal conductivity, and the standard deviation of molten NaCl–KCl–$MgCl_2$ at 450 °C

No. of measurement	Measured *k* of NaCl–KCl–$MgCl_2$ at 450 °C (W m^{-1} K^{-1})
1	0.440
2	0.413
3	0.423
4	0.464
5	0.506
Average (W m^{-1} K^{-1})	0.449
Standard deviation (W m^{-1} K^{-1})	0.033 (7.39%)

2.2.4. DSC measurement

While literature values of c_p of molten salts are used to convert the thermal effusivity to thermal conductivity in the MPR measurements, the melting point and c_p of the molten salt mixtures are still measured using a differential scanning calorimeter (DSC) (404 F3 Pegasus®, NETZSCH) to confirm the composition and characteristics of the mixtures. During the measurement, nitrogen gas (N_2) was used as the protective gas. c_p of a sample was determined by using the ratio method (*88*). A pure sapphire disc was used as the standard. It was noticed that the creeping effect of molten salts occurred when Pt crucibles were used in a DSC measurement (*75*, *89*). When graphite crucibles were used instead, there was no creeping effect observed. The heating rate of the DSC measurement was 20 K min^{-1}. After obtaining the DSC signals of baseline (no sample loading), standard (sapphire), and the actual molten sample samples, c_p of the molten salt was calculated by using Proteus®, an analysis program provided by Netzsch. The

average c_p values were obtained from three measurements, each of which was based on a new sample loading.

2.3. Results and discussion

2.3.1. Calibration of MPR using standard molten materials

The reliability of the MPR measurement with the custom-made molten salt holder is verified by measuring known molten materials, including paraffin wax and sulfur. **Figure 2.4a** and **Figure 2.4b** show the typical raw data of $|\theta_s|$ *vs.* $\omega^{-\frac{1}{2}}$ of the MPR measurement of paraffin wax at 100 ^{o}C and sulfur at 250 ^{o}C respectively, with the data for sulfur at other temperatures shown in **Figure 2.5.** The frequency range for the measurement is carefully selected to ensure the thermal penetration depth δ_p is long enough to probe into the molten samples while minimizing any possible effect from the natural convection in the molten material. The experimental data was fitted with the three-layer model with the radiative heat loss effect, i.e., Eq. (2.6), with the thermal conductivity values of the wax and sulfur shown next to their respective curves in **Figure 2.4a** and **Figure 2.4b**. For molten paraffin wax at 100 ^{o}C, k is determined to be 0.162 ± 0.012 W m^{-1} K^{-1},which is consistent with the average literature value of the same type of paraffin wax (0.160 ± 0.07 W m^{-1} K^{-1}) (*80, 81*). To demonstrate the effect of the natural convection on the measurements, paraffin wax was measured by scanning the sample within a low-frequency range where the natural convection effect is non-negligible. It found that at very-low-frequency (i.e., f = 0.1 Hz), the natural convection in the molten paraffin wax layer is important, such that it can lead to a higher apparent thermal conductivity. The experimental results and the model fitting results for paraffin wax at very-low-frequency are included in **Figure 2.6.**

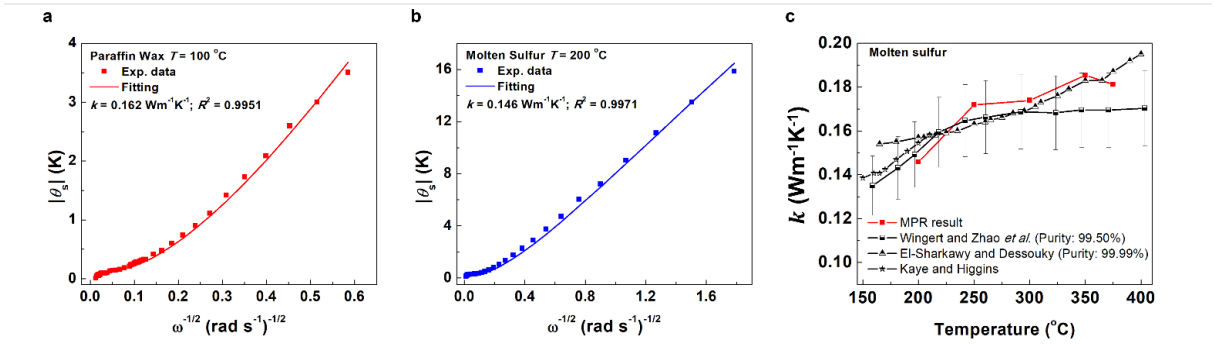

Figure 2.4 Plot of $|\theta_s|$ versus $\omega^{-\frac{1}{2}}$ plot of MPR measurements of **(a)** molten paraffin wax at 100 ^{o}C, and **(b)** molten sulfur at 200 ^{o}C respectively. The fitted thermal conductivity are listed in the plots; **(c)** thermal conductivity of molten sulfur as a function of temperature compared with the existing literature values (*77*, *80*, *81*, *90*, *91*): Wingert and Zhao *et al.* (*92*) (purity: 99.50 %), El-Sharkawy and Dessouky (*77*) (purity: 99.99 %), and Kaye and Higgins (*91*)

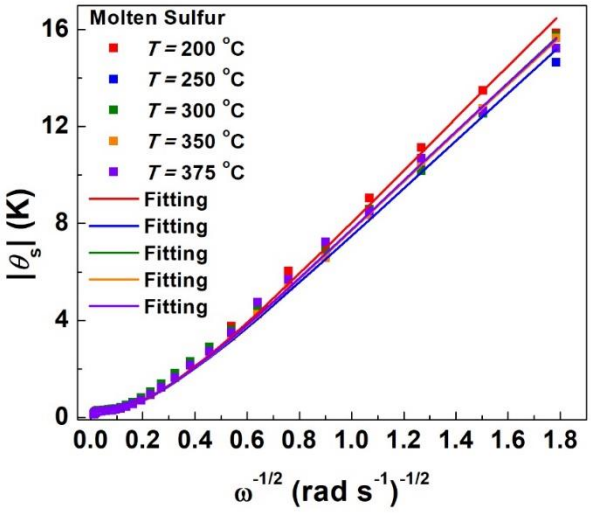

Figure 2.5 Raw data of $|\theta_s|$ *vs.* $\omega^{-\frac{1}{2}}$ of the MPR measurement of molten sulfur at different temperatures ranging from 250 ^{o}C to 375 ^{o}C. The symbols are experimental data and the solid lines are model fitting

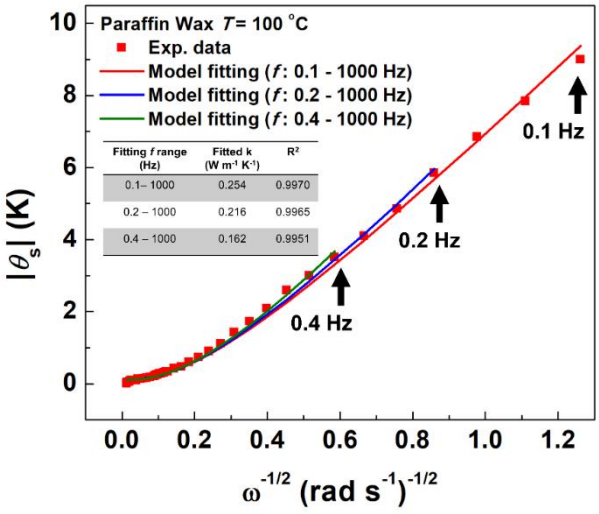

Figure 2.6 Raw data of $|\theta_s|$ *vs.* $\omega^{-\frac{1}{2}}$ of the MPR measurement of molten paraffin wax at 100 °C. The fitting results in different frequency ranges are listed on the inserted Table.

Figure 2.4c shows the measured *k* of molten sulfur from 250 to 375 °C. The average *k* of molten sulfur increases from 0.146 to 0.181 W m^{-1} K^{-1} within the temperature range of 250 to 375 °C. This result shows good agreement with the literature values of sulfur (*77, 90, 91*). Our result is close to that reported by El-Sharkawy and Dessouky (*77*) in which the sulfur has a slightly higher purity (~99.9 %), and is only slightly higher than the results from the frequency-domain hot-wire method by Wingert and Zhao *et al.* (*92*), in which they used sulfur with a purity of 99.50 %. These calibration results demonstrate the reliability of the MPR technique for measuring molten materials.

2.3.2. Specific heat capacity measurements of molten salts

Figure 2.7 show the c_p *vs. T* curves for the solar salt mixture, $NaNO_3$–KNO_3 (wt.% 60–40), NaCl–KCl–$MgCl_2$ (wt.% 15.11–38.91–45.98. The same DSC measurements also yield the melting points of the salts, which are listed in **Table 2.1** and are confirmed to be consistent with the literature values. The measured c_p of $NaNO_3$–KNO_3 decreases from ~1.57 to 1.49 J g^{-1} K^{-1}

when the temperature increases from 250 to 425 °C. The results are consistent with the literature values (*12*) with a maximum difference of ~5 %. The measured c_p of NaCl–KCl–$MgCl_2$ first decreases from ~1.12 to ~1.02 J g^{-1} K^{-1} from 450 to 500 °C and then keeps constant from 500 to 650 °C. It is consistent with the values reported by NREL (*75*) as well as the theoretical prediction obtained using the software Factsage (*75*, *93*). In summary, our DSC measurements on the melting points and c_p confirm that the composition and quality of our salt samples are similar to those used in the earlier studies on the same salts. The literature c_p values of the selected molten salts are thus suitable to be used for the thermal conductivity calculation in the MPR measurements.

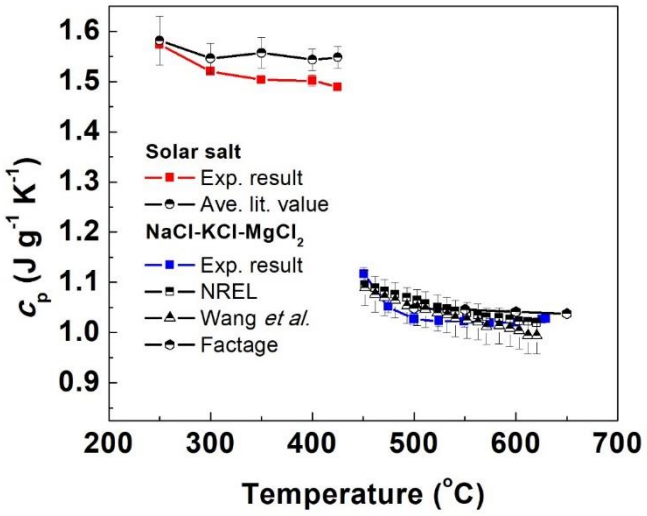

Figure 2.7 Measured specific heat capacity of **(a)** molten solar salt; and **(b)** molten NaCl–KCl–$MgCl_2$.The literature values are included in the plot for comparison. The reference data are from: D'Aguanno *et al.*, Wang *et al.* (*75*), NREL (*75*), and Factage (*93*)

2.3.3. Thermal conductivity of $NaNO_3$ and KNO_3

Figure 2.8 shows the measured temperature-dependent thermal conductivity of molten $NaNO_3$ and KNO_3. The low-frequency linear regions of the $|\theta_s|$ *vs.* $\omega^{-\frac{1}{2}}$ plots are shown in

Figure 2.9. Our MPR results show that the thermal conductivity of molten $NaNO_3$ slightly decreases from 0.562 to 0.540 W m^{-1} K^{-1} when the temperature increases from 350 to 450 ^oC. For molten KNO_3, the measured thermal conductivity also shows a graduate decrease from 0.488 to 0.443 W m^{-1} K^{-1} from 350 to 450 ^oC. Similar to the measurement of sulfur, our measured results of molten $NaNO_3$ and KNO_3 are close to that of Zhao *et al.* (*15*). Both our MPR and Zhao *et al.*'s results are higher than most of the literature-reported values by 10-15 %, including those obtained from the LFA method. It is also noted that there is a large discrepancy among the literature-reported values. The data obtained by the steady state method might be problematic due to convection errors, the presence of radiation loss, and inaccurate heat flux calibration (*17, 59, 94*); on the other hand, time-domain measurement data can be highly influenced by the time window selected for data processing. The time window has to be selected in order to eliminate errors from natural convection and the thermophysical properties of the sensor or confinement materials. Since the MPR and Zhao *et al.*'s methods are both based on frequency-domain techniques, which are expected to eliminate the convection effect and are less sensitive to the salt creeping effect, these results are likely better representatives of the true thermal conductivity of the two nitrate salts measured here. A detailed discussion on the differences between the MPR technique and the LFA method is included in *Section 2.4*.

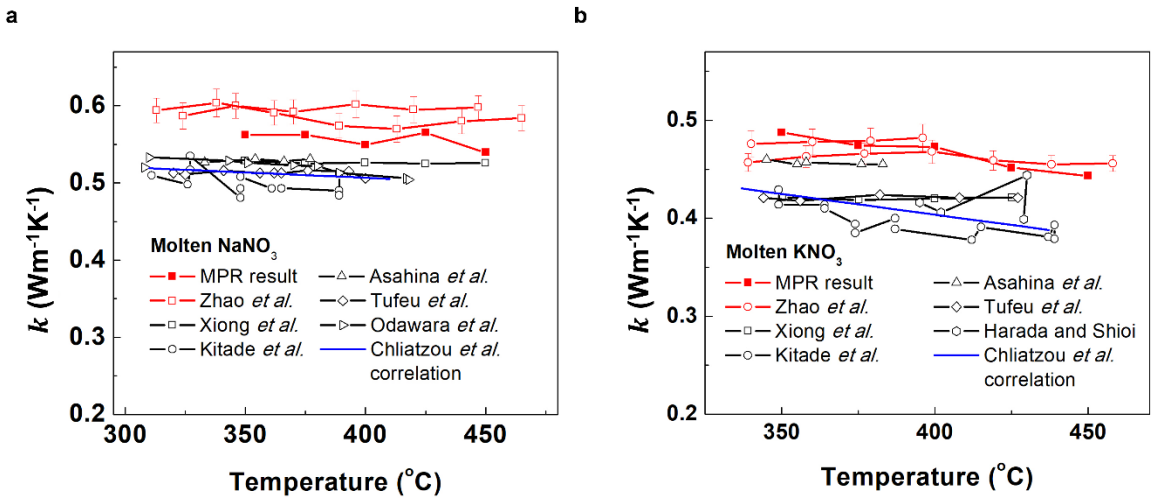

Figure 2.8 Measured temperature-dependent thermal conductivity of (**a)** molten $NaNO_3$ and **(b)** molten KNO_3, along with selected literature values. The reference data are from: Zhao *et al.* (*15*) (frequency-domain hot-wire method), Xiong *et al.* (*95*) (LFA), Kitade *et al.* (*96*) (THW), Asahina *et al.* (*97*) (pulse heated flat plate technique), Tufeu *et al.* (*94*) (steady state method), Odawara *et al.* (*98*) (wave-front-shearing interferometry), Harada and Shioi (*17*) (LFA), and Chliatzou *et al.*'s correlation (*17*).

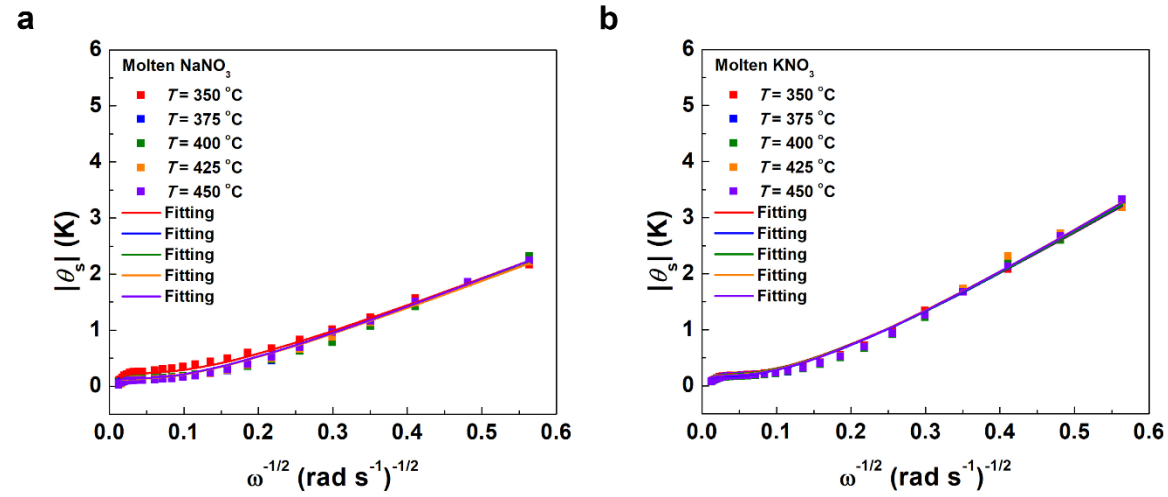

Figure 2.9 $|\theta_s|$ *vs.* $\omega^{-\frac{1}{2}}$ plot of **(a)** molten $NaNO_3$ from 320 to 450 °C; and **(b)** molten KNO_3 from 350 to 450 °C. The symbols are experimental data and the solid lines are model fitting.

2.3.4. Thermal conductivity of solar salt ($NaNO_3$-KNO_3 mixture)

Figure 2.10 shows the measured thermal conductivity of the molten solar salt. The experimental data of $|\theta_s|$ *vs.* $\omega^{-\frac{1}{2}}$ of this salt are shown in **Figure 2.11**. The measured thermal

conductivity of the molten solar salt slightly decreases from 0.510 to 0.477 W m^{-1} K^{-1} when the temperature increases from 300 to 425 ^{o}C. Because thermal conductivity of the molten nitrate salt is mainly contributed by diffusons (*68*), or vibrational modes with approximately inter-molecular diffusion length, the thermal conductivity of the molten mixture is expected to lie in between those of its constituents, which is the case for our measured k values.

Furthermore, the measured result is compared to the estimated one based on the rule of mixing, i.e.:

$$k_{\mathrm{NaNO3-\,KNO3}} = ak_{\mathrm{NaNO3}} + (1-a)k_{\mathrm{KNO3}} \qquad (2.11)$$

where k_{NaNO3} and k_{KNO3} are the thermal conductivity of pure $NaNO_3$ and KNO_3 respectively from our MPR measurements (shown in **Figure 2.8**), and a = 0.64 is the molar percentage of $NaNO_3$ salt. As shown in **Figure 2.10**, the measured k value is about 10 % lower than that of the estimated one at 300 ^{o}C but the two values are getting closer at higher temperatures. This result may be attributed to additional phonon scattering by different cations in the mixture, which suggests that the propagating phonons could still contribute to a small but non-negligible portion of thermal conductivity in the pure nitrate salts at around 300 ^{o}C but this contribution is gradually diminished at higher temperature. Nevertheless, the mechanistic understanding of heat conduction in these salts would warrant further studies, perhaps using atomistic simulations (*99-101*).

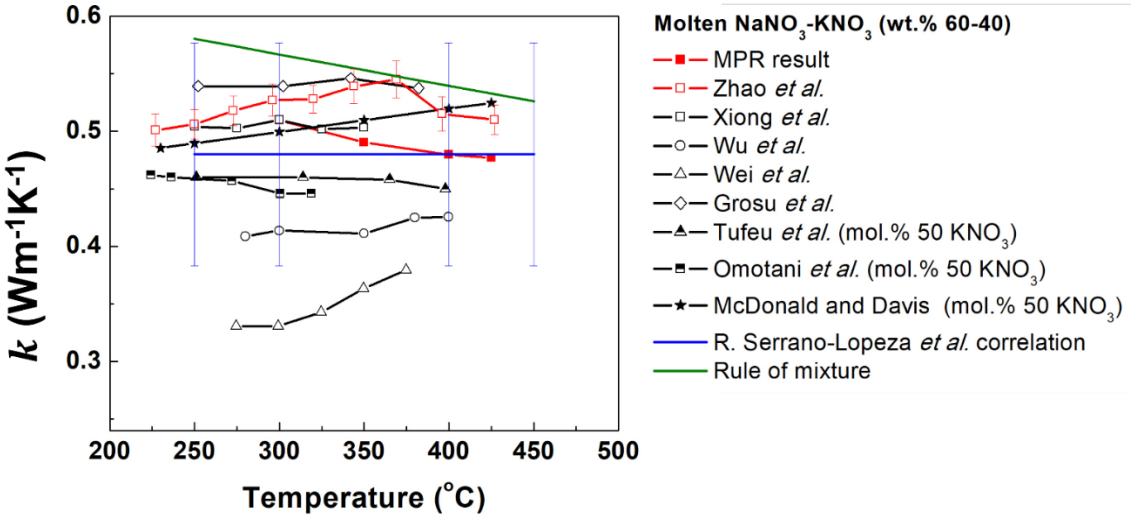

Figure 2.10 Thermal conductivity of molten solar salt along with selected literature results of $NaNO_3$–KNO_3 mixtures and the calculated thermal conductivity according to the rule of mixtures. The reference data are from: Zhao *et al.* (*15*) (frequency-domain hot-wire method), Xiong *et al.* (*95*) (LFA) , Wu *et al.* (*102*) (LFA), Wei *et al.* (*103*) (LFA), Grosu *et al.* (*62*) (LFA), Tufeu *et al.* (*94*) ($NaNO_3$–KNO_3 mol.% 50-50, steady state method), Omotani *et al.* (*56*) ($NaNO_3$–KNO_3 mol.% 50-50, THW), McDonald and Davis (*59*) ($NaNO_3$–KNO_3 mol.% 50-50, steady state method), and R. Serrano-López *et al.*'s correlation (*104*)

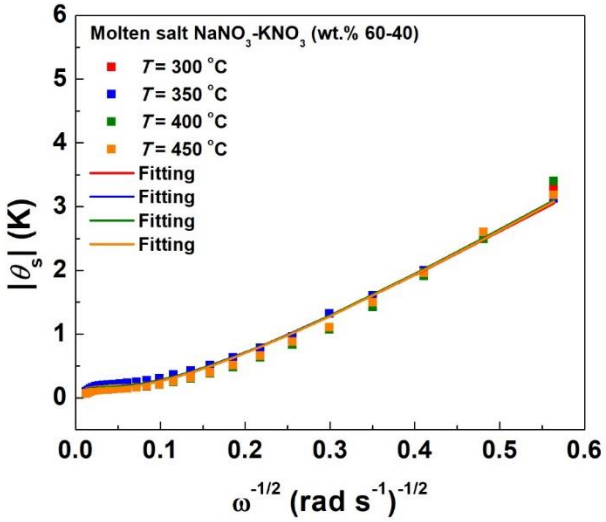

Figure 2.11 $|\theta_s|$ *vs.* $\omega^{-\frac{1}{2}}$ plot of molten solar salt from 250 to 425 °C. The symbols are experimental data and the solid lines are model fitting

Figure 2.10 also compares the MPR results with the literature ones and the suggested correlations. Our measurement values are again in excellent agreement with those of Zhao *et al*. (*15*), as well as those by Gruso *et al.*(*62*) (using LFA with a Zn crucible) and Xiong *et al.* (*95*) (LFA). Our and Zhao *et al.*'s results are slightly higher than the correlation suggested by R. Serrano-López *et al.* (0.480 ± 0.098 W m^{-1} K^{-1}) (*104*). On the other hand, the LFA results from Wu *et al.* (*102*) and Wei *et al.* (*103*) show significantly lower values, even lower than that of pure KNO_3, which cannot be explained with the existing theories. On a similar nitrate salt mixture with 50 mol. % of KNO_3, the results from McDonald and Davis (steady state method) (*59*), Tufeu *et al.* (steady state method) (*105*), and Omotani *et al.* (THW) (*56*) also show discrepancies in both the absolute values and temperature trends. As mentioned in *Section 3.3*, the molten salt thermal conductivity obtained using the steady state method and time-domain measurement techniques can be susceptible to errors from convection, radiation loss, and biased time window for data processing. It reveals the fact that reliable molten salt thermal conductivity data are difficult to obtain using the steady state, THW, or LFA methods. A more detailed discussion of LFA measurements of molten salts is presented in *Section 2.4.*

2.3.5. Thermal conductivity of ternary chloride salts

Figure 2.12 shows the measured thermal conductivity of molten NaCl–KCl–$MgCl_2$ as a function of temperature. The available literature values are included for comparison. The ρ and c_p of each salt for the *k* determination are extracted from ref (*75*) . The experimental data of $|\theta_s|$ versus $\omega^{-\frac{1}{2}}$ are included in **Figure 2.13**. The measured thermal conductivity of molten NaCl–KCl–$MgCl_2$ slightly decreases from 0.506 to 0.400 W m^{-1} K^{-1} when the temperature increases from 450 to 650 ^{o}C. The experimental result is generally consistent with the results reported by

Wang *et al.* (*75*) using LFA on the same salt, although their measured thermal conductivity of this molten salt shows a stronger decreasing trend with temperature.

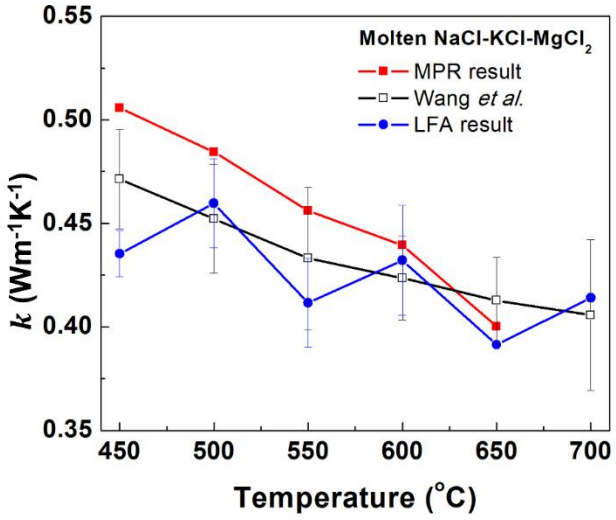

Figure 2.12 Measured temperature-dependent thermal conductivity of molten NaCl–KCl–$MgCl_2$. The reference data are from: Wang *et al.* (*75*) (LFA)

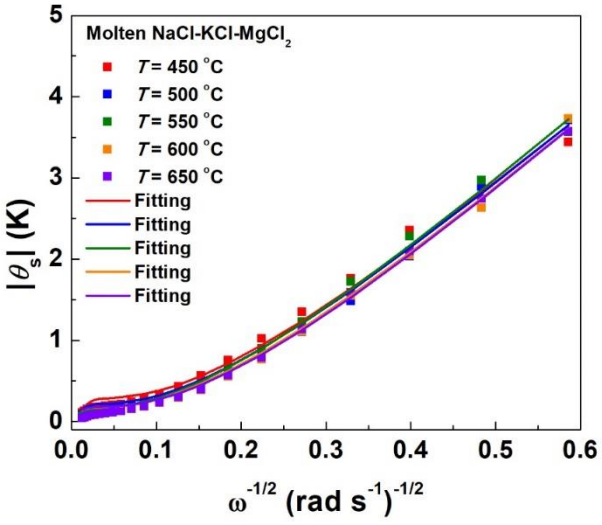

Figure 2.13 $|\theta_s|$ *vs.* $\omega^{-\frac{1}{2}}$ plot of molten NaCl–KCl–$MgCl_2$ from 450 to 650 °C. The symbols are experimental data and the solid lines are model fitting.

2.4. Comparison with other measurements

DiGuilio and Teja (*106*) have reviewed major thermal conductivity models for molten salts. They concluded that the thermal conductivity of molten salts should show a decreasing trend with increasing temperature. Recently, Zhao *et al.* (*68*) developed a phonon gas model for dense, strongly interacting liquids to predict the thermal conductivity of molten $NaNO_3$ and KNO_3. Their modeling results show that pure molten $NaNO_3$ and KNO_3 exhibit slightly decreasing trends in thermal conductivity as temperature increases. The modeling results match well with their previous reported experimental values using the frequency-domain hot-wire method (*15*). According to our MPR experimental results, the measured thermal conductivity of molten salts in general shows a slightly decreasing or nearly constant temperature dependence. It is consistent with Zhao *et al.*'s model (*68*) and experimental data (*15*). On the other hand, many of the thermal conductivity data of molten nitrate salts reported earlier show an increasing trend with temperature (*107*) (**Figures 2.4** & **2.5**). This could be attributed to the measurement errors originated from the stronger convection effect of molten salt and thermal radiation at higher temperature in conventional measurement techniques. Therefore, it is believed that the experimental results from the MPR technique and the frequency-domain hot-wire method are more reliable on molten nitrate salts, whereas other techniques such as LFA and the steady state method are more susceptible to larger errors as evidenced by the relatively large scattering of the data. Our MPR data are also in line with the recent LFA results on the two ternary chloride salts, suggesting that MPR is reliable on both nitrate and chloride salts while there could be special precautions needed for LFA on different types of molten salts, which warrants further investigation.

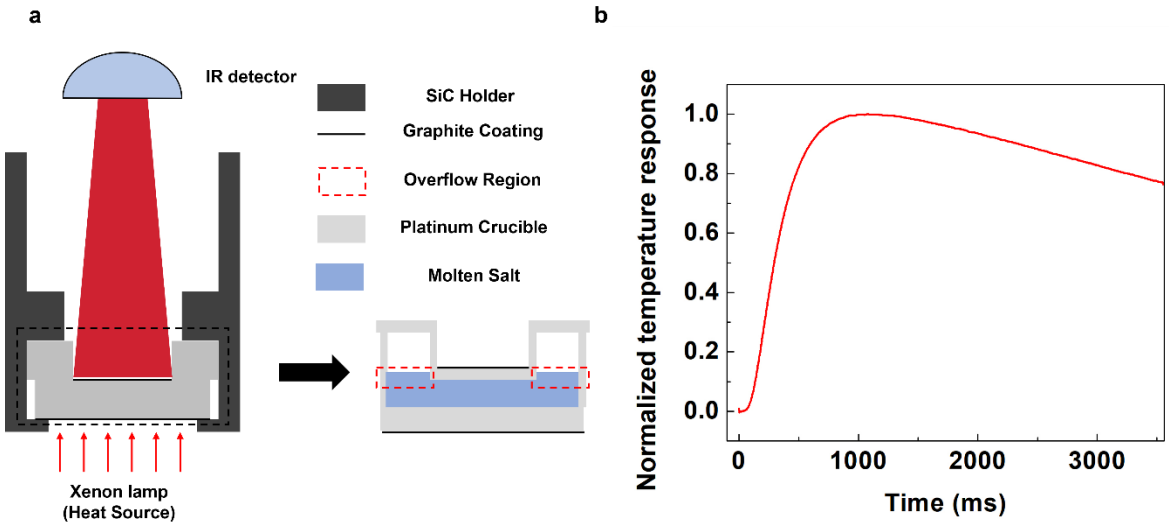

Figure 2.14 Detailed schematic of our LFA measurement: **(a)** schematic of LFA (LFA 467 HT HyperFlash, NETZSCH), including Pt crucible (black dashed line section view), SiC holder and the infrared (IR) detector for collecting the radiative thermal response form the graphite-coated top surface of Pt crucible; the overflow region aims to ensure the full immersion of the Pt crucible lid into the molten salt; and **(b)** raw data of the normalized front side temperature response as a function of time in an LFA measurement of molten $NaNO_3$ at 350 ^oC.

Here we specifically comment on several factors compounding the LFA because it has been a widely used technique in recent years. LFA is a time-domain method based on front side pulsed photothermal heating and back-side infrared thermometry **(Figure 2.14).** According to discussion found in the literature and our own experience with the LFA, it was found that LFA measurement could be sensitive to various experimental conditions, such as the exact salt loading in the crucibles (*62, 63, 108*), type of crucibles used and their wettability with the molten salts (a non-wettable surface such as graphite could create a gap with the salt (*62, 108, 109*), whereas a wettable surface such as Pt could lead to significant salt creeping effect (*62, 63*)), the thickness of the salt layer in the crucibles (thicker layer could have significant natural convection effect (*67, 108*)), the overall measurement time (longer measurement duration could exacerbate the salt creeping effect (*63*)), exact temperature rise window used for data fitting (*64-66*), etc. The lack of a standard procedure of LFA for molten salts to control these factors could have contributed to

the large scattering of the LFA data reported so far. Nevertheless, when properly done, the LFA method does yield reasonable results on the two chloride salts measured here. Consistent data on the NaCl–KCl–$MgCl_2$ salt was also obtained using our own LFA (**Figure 2.12**). Our experience as well as that of the authors of ref (*75*) shows that it is critical to minimize the salt creeping effect, e.g., by loading a suitable amount of salt and limiting the measurement time to about two temperature points for each salt loading.

The MPR method shows several advantages of addressing the issues in LFA (**Figure 2.1**). First, the MPR technique is a front side sensing method, which eliminates the influences of the convection effect or gaps between the salt and the backside of crucibles in LFA. Second, the MPR molten salt holder is vertically oriented whereas the LFA sample crucible is typically horizontally positioned. The vertical orientation of the holder avoids the issues due to the salt creeping effect because the salt will always be in contact with the front and back metallic sides of the holder due to their high wettability with the molten salts. The salt creeping in LFA could lead to non-uniform distribution of the horizontal molten salt layer inside the crucible. Lastly, MPR is a frequency-domain technique, so the thermal penetration depth can be controlled to be a few hundred micrometers within the molten salt volume, which minimizes the possible natural convection effect in the salt and heat losses from the crucible to the environment that could be present in a time-domain method. In LFA, typically only data within a certain time window are used for fitting to reduce the errors caused by the convection and heat loss effects (*64-66*). However, there is no standard or quantitative guideline for the selection of the time window, which could appreciably impact the extracted thermal diffusivity.

2.5. Conclusion

The current paper presents the development of a non-contact, frequency-domain MPR technique as a convenient and reliable method of thermal conductivity measurement for molten salts. The MPR technique is calibrated using standard phase change materials, including paraffin wax and sulfur, demonstrating the suitability of the MPR technique in determining the thermal conductivity of molten materials. Nitrate and chloride salts for high-temperature CSP systems are measured using the MPR technique. Our results on $NaNO_3$, KNO_3, and solar salt show excellent agreement with those obtained by Zhao *et al*. (*15*) using another frequency-domain technique based on a hot-wire method. The MPR technique also yields reasonable results on chloride salts. The MPR technique avoids the complicated setup preparation procedures that are otherwise required in contact-based techniques. The frequency-domain feature of the MPR enables the precise control of the thermal penetration depth in the measurement, thus eliminating the possible convection heat transfer effect commonly encountered in the LFA and other conventional time-domain measurements. The use of the front side sensing and the vertical holder orientation also minimize the impact of the salt creeping effect, which is often an issue in LFA. The work demonstrated that the MPR technique developed here will be especially useful for measuring high temperature thermal conductivity of emerging molten salts and other challenging fluids (such as molten metals) for future thermal energy conversion and storage systems.

Acknowledgements

Chapter 2 is a full reprint of **K. M. Chung**, T. Feng, J. Zeng, S. R. Adapa, X. Zhang, A. Z. Zhao, Y. Zhang, P. Li, Y. Zhao, J. E. Garay, and R. Chen. "Thermal Conductivity Measurement of Nitrate and Chloride Molten Salts Using Modulated Photothermal Radiometry " *International*

Journal of Heat and Mass Transfer 217 (2023): 124652. For this publication, K. M. Chung performed the experiments, data analysis and manuscript writing.

Chapter 3. *In-situ* thermophysical measurement of flowing molten chloride salt using modulated photothermal radiometry

3.1. Introduction

Concentrated solar power (CSP) plants with thermal energy storage (TES) systems are one of the most promising emerging renewable energy systems with the capability of delivering dispatchable electricity by utilizing abundant solar energy (*50, 110*). To deliver the heat collected from the concentrated sunlight to a heat exchanger and thermal storage tank, a heat transfer fluid (HTF) is needed for a CSP system. An ideal HTF requires a high thermal conductivity for efficient thermal energy transfer, a high heat capacity for large quantities of sensible thermal energy storage, and a low viscosity that renders minimal power consumption for circulating the fluid (*11, 111*).

In state-of-the-art CSP technologies, there are two common HTFs: oil-based HTFs and molten salt-based HTFs. Synthetic oil, such as Therminol VP-1 (Biphenyl and Diphenyl oxide), is a commonly used HTFs in the 1st and 2nd generation of CSP power plants (*11, 111, 112*). It can reach a maximum operating temperature of 400 ^{o}C. However, oil-based CSP plants usually have limited thermal energy storage capability (*112, 113*), which makes molten salts being competitive as the HTFs for CSP applications from the energy storage capability point of view. Nitrate salt mixtures, $NaNO_3$-KNO_3, is used for heliostat CSP tower with a maximum operating temperature of 560 ^{o}C (*114*). CSP plants using molten $NaNO_3$-KNO_3 can provide around 8-10 hours of thermal energy storage (*113*). The next generation CSP integrated with TES facilities aims at a higher operating temperature (> 700 ^{o}C) to achieve both a high power cycling efficiency (> 50 %) and a lower levelized cost of electricity (LCOE) of $0.05 per kWh (*112*). Eutectic molten

chloride salts, such as $MgCl_2$-KCl, or NaCl-KCl-$MgCl_2$, that can work at high temperatures of up to 800 ^oC, are considered as good HTF candidates for next-generation CSP due to their favorable thermal and transport properties, high boiling point, acceptable low freezing point, and low price to meet the large quantity of demand for thermal storage (*115*-*117*).

Limited to insufficiency of reliable molten salt thermal conductivity data, it is usually difficult to evaluate molten salt heat transfer performance in the entire operating temperatures. For example, there is a difference of up to 40% among the reported thermal conductivity values for solar salt (*55*), despite its widespread use in commercial CSP plants. Reliable data on emerging high-temperature chloride salts are even more insufficient. The scattered thermal conductivity data in the molten salt is mainly due to measurement errors, caused by convection, radiation, and corrosion during the measurement process. These errors can be further magnified in the convectional measurement techniques (i.e., steady state method, transient hot-wire (THW) method, and laser flash analyzer (LFA) at high temperatures. Other than the importance of obtaining accurate molten salt thermal conductivity when it is static, monitoring the thermal transport properties of molten salts in their flowing state in real-world applications is even more important. The effective thermal conductivity k_{eff} of flowing molten salts is a crucial indicator to evaluate their thermal transport property under various flow and temperature operational conditions. Several measurement techniques have been developed and modified to remove the barriers in measuring molten salts, molten metal, and other high-temperature fluids. Zhao *et al.* (*15*) have developed a frequency-domain THW method to measure molten nitrate salts. Their reported results are believed to be a more appropriate representative of molten nitrate salt thermal conductivity because their frequency-domain method can limit the thermal penetration of the measurements within less than 100 μm, thus enabling a negligible natural convection error

in the measurements. However, their measurements were still limited to the operating temperatures of molten nitrate salts of less than 500 ^{o}C. At even higher temperatures, the alumina-coated Pt wire in their measurement device could be damaged due to thermal stress and corrosion issues.

In-situ measurement of flowing fluids is also important to the evaluation of the thermal transport properties of flowing fluids in real time. However, there is a lack of measurement techniques for flowing fluid. Langstaff *et al.* (*118*) have developed an *in-situ* thermophysical measurement technique for high-temperature liquids using aerodynamic levitation (ADL). They demonstrated the technique by measuring the thermophysical property of Al_2O_3 droplets *in-situ* over the entire liquid and super-cooled regimes. However, this technique might not be accessible to flowing liquids. Hong and Kim (*119*) measured flowing D.I. water in a circular tube using a 3ω method. It demonstrates that the intrinsic thermal conductivity of the fluids can be measured when the flow condition and heating frequency are carefully adjusted. However, the technique may not be suitable for high-temperature measurements where the 3ω heater and sensor can be damaged. Mehrvand and Putnam (*120*) reported the use of time-domain thermoreflectance (TDTR) to characterize the local heat transfer coefficient of flowing water and refrigerant in a microchannel. The difficulty of the method may have arisen from the preparation complexity and the stability of the metal coating on the surface of the measurement window. In addition, further work is needed to demonstrate the capability of the technique to perform measurements for wider channels and at high temperatures (> 500 ^{o}C) for more practical applications in industry and power plants where HTFs are usually operating at high temperatures.

Recently, we have reported the thermal conductivity measurement of molten salts, including molten nitrate and chloride salts, using the modulated photothermal radiometry (MPR)

technique. It is a laser-based, non-contact, frequency-domain measurement technique that can eliminate the errors from corrosion and convection effects in molten salts, thus being capable of extracting accurate molten salt thermal conductivity. The MPR technique was also applied for measuring flowing fluids *in-situ* at room temperature and intermediate temperatures (*70*). In the MPR flowing fluid property measurement, the intrinsic thermal conductivity k_0 of D.I. water and thermal oil were extracted when the flows satisfy the criteria of $Re^{1/2}Pr^{1/3} < 100$ in the given experimental conditions. In this work, we performed the *in-situ* thermal conductivity of flowing molten salt inside a molten salt flow loop. We selected NaCl-KCl-$MgCl_2$ (wt% 15.11–38.91–45.98) to study the relative changes in k_{eff} of the molten salt under different flow conditions and temperatures. Based on the measured intrinsic thermal conductivity, the convective heat transfer coefficient *h* of flowing NaCl-KCl-$MgCl_2$ was also estimated using Gnielinski's correlation.

To our best knowledge, this is the first *in-situ* thermal conductivity measurement of flowing molten salt. It opens the possibility to apply the MPR technique to accurately extract and monitor possible changes in the thermal transport properties of molten salts and other high-temperature liquids (i.e., molten metal) under various operating conditions, which will be valuable to the further optimization of the overall heat transfer performance of the HTFs.

3.2. Experimental procedures

3.2.1. Salt properties and salt preparation

The molten salt loop equipped with the molten salt reservoir was built at the University of Arizona (UA). The selected chloride salt in this work is NaCl-KCl-$MgCl_2$ (wt% 15.11–38.91–45.98) (*75, 116*). The overview of the molten salt loop integrated with the MPR setup is shown in

Figure 3.1. The physical properties of the molten salt studied by the team at the UA and National Renewable Energy Laboratory (NREL) (*75*) are listed in **Table 3.1**.

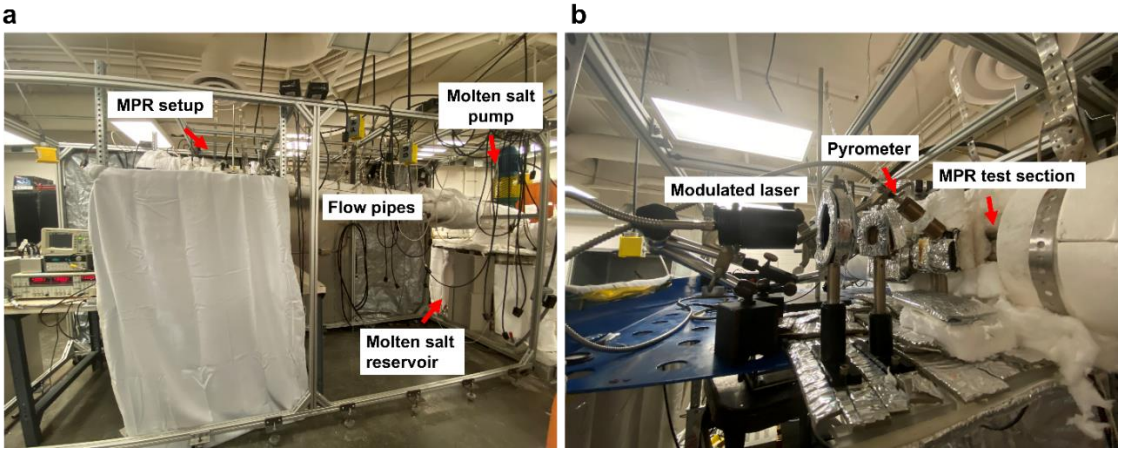

Figure 3.1 (a) Overview of the molten salt loop; and **(b)** close-up of the MPR setup that is integrated to the molten salt flow loop

Table 3.1 The properties of the eutectic chloride salt NaCl-KCl-$MgCl_2$ (wt % 15.11–38.91–45.98). It is from reference (*75*)

Properties	Correlations as a function of T (°C)
Density ρ_o (kg m^{-3})	$1958.8438-0.56355 \times T$
Specific heat capacity $c_{p,o}$ (J g^{-1} K^{-1})	$1.30138-0.005 \times T$
Dynamic viscosity μ (Pa·s)	$7.0645\times10^{-4} \exp\left(\frac{1204.11348}{T+237.15}\right)$
Thermal conductivity k_o (W m^{-1} K^{-1})	$0.5822-2.6\times10^{-4} \times T$

The ternary molten salts were prepared according to the protocol reported by Zhang et al (*121*). Briefly, the constituent components of the eutectic salt, including anhydrous salt powders of $MgCl_2$ (Thermo Fisher Scientific Chemical Inc., purity: 99.0 %), KCl (Thermo Fisher Scientific Chemical Inc., purity: 99.0-100.5 %), and NaCl (Thermo Fisher Scientific Chemical Inc., purity: 99.5 %) were mixed according to the required weighted percentage of the composition (45.98% $MgCl_2$, 38.91% KCl, 15.11% NaCl). Less than 0.1 wt % of elemental Mg

was added as suggested by Zhao and Vidal (*116*) to reduce the presence of corrosive impurities, mainly water. The salts were then grounded into fine powders. The eutectic mixtures were then loaded into a Hastelloy C-276-made reservoir (inner diameter 508 mm, height 533.4 mm) for melting. The schematic of the reservoir is shown in **Figure 3.2**. The reservoir was sat in a furnace (Model KM714, Skutt Ceramic Products, Inc.) that can heat the molten salt from room temperature to 750^{o}C. Before the salt melting process, the reservoir was evacuated to remove air, moisture, and other impurities. The salt was first heated to 150 ^{o}C and stayed at that temperature for more than an hour to remove the water content in the salt. After salt melting, it was degassed with a dry nitrogen gas to minimize any residual water and trapped air. Humidity and oxygen sensors were installed at the opening of the vent of the reservoir for air and moisture monitoring. The volume of the molten salt prepared in this work was about 102.68 L.

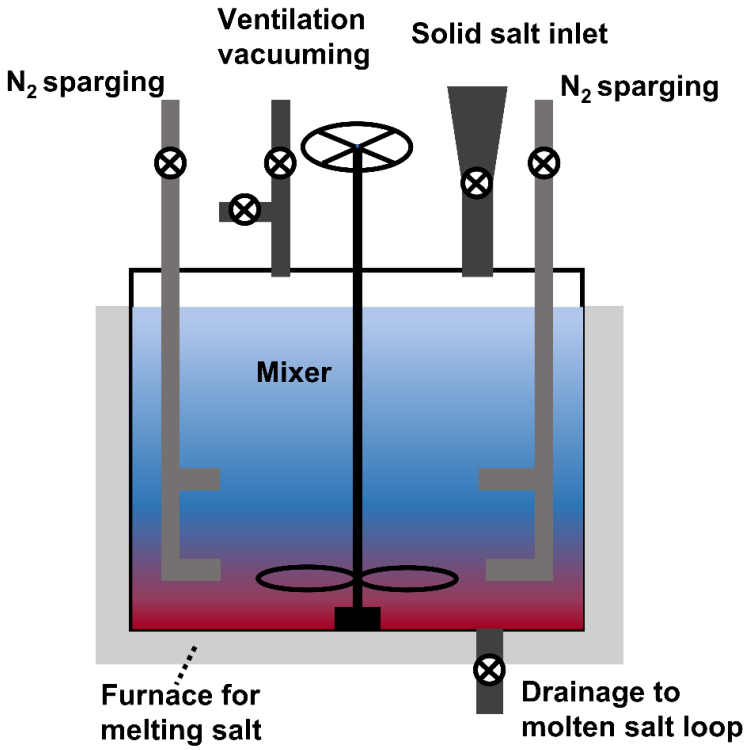

Figure 3.2 Salt melting and purification in salt reservoir

3.2.2. High-temperature molten salt loop and operation procedures

Figure 3.3a shows the schematic of the molten salt loop and the *in-situ* MPR measurements. The molten salt loop was mainly comprised of a molten salt reservoir, a high-temperature molten salt pump (Nagle Pumps, Inc.) with a maximum molten salt pumping rate of 0.63 L s^{-1}, and a designated MPR test section. The pipes of the loop were made of Hastelloy C-276 (outer diameter: 25.4 mm, wall thickness: 1.2446 mm; total length: 6.4 m). The flow loop in total could contain a molten salt volume of 3.24 L. The MPR test section was a modified Inconel 625 tube with a tube outer diameter of 25.4 mm and 1 mm in wall thickness. In the middle of the tube, which is the MPR measurement window, a 100 μm thick Inconel 625 sheet was wielded on the tube. Such a thin layer is required to maintain the high sensitivity of the measurement to the flowing molten salt regime. The thin Inconel 625 sheet was coated with a thin layer of Pyromark 2500 (10-15 μm) for laser heating absorption. The back side of the Inconel 625 sheet was also coated with a 200 nm thick Pt layer to avoid severe corrosion of the measurement window. The photograph of the MPR test section is given in **Figure 3.4**. The pipes of the flowing loops were tilted by 5 ^{o} relative to the ground so that the molten salt could flow back to the reservoir in case the molten salt flow loop stopped operating. The molten salt was then pumped out and flowed into the *in-situ* MPR thermal conductivity measurement. The instruments used to control the flow and temperature of the molten salt loop were described in an earlier paper (*121*).

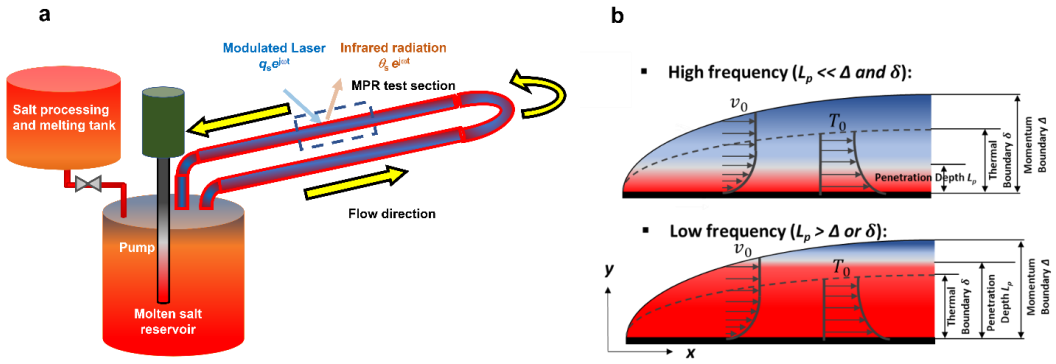

Figure 3.3 (a) Schematic of molten chloride salt loop and the MPR *in-stiu* measurement on the test section; and **(b)** Schematics of momentum boundary, thermal boundary and thermal penetration depth in the MPR measurement

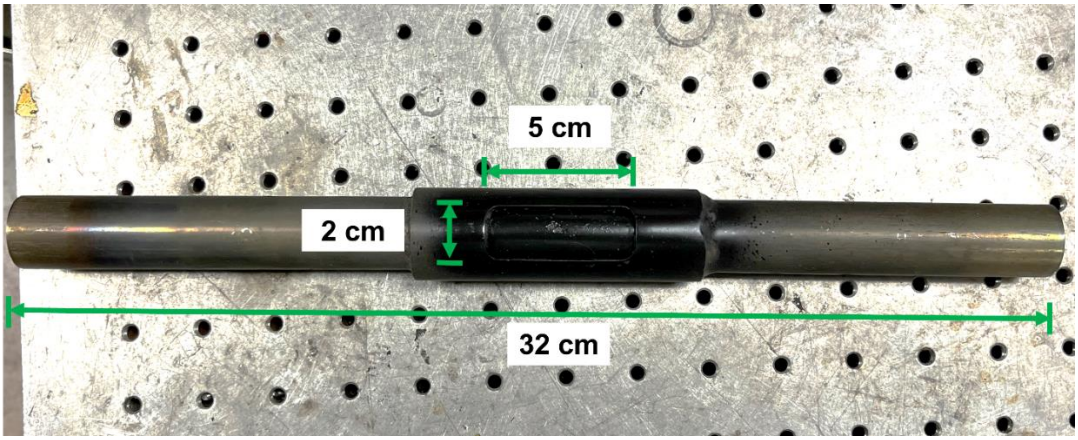

Figure 3.4 Photograph of the MPR test section

3.3. MPR *in-situ* measurement principle

3.3.1. MPR model for flowing fluid measurement

The instrumentation details of the MPR system was described in our earlier work (*69*) and the procedure of applying it for *in-situ* thermal conductivity measurement of flowing fluids inside a tube was reported in (*70*). Here we will only briefly introduce the setup. In an MPR measurement, a continuous laser with modulating angular frequency ω ($q(t) = q_s e^{j\omega t}$) heats the front surface of the Inconel window of the test section. The temperature oscillation of the fluid flowing inside the test section ($\theta_s(t) = \theta_s e^{j\omega t}$) is measured using both a high-speed MCT (mercury-cadmium-telluride) infrared (IR) detector and a pyrometer. A tube containing molten

salt can be modeled as three layers: a thin (< 20 μm) black coating at outer surface (for laser absorption and IR emission), the tube wall (100 μm thick Inconel sheet), and the molten salt layer. The heat transfer problem on the cylindrical tube geometry can be approximated as a planar one with < 7 % error. When the modulation frequency ω is low enough, the thermal penetration depth (L_p) is well into the molten salt layer and the surface temperature oscillation (θ_s) induced by the intensity-modulated laser can be expressed as (*70*):

$$\theta_s = q_s\left(\frac{\exp\left(-\frac{\pi}{4}j\right)}{e_o\sqrt{\omega}} + R_{c,s}\right) \tag{3.1}$$

where e_o is the thermal effusivity of the molten salt; $R_{c,s}$ is the lumped thermal resistance from the thin Inconel sheet and the Pyromark coating (*70*):

$$R_{c,s} = \left(1 - \frac{e_s}{e_o}\right)\frac{l_s}{k_s} + \left(\frac{1}{2} - \frac{{e_c}^2}{{e_0}^2}\right)\frac{l_c}{k_c} \tag{3.2}$$

where e, k and l are thermal effusivity, thermal conductivity, and thickness. The subscripts s and c stand for the thin Inconel sheet and the coating layer. According to Eq. (3.1), the thermal effusivity of the molten salt layer e_o can then be derived from the slope m_o of the $|\theta_s|$ *vs.* $\omega^{-\frac{1}{2}}$ plot in the low-frequency region given that q_s is known. To eliminate the uncertainty in the q_s measurement, a reference sample (borosilicate glass) is introduced for calibrating q_s. Using a differential method, e_o can be obtained by comparing m_o and m_{ref}, the slope of the $|\theta_s|$ *vs.* $\omega^{-\frac{1}{2}}$ plot of the reference with a standard thermal effusivity (e_{ref}): e_o can be obtained as given in Eq. (3.3), by comparing with the reference:

$$e_o = \frac{m_{ref}}{m_o} e_{ref} \tag{3.3}$$

Borosilicate glass was chosen as the reference sample because it has a well-established thermophysical property (*71*). e_o of the molten salt layer is then converted to k_o,

$$k_o = \frac{{e_o}^2}{\rho_o c_{p,o}} \tag{3.4}$$

The thermal conductivity calculation based on Eqs. (3.3- 3.4) takes advantage of the simplicity of mathematical operation without involving complicated model fitting and data processing. It provides a simple and convenient method to dictate the sample's thermal conductivity by comparing the slope of $|\theta_s|$ *vs.* $\omega^{-\frac{1}{2}}$ plot in the appropriate frequency range. It is beneficial for the *in-situ* measurements that require a timely response to the change in thermal conductivity of the layer that is of interest. The limitations of this method will be discussed in *Section 3.4.2*.

3.3.2. Criteria of measuring intrinsic thermal conductivity of flowing fluids

Figure 3.3b shows the 2D schematic of the flow inside the test section during the MPR measurement. The thermal boundary layer, momentum boundary layer, and the thermal penetration depth at both high-and-low frequency cases are illustrated. For convenience in the flow analysis, we assume a laminar flow. The hydrodynamic entrance length L_{ef} and the thermal entrance length L_{eh} are given in the following (*122*):

$$L_{ef} = 0.05 Re_D D \tag{3.5}$$

and

$$L_{eh} = 0.05 Re_D Pr D \tag{3.6}$$

where Re_D is the Reynold number, Pr is the Prandtl number, and D is the cylindrical tube diameter. Based on the thermophysical property of molten NaCl-KCl-$MgCl_2$ and the

experimental conditions given in Table 1, Re_D and Pr of the molten salt ranges from around 3805 – 15000 and 7, respectively. Using Eq. (3.5), the estimated L_{ef} and L_{eh} ranges from 500 – 1900 cm, and 3400 – 13000 cm, respectively. Since the laser spot of ~ 10 mm targets at the middle of the MPR test section where the Inconel measurement window locates, the flow is still in both hydrodynamic and thermal entrance regions. The above analysis shows that the thermal boundary layer δ of the flow is always thinner than its momentum boundary layer Δ in our measurements. According to our previous MPR flowing fluid measurement (*70*), when the thermal penetration depth in the measurement is less than both the thermal boundary layer and momentum boundary layer, the intrinsic thermal conductivity of a flowing fluid can be measured (**Figure 3.3b upper schematic**). In other words, the following criteria has to be satisfied: $L_p <$ min [Δ, δ]. Otherwise, when $L_p > \Delta$ or δ, the temperature response from the test section would be affected by the momentum boundary layer, a more prominent convective effect would then be observed. Under the laminar flow assumption, $\delta = Pr^{-\frac{1}{3}}\Delta$, and $\Delta = 5\sqrt{\frac{\nu x}{u_b}}$, where ν is the kinematic viscosity of the fluid, and x is the characteristic entrance length of the measurement section as shown in **Figure 3.3b** (x ~ 15 cm in our experiment), and u_b is the flow velocity. To satisfy the criteria, we require $L_p < 0.2\delta$. The criterion can then be expressed with the flowing relation (*70*):

$$Re_D^{\frac{1}{2}} Pr^{-\frac{1}{3}} < \sqrt{\frac{DD_{laser}\pi f}{\alpha_o}} \tag{3.7}$$

Given that $D = 25.4$ mm and $D_{laser} = 10$ mm in our experimental work, and using α_o of the molten salt (*75*), when f is within 0.5 to 2 Hz, $Re_D^{\frac{1}{2}} Pr^{-\frac{1}{3}} < 100$, the forced convection effect is neglected. When $Re_D^{\frac{1}{2}} Pr^{-\frac{1}{3}} \gg 100$, the forced convection effect is no longer negligible. k_{eff}

that is higher than the k_o of the flow fluid is thus obtained in the measurement. For convenience, we define $\lambda = \frac{k_{eff}}{k_o}$ as the normalized thermal conductivity of the flowing fluids. It is an indicator that describes the relative change in the thermal transport property of the flowing fluids due to the convection effect.

3.4.Results and discussions

3.4.1. MPR measurement results

Table 3.2 summarizes the experimental conditions of the MPR flowing molten salt measurements. The measurement temperatures *T* = 520 and 580 ^{o}C were selected. They are within the proposed operating temperatures (between 520 to 720 ^{o}C) of the chloride-salt-based CSP plants. (*7*), albeit at the lower end of this temperature window. In addition, these temperatures ensure the safety and good operational condition of the molten salt flow loop, based on the considerations of the maximum operating temperatures of several components of the loop, such as the valve, and flow meter, which are all limited to 650 ^{o}C (*121*), and the corrosion and mechanical stress issues (*123*). Nevertheless, the operational conditions including the temperature selected in this study are for demonstrating the feasibility of *in-situ* MPR measurements on flowing molten salts. The MPR technique itself is non-contact and has been well-calibrated with radiation heat loss and other factors associated with high-temperature operations. Therefore, it can be extended to higher temperatures such as 750-800 ^{o}C, provided that the thin Inconel window can be replaced by thicker and/or more robust materials, which we shall discuss in detail in *Section 3.4.2*. Typically, the practical molten salt flow velocity ranges from 0.5 to 4.0 m s^{-1} (Martinek et al., 2021; Robb, 2022; Zeng et al., 2022). Our selected flow velocity from 0.3 to 1.0 m s^{-1} is a wide enough flow velocity to observe the thermal transport property changes from the laminar flow-to-turbulent flow regime using our technique. The

velocity of 1.0 m s^{-1} was set as the upper boundary of the flow velocity to maintain the safe operation of the flow loop integrated with the designated MPR test section.

Table 3.2 Summary of the experimental conditions for MPR flowing molten NaCl-KCl-$MgCl_2$ measurements

Temperature T (^oC)	Average flow velocity u_b (mm s^{-1})
520	375 ± 42
	658 ± 33
	1000 ± 33
580	266 ± 28
	448 ± 35
	628 ± 38
	971 ± 16
	1040 ± 34

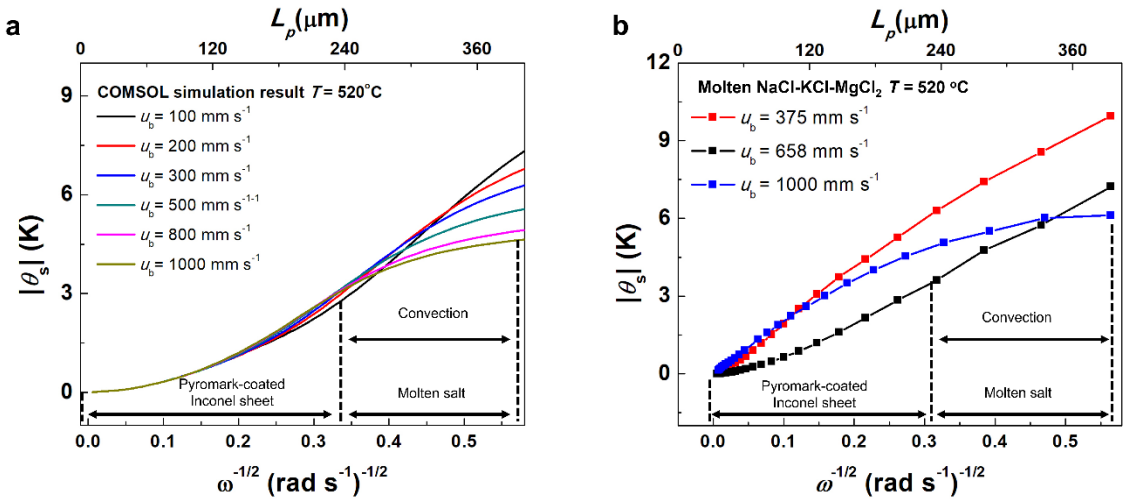

Figure 3.5 (a) COMSOL simulation result of $|\theta_s|$ *vs.* $\omega^{-\frac{1}{2}}$ for flowing molten NaCl-KCl-$MgCl_2$ measurement with various u_b ranging from 100 - 1000 mm s^{-1}; **(b)** plot of $|\theta_s|$ versus $\omega^{-\frac{1}{2}}$ of flowing NaCl-KCl-$MgCl_2$ at T = 520 °C with different u_b: 375, 658, and 1000 mm s^{-1}

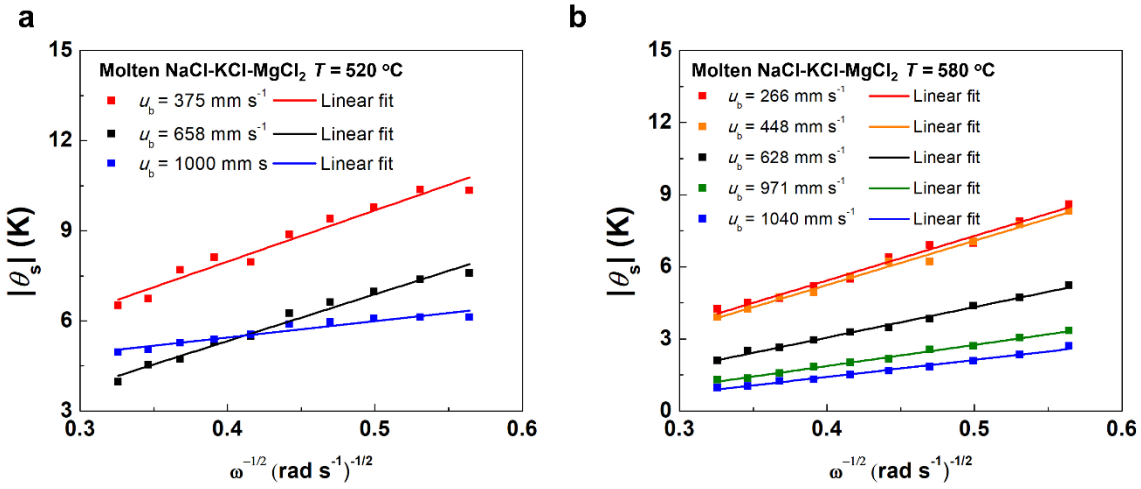

Figure 3.6 Plot of $|\theta_s|$ *vs.* $\omega^{-\frac{1}{2}}$ of flowing NaCl-KCl-$MgCl_2$ **(a)** at T = 520 °C with different u_b ranging from 375 to 1000 mm s^{-1}; **(b)** at T = 580 °C with different u_b ranging from 266 to 1040 mm s^{-1}

To illustrate the expected experimental results, we built a COMSOL model using a laminar flow module coupled with heat transfer to study the thermal response of flowing molten salt inside the MPR test section. The test section and material properties NaCl-KCl-$MgCl_2$ at T = 520 °C are from reference (*74*, *75*). **Figure 3.5a** shows the COMSOL simulation result of the MPR flowing molten salts NaCl-KCl-$MgCl_2$ measurement at T = 520 °C in the entire frequency range with u_b changes from 100 to 1000 mm s^{-1}. From the COMSOL simulated results of $|\theta_s|$ *vs.* $\omega^{-\frac{1}{2}}$, three regions are observed: the flowing molten salt region in the low-frequency range, the Inconel alloy region in the intermediate-frequency range, and the Pyromark coating region in the high-frequency region. The slopes of the $|\theta_s|$ *vs.* $\omega^{-\frac{1}{2}}$ plots in the low-frequency region decrease gradually with the increasing u_b. When u_b > 500 mm s^{-1}, the slope starts to plateau. It is a result of the forced convection effect, equivalently higher k_{eff} at high flow velocity, leading to a less prominent $|\theta_s|$. **Figure 3.5b** shows experimental $|\theta_s|$ *vs.* $\omega^{-\frac{1}{2}}$ plot of molten NaCl-$MgCl_2$-KCl at T = 520 °C with different u_b of 0.375, 0.658, and 1.000 m s^{-1}. Despite the discrepancy between our experimental results and the COMSOL simulation results, we could observe the change in the slope in the low-frequency region. It is consistent with the COMSOL simulation results. The $|\theta_s|$ *vs.* $\omega^{-\frac{1}{2}}$ curves show the transition from the molten salt region to the Pyromark-coated Inconel sheet region when the modulation frequency increases. The slopes of the $|\theta_s|$ *vs.* $\omega^{-\frac{1}{2}}$ plots in the low-frequency region decrease along with increasing u_b. At u_b = 1.0 m s^{-1}, the slope nearly plateaus. It indicates the significant convection effect at high flow velocities, as the model predicts. Using Eqs. (3-4), k_{eff} of the flowing molten salts was obtained. The $|\theta_s|$ *vs.* $\omega^{-\frac{1}{2}}$ data

of the flowing molten salt in the low-frequency range (0.5 – 1.5 Hz) at T = 520 °C and T = 580 °C with different u_b ranging from ~ 0.27 to 1.04 m s^{-1} are included in the **Figure 3.6.**.

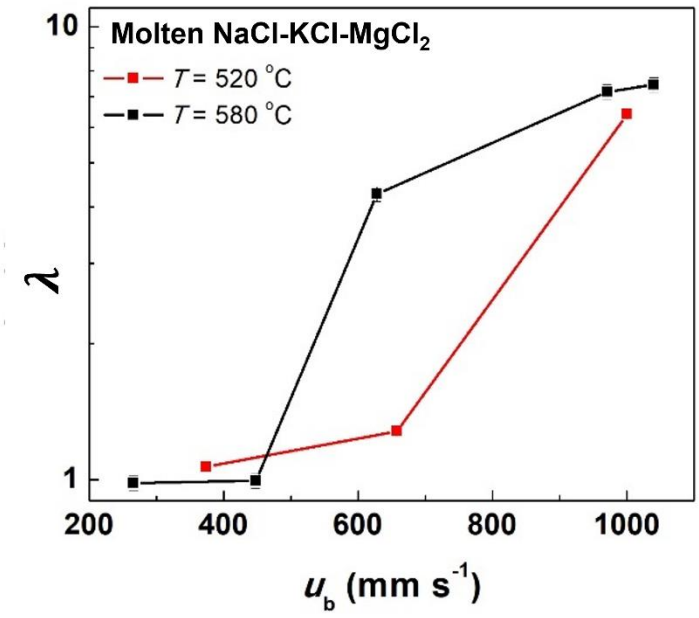

Figure 3.7 Plot of the normalized thermal conductivity $\lambda = \frac{k_{eff}}{k_o}$ of flowing salt as a function of fluid flow velocity u_b.

Figure 3.7 shows the normalized thermal conductivity λ as a function of u_b. λ approaches unity when the flowing molten salts exhibit k_o (*75*); otherwise, it increases as a function of T and u_b. From the experimental results, λ of flowing molten salt is a strong function of u_b. When u_b is small (u_b < 0.4 m s^{-1}), we obtained λ close to 1. At T = 520 °C, the measured k_{eff} of molten NaCl-$MgCl_2$-KCl with u_b= 0.375 m s^{-1} is 0.477 W m^{-1} K^{-1}; at T = 580 °C, the measured k_{eff} of the molten salt u_b= 0.266 m s^{-1} is 0.424 W m^{-1} K^{-1}. Upon u_b increases, λ increases substantially. At T = 520 °C with u_b = 1.0 m s^{-1}, κ increases to 6.40; at T = 580 °C with u_b = 1.05 m s^{-1}, λ increases to 7.44. The enhancement in the k_{eff} is due to the forced convection effect in the flowing molten salt. The k_{eff} enhancement of flowing molten salt NaCl-$MgCl_2$-KCl

behaviors similarly at both T = 520 °C and 580 °C. However, the k_{eff} enhancement at T = 580 °C begins at a slightly lower u_b. It implies that the forced convection effect is more significant at higher temperatures, due to a lower viscosity of the molten salt.

The experimental results are further analyzed by plotting λ as a function of Re_D and $Re_D{}^{\frac{1}{2}}Pr^{-\frac{1}{3}}$ respectively, as shown in **Figure 3.8a** and **Figure 3.8b**. On the λ *vs.* Re_D plot shown in **Figure 3.8a**, λ increases monotonically as a function of Re_D. For flowing fluid in a smooth tube, the flow transits to turbulent when $Re_D \sim 4000$ and the turbulence is fully developed when $Re_D > 10{,}000$ (*79*). It explains the enhancement of λ at large Re_D values and it is consistent with the results shown in **Figure 3.7**. **Figure 3.8b** shows that when the flowing molten salt has relatively small $Re_D{}^{\frac{1}{2}}Pr^{-\frac{1}{3}}$ values, the measured λ converges to unity; when $Re_D{}^{\frac{1}{2}}Pr^{-\frac{1}{3}}$ increases and much beyond 100, the measured λ increases significantly. It is consistent with our analysis of the criteria of intrinsic thermal conductivity measurement of flowing fluids. Our previous flowing D.I. water and thermal oil results are also plotted in **Figure 3.8b** for comparison.

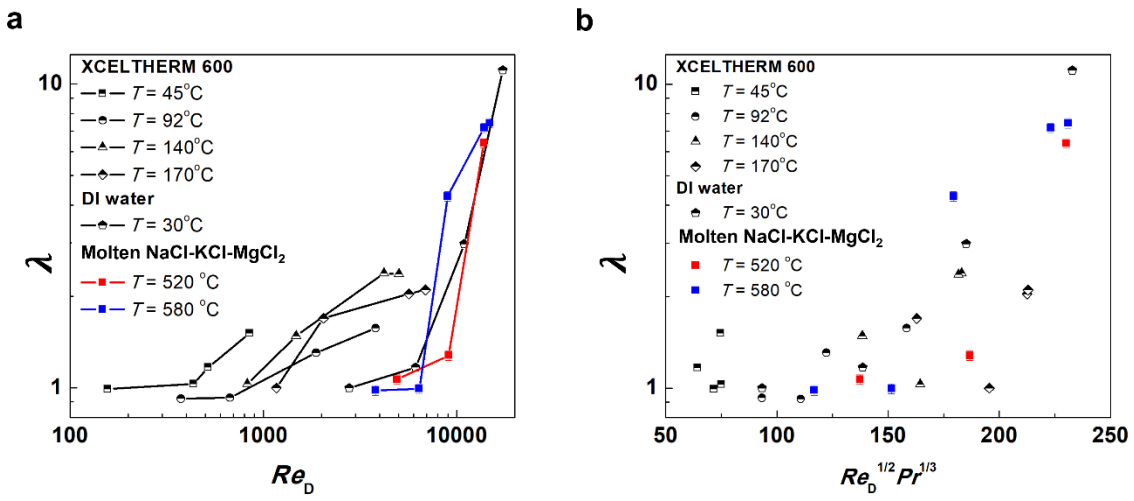

Figure 3.8 Analysis of the forced convection effect in flowing molten salt. **(a)** normalized thermal conductivityλ as a function of Re_D number for molten salt; and **(b)** normalized thermal conductivity λ of flowing molten salt as a function of $Re_D^{\frac{1}{2}}Pr^{-\frac{1}{3}}$ at different temperatures. Our previous flowing D.I. water and Xceltherm 600 measurement data using the MPR method are included for comparison (*70*).

It is rarely peculiar that our experimental results shown in the $|\theta_s|$ *vs.* $\omega^{-\frac{1}{2}}$ plots (**Figure 3.6b**) exhibit different trends, especially in the intermediate-to-high frequency range, compared to COMSOL model prediction. The reason is still not clear. The scale of the molten salt loop that we used in this work is much larger than the setup shown in other similar studies (*121*, *124-126*), thus, complicating the measurements and the stability of the molten salt flow. On the other hand, corrosion of the measurement window could also cause the discrepancy. As we mentioned in *Section 3.3.1*, a thin layer of Pt was coated on the back side of the 100 μm Inconel 625 measurement MPR window on the test section to prevent corrosion. However, the corrosion of the thin Inconel sheet was still inevitable. According to the studies of the corrosion of Inconel alloy under molten chloride salts (*127*), corrosion would make the alloy thinner due to the depletion of individual metal components. On the interface of the corroded alloy, there is a formation of a metal oxide layer, which could show different thermophysical properties

compared to the original alloy. The corrosion issue could be attributed to the discrepancies in the intermediate-to-high-frequency range where the thermal response of the test section is more dominant by the thermophysical properties of the alloy and the coating. Nevertheless, according to Eqs. (3.1-3.2), the low-frequency thermal response is still more determined by the thermophysical property of molten salt. This explains that our molten salt thermal conductivity calculation is less affected by the effects of molten salt corrosion of the measurement window.

3.4.2. Discussion on the k_{eff} calculation using the differential method

Based on Eqs. (3.1-3.4), the thermal conductivity of fluids can be obtained using a differential method. The simplicity of the method allows us to measure k_o without exactly knowing the required physical quantities (e.g., heat flux, and laser spot size). However, one has to be cautious about applying this method in three-layer measurements. The simplification shown in Eq. (3.1) is only valid if the intermediate layer exhibits a negligible thermal resistance (i.e., negligible thickness). The intermediate layer contributes a heat spreading effect, thus, affecting the heat transfer from the top layer (Pyromark coating) to the bottom layer (molten salt layer). The calculation of k_o would lead to a certain deviation if the differential method is applied. To illustrate this, we compare the simulation $|\theta_s|$ *vs.* $\omega^{-\frac{1}{2}}$ curves of a three-layer structure (Pyromark coating, 100 μm Inconel alloy, and molten salt layer) and that of a two-layer structure (Pyromark coating, and molten salt layer). It is included in **Figure 3.9**. The slopes in the low-frequency region of the $|\theta_s|$ *vs.* $\omega^{-\frac{1}{2}}$ show a deviation of around 7 %. The deviation can be minimized if the thickness of the Inconel sheet is further reduced.

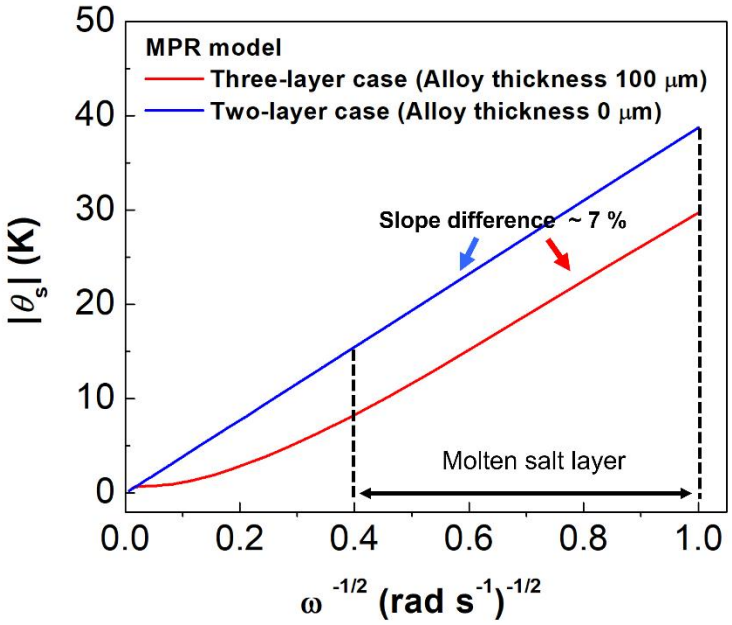

Figure 3.9 $|\theta_s|$ *vs.* $\omega^{-\frac{1}{2}}$ plots of a three-layer structure (Pyromark coating, 100 μm Inconel alloy, and molten salt layer) and a two-layer structure (Pyromark coating, and molten salt layer) simulated by the MPR model. The input parameters are the thermophysical properties of Pyromark coating, Inconel alloy and molten salts at T = 500 °C (*69*, *74*, *75*). The slopes of the curves in the low-frequency region show a deviation of around 7%.

In our case, the intermediate layer in our study is a 100 μm Inconel sheet. The choice of the Inconel sheet thickness is a compromise between the mechanical strength of the Inconel sheet to contain the flowing molten salt inside the test section and the sensitivity of the amplitude signal ($|\theta_s|$) in the low-frequency region. Nevertheless, in the differential method, we can indicate the relative change of k_{eff} of flowing molten salt by dictating the change in the low-frequency slopes in the $|\theta_s|$ *vs.* $\omega^{-\frac{1}{2}}$ plots. A detailed sensitivity analysis of the thermal response is included in **Figure 3.10**. The increases in the alloy layer thickness could reduce the sensitivity of the thermal measurements. Therefore, to maintain the high sensitivity of the thermal conductivity measurement to the molten salt in the MPR technique while using the Inconel 625 as a compatible structural material for the current setup, a small thickness of 100 μm is needed

for Inconel 625. The small thickness, however, would limit the total exposure time and temperature of this window to the molten chloride salt, due to the possibility of corrosion.

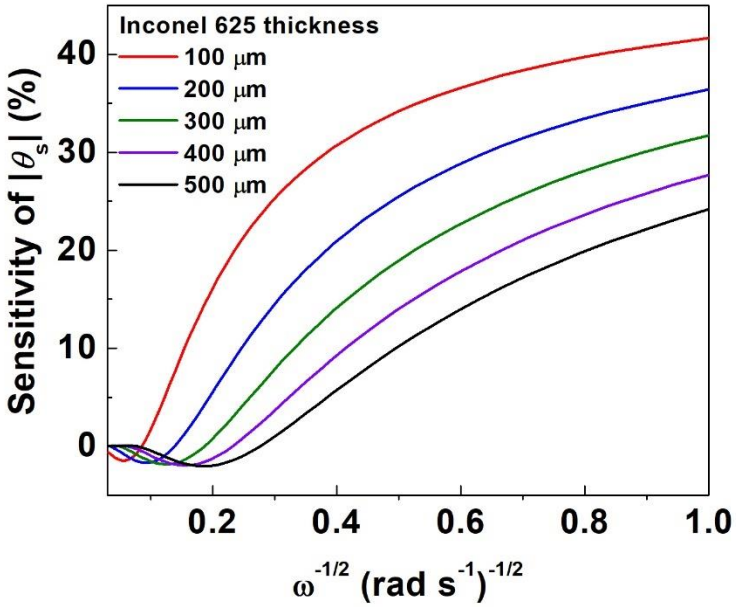

Figure 3.10 Sensitivity of $|\theta_s|$ to molten salt thermal conductivity k_o, for Inconel window layers with thickness varying from 100 μm to 500 μm.

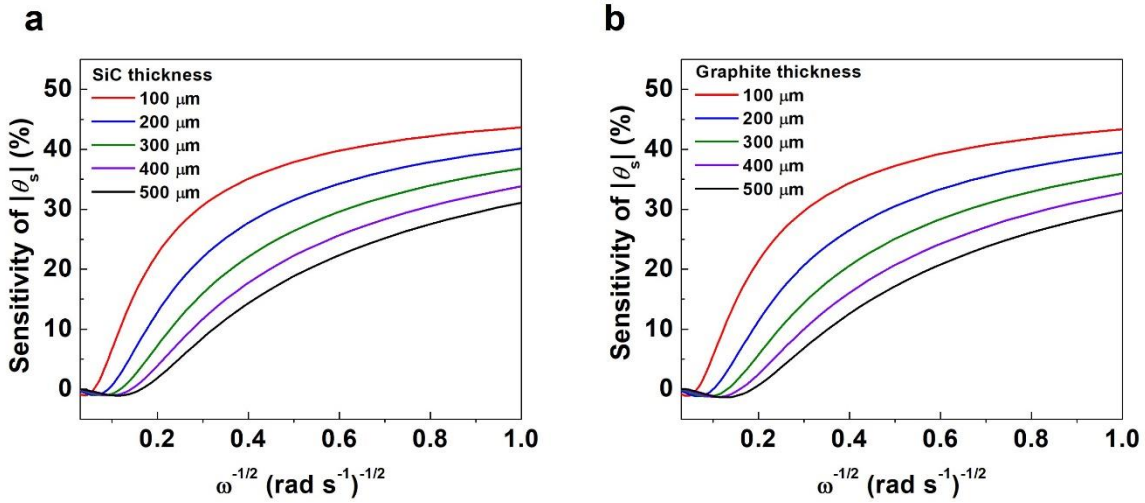

Figure 3.11 Sensitivity of $|\theta_s|$ to molten salt thermal conductivity k_o, for **(a)** SiC and **(b)** Graphite window layers with thickness varying from 100 μm to 500 μm.

The materials and their thickness limitation can potentially be resolved by using high thermal conductivity materials such as Silicon Carbide (SiC), graphite, and their composites in the MPR window, as these materials are known to be as stable structural materials for molten-salt-based CSP and TES facilities (Ding and Bauer, 2021; Ding et al., 2019; Ibrahim et al., 2021; Wang et al., 2022). They showed desirable corrosion resistance and excellent mechanical properties at high temperatures. Based on the thermophysical properties of SiC and graphite which have around 6 and 3 times higher thermal conductivity at high temperatures, respectively, compared to that of Inconel 625 (Pavlov et al., 2017; Sparavigna, 2002; Wei et al., 2013), we did the sensitivity analysis of the thermal response in our MPR experiments when these materials are used as the window layer (the second layer in the measurement). The results are shown in **Figure 3.11a** and **Figure 3.11b**. From this analysis, the sensitivity of the measurement maintains around 40 % in the low-frequency region for 200 μm thick SiC and graphite. As the SiC and graphite have better intrinsic molten salt corrosion resistance and can be made thicker as the MPR window for sensitive measurements, we believe they could be suitable candidate materials for long-term *in-situ* experiments.

3.5. Heat transfer coefficient prediction using Gnielinski's correlation

It is of interest to study the convective heat transfer coefficient h of flowing NaCl-KCl-$MgCl_2$ inside the smooth pipes. Zhang *et al.* (*121*) recommend that Gnielinski's Correlation is a better correlation for current molten chloride salt systems. Gnielinski's correlation is given by (*79*):

$$Nu = \frac{(\frac{f}{8})(Re-1000)Pr}{1+12.7\left(\frac{f}{8}\right)^{0.5}\left(Pr^{\frac{2}{3}}-1\right)} \tag{3.8}$$

where $Nu = \frac{hD}{k_o}$ is the Nusselt number; f is the Darcy friction factor (*79*):

$$f = (0.79\,\mathrm{Ln}(Re_D) - 1.64)^{-2} \tag{3.9}$$

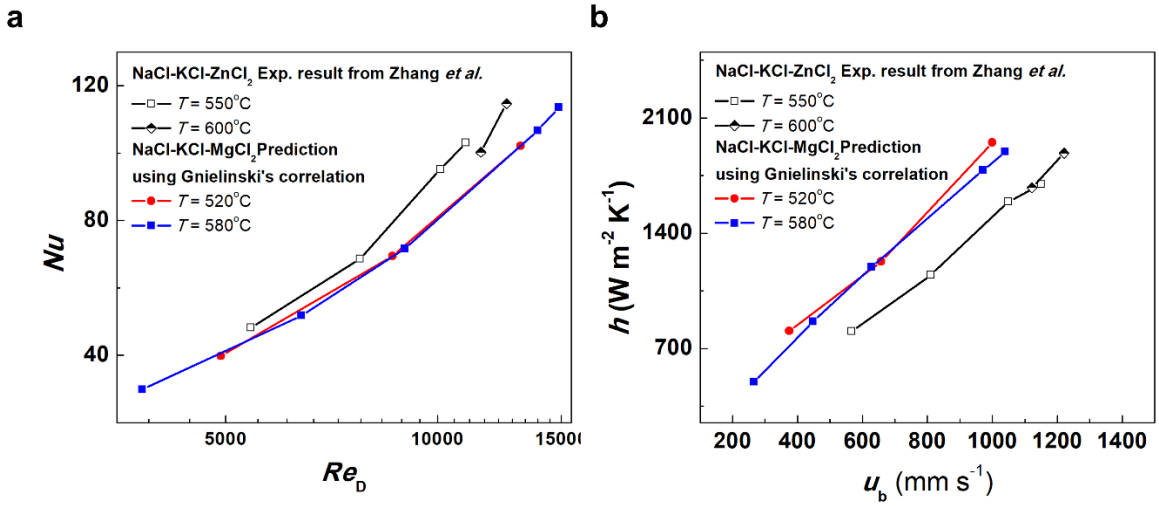

Figure 3.12 The predicted **(a)** Nusselt number (*Nu*) and **(b)** Heat transfer coefficient (*h*) of molten NaCl-KCl-$MgCl_2$ using Gnielinski's correlation. The results from Zhang *et al*. (*121*) of flowing molten NaCl-KCl-$ZnCl_2$ are plotted on the same graphs for comparison.

Gnielinski's correlation is valid when $0.5 < Pr < 2000$ and $3000 < Re_D < 5 \times 10^6$. Using Eqs. (8-9), we calculate Nu and h values the flowing molten salt. The measured intrinsic thermal conductivity of the flowing molten salt (k_o = 0.477 W m^{-1} K^{-1} when T = 520 °C and u_b= 375 mm s^{-1}; k_o = 0.424 W m^{-1} K^{-1} when T = 580 °C and u_b= 266 mm s^{-1}), the flow velocity in our study, and the known thermophysical properties of the molten salt from reference (*75*) are the input parameters. **Figure 3.12a** and **Figure 3.12b** show the Nu *vs.* Re_D, and h vs. u_b plots at T = 520 and 580 °C, respectively. The measured values of Nu and h of molten NaCl-KCl-$ZnCl_2$, another eutectic chloride salt with similar compositions, are also plotted alongside for comparison (*121*). The predicted h of molten NaCl-KCl-$MgCl_2$ increases linearly with u_b. It is the result of the turbulence of the flow at high flow velocities. The predicted h of molten NaCl-KCl-$MgCl_2$ shows around 20 % higher than the measured h of molten NaCl-KCl-$ZnCl_2$ in the entire flow velocity

range. The discrepancy can be attributed to the limited prediction ability of the correction and the difference in the intrinsic thermophysical properties of these two molten eutectic chloride salts (*75*, *117*). Yet, the predicted *h* of molten NaCl-KCl-$MgCl_2$ using Gnielinski's correlation can provide a very valuable reference and evaluation of the heat transfer performance of molten chloride salt for CSP applications.

3.6. Conclusion

This paper reports the first *in-situ* thermal conductivity measurement of flowing molten salt (NaCl-KCl-$MgCl_2$) from 520 and 580 ^oC using the MPR method with flow velocities ranging from around 0.3 to 1.0 m s^{-1}. The intrinsic thermal conductivity of the molten salt flow can be obtained when the flow velocity is low and when the criterion $Re_D^{\frac{1}{2}}Pr^{-\frac{1}{3}} < \sqrt{\frac{DD_{laser}\pi f}{\alpha_o}}$ is satisfied in the measurement. In our experimental setting, the criterion is given by $Re_D^{\frac{1}{2}}Pr^{-\frac{1}{3}} < 100$. It is consistent with our previous MPR flowing fluid measurements of D.I. water and thermal oil. We were able to detect the relative change of k_{eff} as the turbulence of the molten salt flow developed. We could not only measure the intrinsic thermal conductivity of flowing molten salt and the relative change in the effective thermal conductivity under controlled flow conditions but also the heat transfer coefficient of the molten salt using the MPR method. The heat transfer coefficient of molten NaCl-KCl-$MgCl_2$ was obtained using Gnielinski's correlation together with the measured intrinsic thermal conductivity. The heat transfer coefficient of molten NaCl-KCl-$MgCl_2$ obtained in our measurement shows good agreement with the experimentally determined *h* of another eutectic chloride salt with similar compositions. Our heat transfer coefficient calculation of molten NaCl-KCl-$MgCl_2$ provides a useful reference and evaluation of molten chloride salt heat transfer performance for CSP applications. The work demonstrates that

the MPR can serve as an *in-situ* diagnostic tool to monitor the thermal transport property of molten salts flowing in the loop. It also opens the potential to apply the MPR technique to on-site facilities for *in-situ* measurement of other high-temperature HTFs.

Acknowledgements

Chapter 3 is a full reprint of **K. M. Chung,** Y. Zhang, J. Zeng, F. Haddad, S. R. Adapa, T. Feng, P. Li, R. Chen. "*In-situ* Thermophysical Measurement of Flowing Molten Chloride Salt Using Modulated Photothermal Radiometry" *Solar Energy* 256 (2023): 112124. For this publication, K. M. Chung performed experiments, data analysis and manuscript writing.

Chapter 4. *In-situ* thermal conductivity measurement revealing kinetics of thermochemical reactions

4.1. Introduction

Thermochemical materials (TCMs) are being extensively studied for developing sustainable and carbon-free renewable energy technologies. TCMs can find applications in thermal energy storage (TES) (*110, 128*) and fuel production with thermal energy from concentrated solar and other sources (*35, 129-136*) . TES is one of the crucial technologies to provide long-duration energy storage by utilizing TES materials (*27, 33, 137*). With the integration of TES systems into renewable power plants, for example, concentrating solar power (CSP) plants, the resilience of electrical generation can be secured. TES using TCMs is competitive because thermochemical storage materials have higher energy/power densities and smaller heat losses compared to sensible and latent heat storage (*19*). Promising TCMs include redox-active metal oxides (for example, Co_3O_4-CoO, CuO-Cu_2O, Mn_2O_3-Mn_3O_4) (*138-140*) and hydroxides ($Ca(OH)_2$ (*25, 141*)). Other than TES application, taking advantage of the use of thermal energy from the abundant concentrated sunlight, TCMs play an important role in various solar-driven chemical processes, including air separation (*129, 130*), carbon dioxide (*35, 131, 136*), and water splitting (*35, 132, 133, 135, 136*), providing an alternative route to more sustainable fuel production.

The thermal transport properties of TCMs are important parameters to evaluate the kinetics and the overall efficiency of TES systems and chemical reactors. Researchers have employed different techniques to obtain the thermal conductivity of TCMs (*33*). Steady-state method, transients hot-wire (THW), and hot disk transient plane source (TPS) method (*142*) are

conventional contact methods for measure thermal conductivities of TCMs (*143-145*). However, each method has its limitations. The steady-state method requires a long measurement time and tedious setup preparations that depend on the size and the geometry of the test sections. The hot wire in the THW method can be easily damaged by corrosive and highly reactive samples. Although coating a thin protective layer (i.e., Al_2O_3) on the wires (*16*) can prevent damage, it complicates the setup preparation and the evaluation of thermal conductivity. The measurements of low-thermal-conductivity materials using the TPS method may be challenging because of the lateral heat spread and heat loss in the insulation layer of the sensor (*146, 147*). In addition, the measurement techniques mentioned above (steady-state, THW, and TPS methods) are all contact-based methods. The temperature sensors may be damaged at high temperatures, leading to degradation and measurement errors. Constant replacement of the sensors and other components of the setup is required at the expense of costly and regular maintenance. Laser flash analysis (LFA) is a non-invasive method to measure the thermal diffusivity of TCMs based on the transient thermal response of the sample upon pulse laser heating (*148*). Despite its success in popularity and commercialization, LFA is not suitable for *in-situ* measurements due to factors such as the constraint on the sample thickness imposed by the backside thermometry. The LFA method is also not capable of monitoring the thermal transport properties of TCMs in real-time. Considering this, new techniques for continuously evaluating TCM thermal transport properties are needed.

Recently, a novel non-contact measurement technique, namely, modulated photothermal radiometry (MPR), has been developed by some of the authors. It is a frequency-domain technique where the oscillating thermal response of the sample subjected to a periodic laser heat flux is utilized for thermal characterization. It is a highly versatile technique that accurately

measures the thermal conductivity of samples in various forms, including bulk solid, thin coatings, granular media, and static and flowing molten salts (*69, 70, 149, 150*). Here, we report the *in-situ* monitoring of thermochemical reactions using modulated photothermal radiometry (MPR). Two thermochemical materials, namely, calcium hydroxide ($Ca(OH)_2$), and $Ba_{0.15}Sr_{0.85}FeO_{3-\delta}$ (BSF1585) were selected for examination. $Ca(OH)_2$ /CaO thermochemical couple is widely applied for high-temperature TES (*141, 151*). Throughout the *in-situ* monitoring of $Ca(OH)_2$ pellet at the temperature of 200-380 °C, the thermal conductivity evolution of $Ca(OH)_2$ was captured and correlated to the kinetics of the dehydration reactions of $Ca(OH)_2$. BSF1585 is an emerging thermochemical material for air separation (*129, 130, 152*). Upon heating, the change in thermal conductivity of BSF1585 was measured using the MPR technique. The correlation of the thermal conductivity and the oxygen non-stoichiometry of BSF1585 was evaluated. The work shows two significant impacts to the research communities. Firstly, it provides a non-invasive, potentially high-throughput diagnostic tool for monitoring the thermal transport properties of TCMs. It would be valuable to the scientific community and industrial sectors that require precise thermal conductivity data of TCMs for thermal systems and reactor design optimization. Secondly, for TCMs that show observable changes in thermal transport properties, a correlation between thermal conductivity and the conversion fraction of the reaction can be established for monitoring the reaction kinetics based on thermal characterization. The thermal transport property changes in TCMs (i.e., perovskites) captured by the MPR thermal characterization method can potentially shed new light on the kinetics study of the chemical reactions.

4.2. Experiments

4.2.1. MPR setup and its principle

Figure 4.1 shows the schematic of the MPR setup and the workflow of *in-situ* monitoring of TCMs. The details of the MPR setup are reported in refs (*69*). A continuous laser (Naku Technology Co., Ltd, CivilLaser, LSR445CP-12W-FC) was modulated by a waveform generator (Bell Electronics NW, Inc., Agilent 33120A) to provide an oscillating heat flux ($q_s(\omega) = q_s e^{j\omega t}$) at an angular frequency ω. The laser was converted from a Gaussian beam profile into a top-hat beam (uniform) profile using a beam shaper (EKSMA Optics, GTH-3.6-1.75FA) to ensure a uniform heat flux. The samples were then mounted on a designated high-temperature sample holder, as described in ref (*69*). The holder was installed with insertion heaters for controlling the sample temperature. The thermal response of the sample was recorded using an ultra-fast PbSe detector (Thorlabs, PDA20H-EC, 34 ms response time) for thermal characterization. The actual surface temperature (θ_s) was monitored by a high-temperature pyrometer (Lumasense Technologies IGA 320/23-LO). The oscillating voltage readings (V_s) from the PbSe detector were extracted using the lock-in amplifier (Bell Electronics NW, Inc., Stanford Research System SR830). Based on the calibration curve of $|\theta_s|$ *vs.* V_s, the temperature oscillation of a sample can be obtained based on the $|\theta_s| - V_s$ conversion. Taking advantage of the frequency-domain nature of the MPR technique, the thermal penetration depth $L_p = \sqrt{\frac{2\alpha}{\omega}}$, where α is the thermal diffusivity, was controlled by varying the modulation frequency f. In this work, f is typically swept from 0.6-20 Hz, which is equivalent to L_p ~ 100-500 μm. The samples were measured from a starting temperature, where no reaction occurred, to a targeted reaction temperature T_{rxn} for study the temperature-dependent thermal conductivity. The samples were also held at T_{rxn} for

a longer period up to 5 h, while they were being measured at specific time intervals to observe the dynamic change of the thermal conductivity at T_{rxn}.

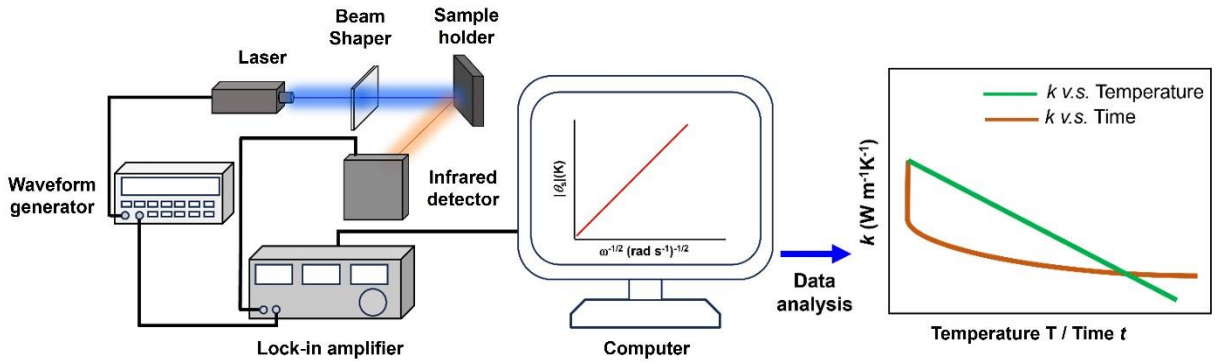

Figure 4.1 Schematic showing the *in-situ* monitoring of TCMs using the MPR technique. The thermal response of the sample is collected and processed digitally. The measured thermal conductivity as functions of temperature and time is then obtained after data analysis

The heat transfer problem in the MPR measurement can be described using the one-dimensional (1D) semi-infinite heat transfer model of a two-layer sample with an oscillating uniform heat flux imposed on the front side. In the low-frequency limit where the thermal penetration depth (L_p) is much longer than the coating thickness, θ_s is given by (*69, 70*):

$$\theta_s = q_s\left(\frac{e^{-\frac{\pi}{4}j}}{e_s\sqrt{\omega}} + R_f\right) \tag{4.1}$$

where e_s is the thermal effusivity of the substrate, R_c is the thermal resistance of the coating. By obtaining the slope (m) of the $|\theta_s|$ *vs.* $\omega^{-\frac{1}{2}}$ plot, the thermal effusivity e_s of the sample (substrate) is determined. A reference sample (borosilicate glass) is introduced for heat flux calibration. Borosilicate glass was chosen as the reference sample because it has well-established thermophysical properties (*71*). Using a differential method, e_s can be obtained by comparing the slopes of the $|\theta_s|$ *vs.* $\omega^{-\frac{1}{2}}$ plot of the reference with a standard thermal effusivity (e_{ref}). e_s can be obtained as given in Eq. (4.2), by comparing with the reference:

$$e_o = \frac{m_{ref}}{m_o} e_{ref} \quad (4.2)$$

The measured e_s is then converted to k using the following relationship:

$$k = \frac{{e_o}^2}{\rho_s c_p} \quad (4.3)$$

Since the modulation frequency is from 0.6-20 Hz, it takes less than 2 s to acquire the thermal response from the sample for data analysis. At each temperature point, the measurement takes about 15-20 min (*149*). It allows one to apply the MPR technique as an *in-situ* diagnostics to measure the thermal conductivity of TCMs as a function of temperature and reaction time.

4.2.2. Sample preparation and materials characterization

Calcium hydroxide ($Ca(OH)_2$) powders (Fisher Scientific, CAS:1305-62-0, certified grade) were commercially available. $Ca(OH)_2$ powders were pelletized using a cold-pressed method. Appropriate amounts of $Ca(OH)_2$ were pressed using a hydraulic press to form a pellet of 10 mm diameter and ~ 1 mm thickness, with a porosity of 53.0 %. BSF1585 perovskite was synthesized using a modified Pechini method (*130, 152*). The as-synthesized BSF1585 powders were pressed to form a pellet of 13 mm diameter and 1 mm thickness with a porosity of 23.0 %. The detailed procedures of BSF1585 sample preparation are documented in refs (*130, 152*). Prior to the MPR measurement, the white $Ca(OH)_2$ pellet was coated with a thin layer of graphite (10-15 μm) for laser absorption and infrared emission in the measurement. On the other hand, BSF1585 pellets were measured under two conditions: with and without laser absorptive Pyromark coatings. Pyromark coating is a silicone-based black paint that can withstand high-temperatures of up to 1000 ^oC (*153*). It was found that BSF1585 reacted with Pyromark coatings to form secondary phases at elevated temperatures, which was detectable in the MPR

measurement. It will be discussed in detail in *Section 3.2*. The intrinsic thermochemical reactions at high temperatures without contamination were obtained in the BSF1585 pellet without the Pyromark coating. BSF1585 has a dark gray color, so it has high absorptance and infrared emittance. Scanning Electron Microscopy (SEM) (FEI Quanta 250 scanning electron microscope) was used to examine the surface morphology of $Ca(OH)_2$ and BSF1585. The X-ray diffraction (XRD) pattern of each sample was obtained using the Rigaku Smartlab X-ray diffractometer (Cu Kα, λ = 0.15418 nm) as the radiation source.

4.2.3. The study of the effect of the Pyromark coatings on BSF1585 perovskite using TGA

Thermogravimetric analysis (TGA) (Netzsch STA 449 F3 Jupiter) was used to study the effect of the Pyromark coatings on BSF1585 at elevated temperatures The detail TGA measurement procedure was documented in ref (*152*). The BSF1585 pellets with and without Pyromark solution attached were placed on a platinum foil-covered alumina crucible for measurement. During the measurements, the samples were heated to 650 °C and then cooled back to room temperature with heating/cooling rates of 20 K min^{-1} under a 20% O_2/N_2 gas environment. The mass change (Δm) of the sample was recorded as a function of time.

4.3. Results and Discussion

4.3.1. $Ca(OH)_2$

The obtained $|\theta_s|$ *vs.* $\omega^{-\frac{1}{2}}$ raw data of $Ca(OH)_2$ measurements are included in **Figure 4.2a**. Using Eqs. (4.2-4.3), the measured k of $Ca(OH)_2$ was extracted. The apparent density of the pellet was measured based on the mass and the volume of the pellet. The specific heat capacity was extracted from ref (*154*). **Figure 4.2b** shows the measured k *vs.* T of the pelletized $Ca(OH)_2$,

from T = 250 to 380 °C. Typically, $Ca(OH)_2$ undergoes dehydration reactions at T_{rxn} of 450 to 500 °C (*30*, *155*):

$$Ca(OH)_2(s) \leftrightharpoons CaO(s) + H_2O(g) \quad (4.4)$$

In our measurement, T_{rxn} was fixed as 380 °C to allow for slower dehydration kinetics for monitoring k of the sample using the MPR technique (*156*).

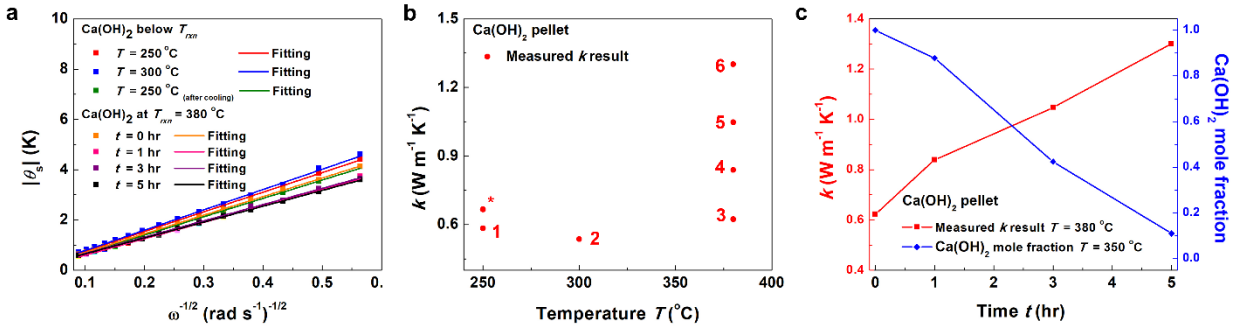

Figure 4.2 MPR measurement results of $Ca(OH)_2$: **(a)** *in-situ* monitoring $|\theta_s|$ *vs.* $\omega^{-\frac{1}{2}}$ raw data for $Ca(OH)_2$; **(b)** k *vs.* T plot. The numbers (1-6) alongside the data point represent the sequence of the measurements. The asterisk (*) marks the measured data point after cooling down overnight; **(c)** k *vs.* t plot at T_{rxn} = 380 °C. The mole fraction of $Ca(OH)_2$ at T = 350 °C as a function of time from ref (*156*) is plotted alongside to show the correlation between the measured k and the conversion fraction (mole).

The measured k of $Ca(OH)_2$ initially decreases slightly initially from 0.58 W m^{-1} K^{-1} at 250 °C to 0.54 W m^{-1} K^{-1} at 300 °C. It then increases to 0.62 W m^{-1} K^{-1} when $T = T_{rxn}$. Depending on the thermal treatment duration at $T = T_{rxn}$, the measured k increases from t = 1 to 5 h. **Figure 4.2b** shows the measured time-dependent k at T_{rxn} = 380 °C. The measured k slightly decreases from 250 to 300 °C, which can be explained by the intrinsic thermal transport property of the packed $Ca(OH)_2$ pellet (*25*). The abrupt change and time-dependent k trend at T_{rxn} = 380 °C (**Figures 4.2b** and **4.2c**) is evidently associated with the dehydration of $Ca(OH)_2$. The bulk thermal conductivity of CaO is higher than that of $Ca(OH)_2$ (20.0 W m^{-1} K^{-1} *vs.* 16.2 W m^{-1} K^{-1} at room temperature) (*157*, *158*). It is consistent with our observation that the ongoing

dehydration leads to a higher $k$value. The conversion fraction of $Ca(OH)_2$ to CaO at T = 350 °C as a function of time is plotted alongside in **Figure 4.2c** (*156*). It is notable that the increase in k is consistent with the experimental kinetics of $Ca(OH)_2$, suggesting that the change in thermal transport property directly correlates with the reaction kinetics. Surface morphologies of $Ca(OH)_2$ before and after the MPR measurements were examined using SEM. As shown in **Figure 4.3a**, the microstructure of $Ca(OH)_2$ shows insignificant change. The possibility of the change in k (**Figure 4.2b** and **Figure 4.2c**) due to the morphological change of $Ca(OH)_2$ pellet can be ruled out. Furthermore, after holding at 380 °C for 5 h, the $Ca(OH)_2$ pellet was cooled down to room temperature and sat overnight for moisture absorption. The sample was re-measured at the initial temperature $T = 250$ °C. The measured result is indicated by an asterisk in **Figure 4.2b**. The measured k of the identical $Ca(OH)_2$ sample was consistent with the original measured k with no reaction. In other words, our MPR results revealed the reversibility of $Ca(OH)_2$/CaO thermochemical reaction. This result further confirms that the measured k increase during the heating process was due to the reaction. In short, from the MPR measurement results of $Ca(OH)_2$, the change in thermal conductivity can be correlated with the reaction kinetics, making it possible to monitor the reactions in real-time. For example, it would be useful for examining the moisture content of hydroxides and conversion of the $Ca(OH)_2$/CaO thermochemical reaction couple during cycling.

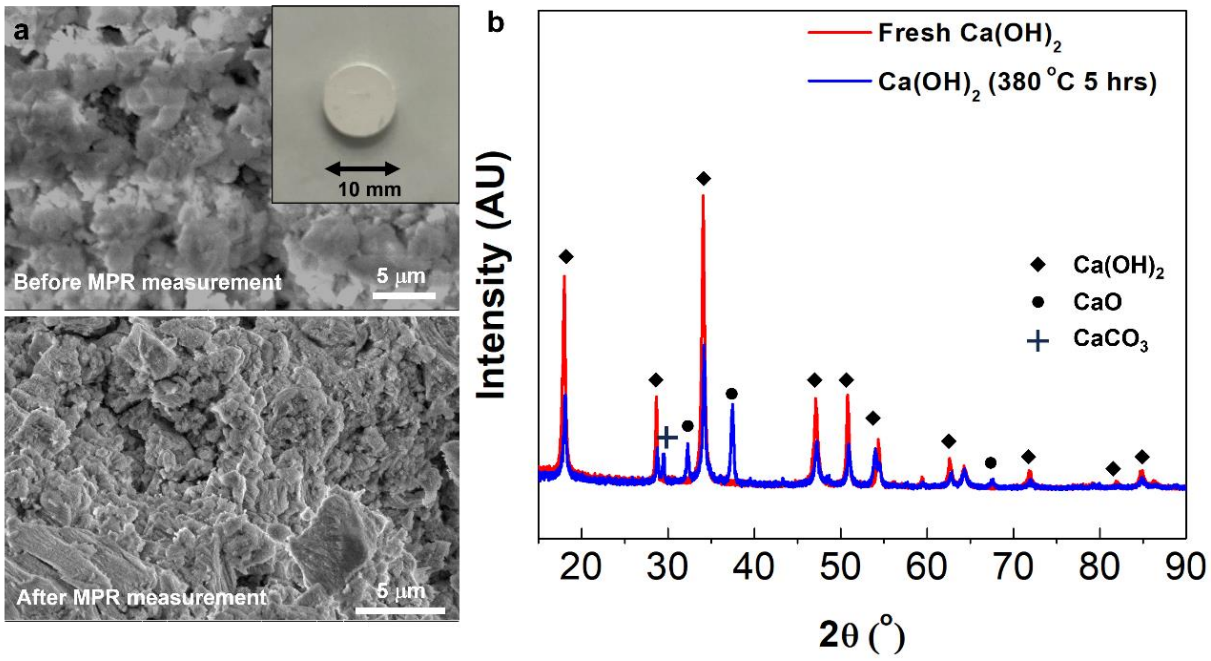

Figure 4.3 The surface morphology and crystal structure characterizations of $Ca(OH)_2$: **(a)** SEM images before and after the MPR measurements. The inset photo shows the $Ca(OH)_2$ pellet for the measurements; and **(b)** XRD patterns of $Ca(OH)_2$ before and after the MPR measurement respectively.

Figure 4.3b depicts the XRD pattern of the $Ca(OH)_2$ sample before and after the MPR measurement. The peaks of the XRD patterns were matched using MDI JADE 6.0 software. The untreated $Ca(OH)_2$ exhibits a typical hexagonal crystal structure as shown in the figure. On the other hand, the XRD patterns of the thermally treated $Ca(OH)_2$ are contributed by both $Ca(OH)_2$ and CaO, with the $Ca(OH)_2$ peak intensities significantly reduced. It is evident that the original $Ca(OH)_2$ sample was partially converted into CaO under the given MPR measurement conditions. There is a small peak attributed to the presence of $CaCO_3$. The formation of $CaCO_3$ after the measurement may be due to the direct CO_2 capture of $Ca(OH)_2$ after the thermal treatment.

4.3.2. BSF1585

BSF1585 is an emerging redox-active perovskite oxide used for air separation based on a two-step solar thermochemical cycle (*130, 152*). The reversible redox reaction is given by:

$$2Fe_{Fe}^{x} + O_{o}^{x} \leftrightharpoons 2Fe_{Fe}^{\prime} + V_{o}^{\prime\prime} + \frac{1}{2}O_{2}(g) \quad (4.6)$$

where Fe_{Fe}^{x} and O_{o}^{x} are neutral Fe and oxygen ions; $Fe_{Fe}^{\prime}$ is the negatively charged ion; and $V_{o}^{\prime\prime}$ is an oxygen vacancy. Upon heating by concentrated solar irradiation, the Fe ion in the perovskite is thermally reduced (e.g., Fe^{4+} to Fe^{3+}) accompanied by the formation of $V_{o}^{\prime\prime}$ and the release of O_2 gas. Reversibly, Fe^{3+} is oxidized to Fe^{4+} when the BSF1585 is cooled, resulting the loss oxygen vacancies due to O_2. The net result is that high-purity N_2 therefore can be separated from air during cycling.

4.3.2.1. Pure BSF1585

The *in-situ* thermal conductivities of two BSF1585 pellets were measured, one with Pyromark coating as in the $Ca(OH)_2$ sample and the other without any coating, in order to investigate the impact of potential reaction between the Pyromark coating and BSF1585. For ease of the comparison of the relative change in k induced by a change in oxygen nonstoichiometry (δ), we define a normalized thermal conductivity of $\lambda = \frac{k}{k_o}$, where k is the real-time measured thermal conductivity and $k_o$is reference thermal conductivity at the initial temperature point before thermochemical reactions. k of the BSF1585 pellets were measured for two consecutive cycles. After the first cycle, the sample was cooled to room temperature and left overnight under the ambient environment before starting the second cycle. The experimental procedures of both cycles were identical. The obtained $|\theta_s|$ *vs.* $\omega^{-\frac{1}{2}}$ raw data of uncoated

BSF1585 is shown in **Figure 4.4a**. Using Eqs. (4.2-4.3), the measured k of BSF1585 as a function of T was extracted. The bulk density of the pellet was measured based on the mass and the volume of the pellet. The Neumann-Kopp rule was used to estimate the specific heat capacity (*159, 160*). k_o of uncoated BSF1585 was measured as 2.11 W m^{-1} K^{-1} at 300 ºC. **Figure 4.4b** shows λ *vs.* T plot of uncoated BSF1585, from $T = 300$ to 650 °C. In the first cycle, λ gradually decreased, from 1.0 to 0.60, along with the increase of temperature from 300 to 650 °C. The compound energy formalism (CEF) (*130*) was used to predict δ for BSF1585 at chemical equilibrium under 1 atm air, equivalently a partial oxygen pressure P_{O2} of 0.2 bar. δ changes from 0.104 to 0.233 when T increases from 350 to 650 °C (**Figure 4.6**), indicating an increase in oxygen vacancy concentration. The change in δ is evidently responsible for the decrease in BSF1585 thermal conductivity. In the second cycle, the initial measured λ of pure BSF1585 is 0.87 at 300 ºC. It may indicate that after the sample was cooled overnight under an ambient environment, it was not fully re-oxidized Eq. (4.5). Therefore, a different λ value was obtained. In the second cycle, λ displayed a similar decreasing trend from 300 to 650 °C in the second cycle, from 0.87 to 0.60. The λ values at the reaction temperature (650 ºC) remained the same as the first cycle, indicating similar δ values when the sample reached this temperature. The decrease in BSF1585 thermal conductivity is also associated with the change in δ. However, the decreasing trend in the second cycle may be affected by a different initial oxygen vacancy concentration of the sample.

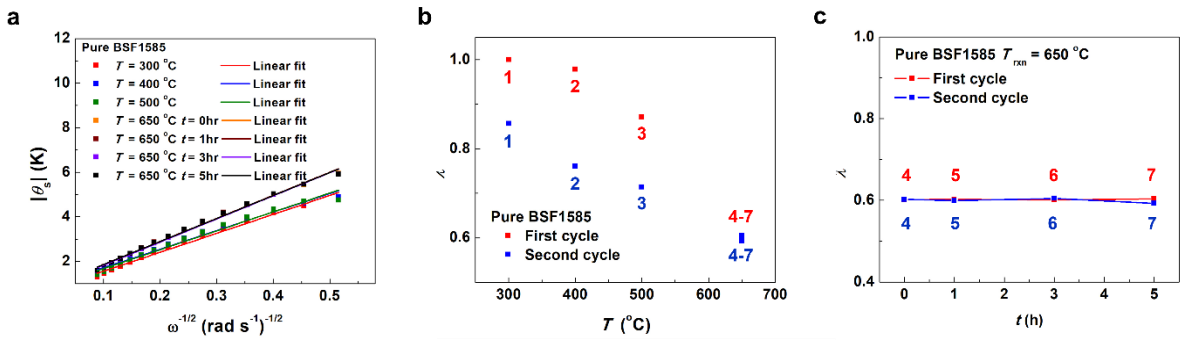

Figure 4.4 MPR measurement results of uncoated BSF1585: **(a)** *in-situ* monitoring $|\theta_s|$ *vs.* $\omega^{-\frac{1}{2}}$ raw data in the first cycle measurement; **(b)** λ *vs.* T plot. The numbers (1-7) alongside the data point represent the sequence of the measurements; and **(c)** λ *vs.* t plot at T_{rxn} = 650 °C

Figure 4.4c shows the λ of the uncoated BSF1585 as a function of time when the sample was held at T_{rxn} = 650 °C. λ of BSF1585 remains nearly constant from 0 to 5 h. This implies that δ was stable once the temperature reached T_{rxn}, showing rapid reaction kinetics. It is consistent with previous experimental results (*152*) that observed pure BSF1585 quickly reaches chemical equilibrium upon heating.

4.3.2.2. Pyromark-coated BSF1585

The thermal conductivity of Pyromark-coated BSF1585 displays entirely different temperature and time dependence. The obtained $|\theta_s|$ *vs.* $\omega^{-\frac{1}{2}}$ raw data of Pyromark-coated BSF1585 is presented in **Figure 5a**. The measured k_o of Pyromark-coated BSF was 1.20 W m^{-1} K^{-1}. **Figure 5b** shows λ *vs.* T of Pyromark-coated BSF1585, from T = 300 to 650 °C. In the first cycle, the measured λ decreased slightly from 1.0 to 0.96, along with the increase of temperature from 300 to 650 °C. In the second cycle, the initial measured λ of pyromark-coated BSF1585 is 0.99 at T = 300 °C. It indicates that after the sample was oxidized and cooled overnight under an ambient environment, it was not fully oxidized, similar to the uncoated sample. In the second cycle, λ showed a steeper decreasing trend from 300 to 650 °C in the second cycle, from 0.99 to

0.82. The decrease in BSF1585 thermal conductivity is also associated with the change in δ. Compared to the results of the uncoated BSF1585, it is obvious that the change in λ is less significant. It implies that the thermochemical reaction in Eq. (4.5) is hindered by the presence of the Pyromark coating.

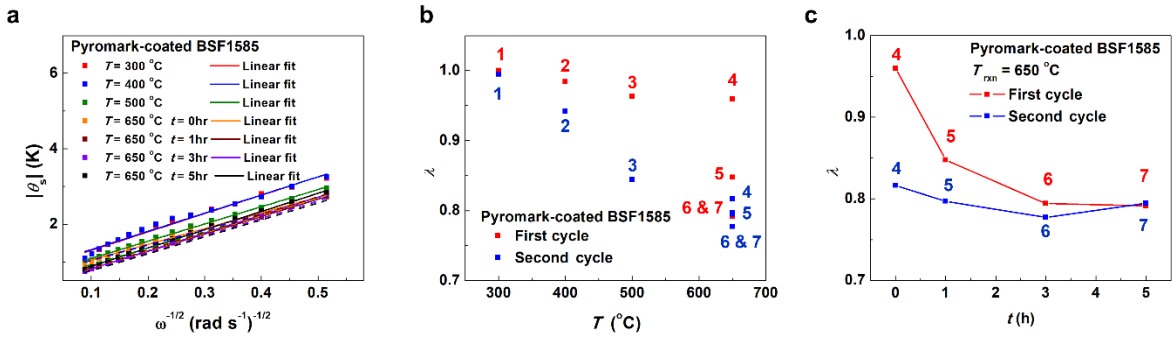

Figure 4.5 MPR measurement results of Pyromark-coated BSF1585: **(a)** *in-situ* monitoring $|\theta_s|$ *vs.* $\omega^{-\frac{1}{2}}$ raw data in the first cycle measurement; **(b)** λ *vs.* T plot. The numbers (1-7) alongside the data point represent the sequence of the measurements; and **(c)** λ *vs.* t plot at T_{rxn} = 650 °C

One can make use of the thermal conductivity of pure BSF1585 to reveal the oxygen vacancy concentrations in the specimen. By correlating the thermal conductivities obtained from pure BSF1585 (first cycle data) with the predicted δ, a $\lambda - \delta$ correlation can be established to predict the oxygen non-stoichiometry of the specimen. It is particularly useful for evaluating in real time the capacity of perovskite oxides, or oxygen carriers in general to absorb/ desorb oxygen.

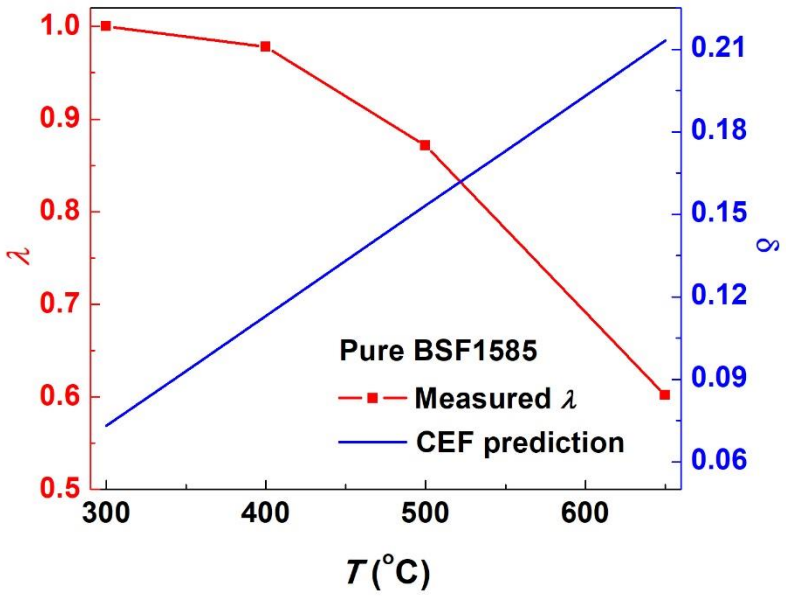

Figure 4.6 Correlation of thermal conductivity change to the oxygen non-stoichiometry of pure BSF1585 as a function of temperature based on the first cycle MPR measurement results

Figure 4.5c shows λ *vs.* t plot of Pyromark-coated BSF1585 when it was held isothermally at T_{rxn} = 650 °C for 5 h. The measured λ of BSF1585 further decreases at T_{rxn} = 650 °C. λ first substantially decreased from 0.96 down to 0.79 in the first 3 h and then eventually plateaued. The overall percentage change in the measured λ is about 17.5 %. A time-dependent λ of Pyromark-coated BSF1585 in the second cycle is also observed. The overall percentage change in λ decreases down to 2.67 %, from 0.82 to 0.79. According to a previous kinetics study of the thermochemical reactions in $SrFeO_{3-\delta}$-based perovskite oxides and our data on the uncoated BSF1585 sample, the reaction rates of both reduction and oxidation in BSF1585 are very rapid (*152*), meaning that the sample rapidly reaches chemical equilibrium with a definite thermal transport property. It is thus unexpected to observe a time-dependent thermal conductivity behavior under isothermal conditions, unless the reaction was affected by the Pyromark coating. The coating may hinder the kinetics of the thermochemical reaction,

manifested by the slower and less significant change in thermal conductivity as the temperature ramped up. The materials characterization results of both pure BSF1585 and Pyromark-coated BSF1585 further explain the statement.

Before SEM imaging, the Pyromark-coated BSF1585 pellet was polished to remove any coating and residues after the MPR measurement. As shown in **Figure 4.7a**, the surface morphologies of uncoated BSF1585 samples before the measurement and Pyromark-coated BSF1585 after the MPR measurements were examined using SEM. The surface morphology observed here is consistent with the observation of the previous study on BSF1585 (*130, 152*).

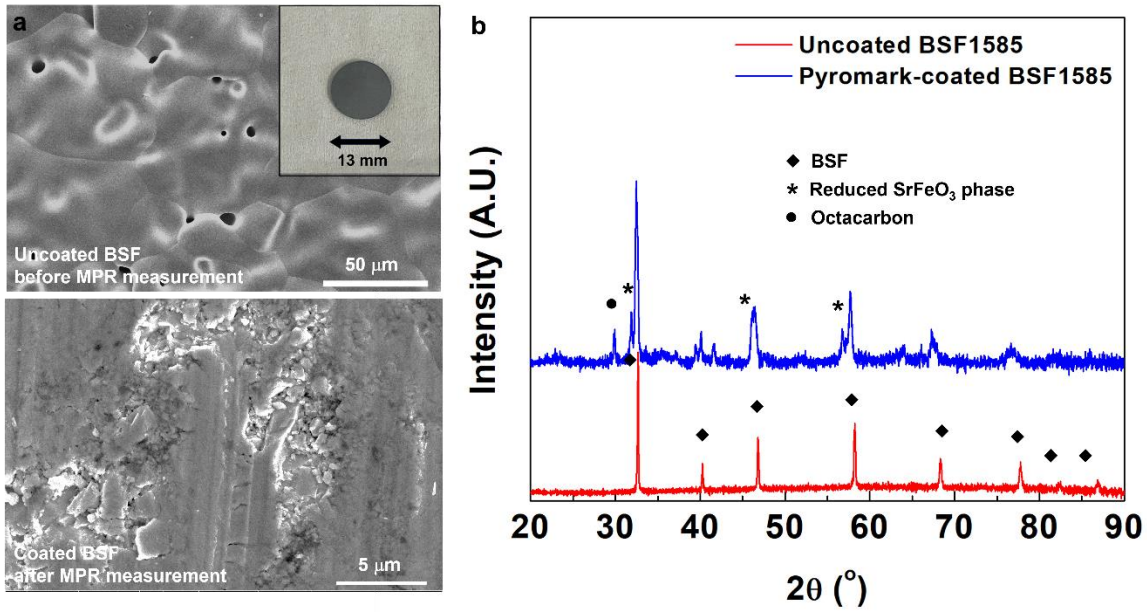

Figure 4.7 The surface morphology and crystal structure characterizations of BSF1585: **(a)** SEM images of uncoated BSF1585 before the measurement and Pyromark-coated BSF1585 after the measurements. The inset photo shows the uncoated BSF1585 pellet for the measurements; **(b)** XRD patterns of pure BSF1585 and Pyromark-coated BSF1585 followed by the same heating procedure in the MPR measurements, respectively.

Figure 4.7b shows the XRD patterns of the uncoated and Pyromark-coated BSF1585 samples, followed by the same heating procedure in the MPR measurements. The XRD pattern

of uncoated BSF1585 was cubic perovskite phase, indicating it was still pure and single phase. However, the coated BSF1585 sample after the high-temperature MPR measurement exhibited additional peaks from secondary phases that contributed to reduced $SrFeO_3$ phase and organic contaminants, Octacarbon. Briefly, Pyromark coating is a silicone-based high-temperature paint consisting of solar absorptive spinel oxides (e.g., $MnCr_2O_4$) and blend methyl phenyl polysiloxane resin binders in diluted organic solvents (*153, 161, 162*). The emergence of these secondary phases is likely due to the reaction between the Pyromark coating and BSF1585 perovskite, and/or the silicone-based residues of the Pyromark coating after high-temperature measurements.

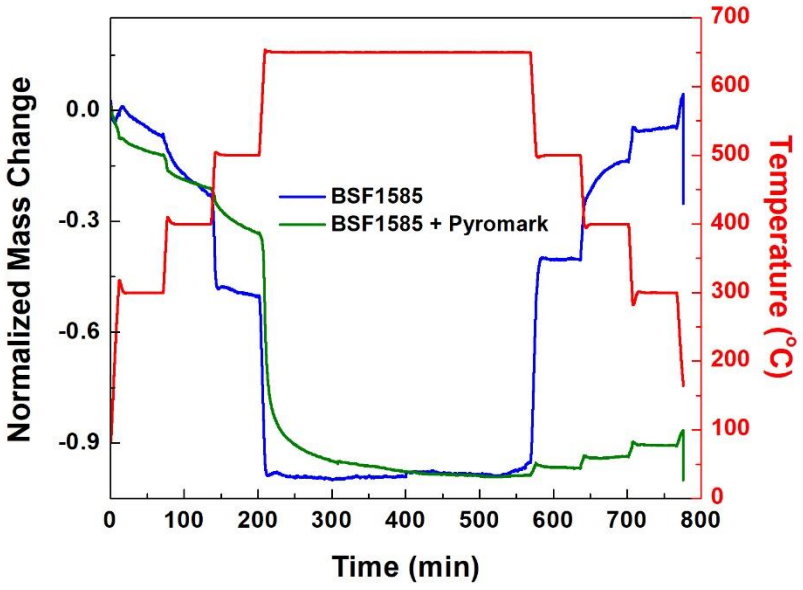

Figure 4.8 TGA results of BSF1585 samples with a heating and cooling rate of 20 K min^{-1} in 20% O_2/N_2 gas environment up to 650 °C. The normalized mass changes of BSF1585 with and without the presence of Pyromark are plotted as a function of time

To investigate the effect of the contamination from Pyromark coating on BSF1585, the sample was studied using TGA. The TGA results of single-phase BSF1585 with and without the Pyromark coating were shown in **Figure 4.8,** which compares the normalized mass change of the

samples at different heating and cooling stages. Here, normalized mass change is defined as $\frac{\Delta m}{\Delta m_{max}}$, where Δm_{max} is the maximum mass change recorded in the TGA measurement. Single-phase BSF1585 reached chemical equilibrium quickly at 650 °C and showed a stable mass at this temperature, similar to earlier work with the same material (*130, 152*). The single-phase BSF1585 also quickly regains mass upon cooling, revealing the progress of the reversible reaction. On the other hand, BSF1585 with the Pyromark coating shows a delay in reaching chemical equilibrium at 650 ˚C, requiring ~ 5 h. It is consistent with the time-dependent thermal conductivity results observed in the Pyromark-coated sample (**Figure 4.5c**), which showed that the decreasing thermal conductivity of Pyromark-coated BSF1585 also required ~ 5 h to plateau when held at 650 °C. Furthermore, the TGA data also reveals very different mass changes of the Pyromark-coated sample during the heating and cooling steps. Upon cooling from 650 °C, Pyromark-coated BSF1585 does not regain mass within the measurement time. It further illustrates that the presence of Pyromark coating hinders the reaction kinetics and reversibility of the reaction. It also explains the different thermal conductivity trends of pure BSF1585 and Pyromark-coated BSF1585 (**Figure 4.4b & 4.4c** *vs.* **Figure 4.5b & 4.5c)**.Through the control experiment of BSF1585 with and without contamination, we demonstrate that not only does the *in-situ* monitoring using MPR can establish $\lambda - \delta$ correlation to evaluate oxygen carrier capacities in real-time, but it is also capable of detecting any physical and/or chemical changes of TCMs based on thermal characterization results.

The experimental results of both $Ca(OH)_2$ and BSF1585 clearly show observable changes in thermal conductivity during thermochemical changes. It brings motivation to further develop the MPR technique as a potential high-throughput diagnostic tool for monitoring both the kinetics and thermal transport properties of TCMs. The precise thermal conductivity data of

TCMs are useful for thermal systems and reactor design optimization. Based on the established correlations between the thermal conductivity and the conversion fraction of the reactions, one can apply the MPR technique for monitoring the reaction based on a thermal characterization technique. The thermal transport property changes in TCMs (i.e., perovskite oxides) captured by the MPR thermal characterization method can shed new light on the kinetics study of reactions. It can be particularly useful for studying perovskite oxides where chemical changes are, otherwise, challenging to capture simply using conventional characterization techniques.

4.4. Conclusion

In this work, we reported the use of the MPR technique for *in-situ* monitoring of thermochemical reactions of two selected TCMs, calcium oxide ($Ca(OH)_2$) and $Ba_{0.15}Sr_{0.85}FeO_{3-\delta}$ (BSF1585) with different reaction temperatures. Their changes in thermal conductivity upon thermochemical reactions were captured in real time when the reactions were taking place. For $Ca(OH)_2$, the thermal conductivity change is consistent with the conversion fraction of $Ca(OH)_2$ to CaO in the dehydration process at 380 ^oC. For BSF1585, specimens with and without Pyromark coating were studied. In both cases, the thermal conductivity decreases upon heating. The decrease is correlated to the change in oxygen nonstoichiometry that is associated with oxygen vacancy creation. Reversibly, upon cooling, the BSF1585 regained their thermal conductivity to slightly lower values due to re-oxidation. In uncoated BSF1585, the measured thermal conductivity using MPR reveals the rapid kinetics of the thermochemical reactions. It is also consistent with our kinetic study of uncoated BSF1585 using TGA and earlier thermochemical reaction studies. On the other hand, the Pyromark-coated BSF1585 displayed a sluggish decrease and time-dependent trend in thermal conductivity. It is associated with hindered reaction kinetics due to the emergence of secondary phases resulting from the

interaction between Pyromark coating and BSF1585. Based on the study of two selected TCMs, we demonstrate the capability of performing *in-situ* monitoring using MPR to reveal thermochemical reaction kinetics. On an instrumentation level, the technique can potentially be leveraged for high-throughput diagnostic applications at lab- and/or large-scale thermochemical reactors and systems.

Acknowledgements

Chapter 4 is currently being prepared for submission as **K. M. Chung**, N. P. Nguyen, S. R. Adapa, P. G. Loutzenhiser, R. Chen "*In-situ Thermal Conductivity Measurement Revealing Kinetics of Thermochemical Reactions*". *in Prep*. For this work, K. M. Chung performed experiments, data analysis and manuscript writing.

Chapter 5. Black coating of quartz sand towards low-cost solar-absorbing and thermal energy storage material for concentrating solar power

5.1. Introduction

As renewables such as photovoltaic and wind energy are gaining increasing penetration in the electrical grid, their intermittency and the associated stability issue are becoming a grand challenge. Concentrating solar power (CSP) coupled with thermal energy storage (TES) is being considered as an appealing solution to deliver stable, dispatchable, and inexpensive electricity generation from renewable solar energy (*49, 163-165*). CSP technology utilizes the thermal energy collected from concentrated sunlight for generating electricity. The heat can be stored in a TES system, which is significantly less expensive and more scalable than electrochemical storage of electricity, enabling electricity generation for up to 8-10 hours when the sunlight is unavailable (*111, 166, 167*). The next-generation CSP plants aim to increase the overall efficiency by elevating the operating temperatures to above 700 ^{o}C (*4, 49, 50*). There are three main pathways under consideration to capture and store high-temperature thermal energy from concentrated sunlight, gas (supercritical CO_2), liquid (e.g., molten salts), and solids. Among these, solid particles are considered a promising heat transfer medium (HTM) and TES material because they can reliably operate at elevated temperatures with minimal stability and safety concerns (*7, 164, 165, 168*), e.g., no corrosion issue as in molten salt or high pressure as in supercritical CO_2. As such, the solid particle pathway is being explored as the focus of the Generation-3 (Gen3) CSP technology where the target operating temperature is close to 800 ^{o}C (*169, 170*).

The selection of solid particles for CSP systems is based on various factors, including optical properties, thermophysical properties, stability (chemical, mechanical, and thermal), and production cost (*164*). Ideal particles would possess high solar absorptance, high thermal conductivity and specific heat, good mechanical and thermal stability, and low cost. Various solid particles, for example, alumina (*50, 51, 171-173*), black silicon carbide (SiC) (*165, 173-176*), quartz sand (*172, 173, 176, 177*) and ceramic particles (*165, 173, 176, 178-181*) have been evaluated as HTM and TES materials for CSP plants. Yet, to date, there is no solid particle that would simultaneously satisfy all the performance and cost metrics. Alumina particles possess desirable stability as an HTM in the falling particle CSP systems. However, they have low solar absorptance (white color) and are more expensive than other types of particles. Black SiC possesses excellent thermal conductivity, high solar absorptance, and good mechanical strength. However, its production cost is high (*50*) and can be oxidized at high temperatures in the air. Silica sand is abundant, inexpensive ($30-50/ton) and has promising thermophysical properties such as thermal stability and reasonably good thermal conductivity (*172, 173, 176, 177, 182*). The main drawback of quartz sand is its low solar absorptivity, about 0.4 (*7, 176, 178, 183*). Currently, ceramic particles such as Carbo HSP, manufactured by CARBO Ceramics Inc. and primarily used as proppants in the petroleum industry, are promising HTM and TES materials under consideration for particle-based Gen-3 CSP. The main constituents of the Carbo particles are sintered bauxite consisting of Al_2O_3 and SiO_2, with a small amount (a few percent) of Fe_2O_3 and TiO_2 which gives the dark appearance (*184, 185*). They are mechanically durable and have good solar absorptance (ranging from 0.89 to 0.93) (*179, 181, 186, 187*). However, their relatively high production cost is still one of the roadblocks to further lowering the levelized cost of electricity (LCOE) of CSP systems (*180*). The cost of the CARBO particles is about

$1,000/ton (*185*). At this cost and with its solar absorptance of ~0.90, technoeconomic analysis done by Albrecht *et al.* (*188*) shows that the LCOE of the CSP with TES will be around 0.058 $/kWhr. If the cost of the particles is reduced to below $100/ton, the LCOE can be as low as 0.053 $/kWhr, which will bring it closer to the DOE's 2030 solar cost target of 0.050 $/kWhr (*189*). In addition, it has been shown that Carbo particles can degrade and become less black above 700 ^{o}C in the air due to oxidation, thus lowering their solar absorptance (*184, 185*). In light of this, it would be useful to develop a new type of solid particles that can meet all the requirements for future CSP & TES systems, including excellent solar absorptance, suitable thermophysical properties, good mechanical and thermal stability, and being cost effective.

It has been suggested that black coating can be a promising approach to increase the solar absorptance of low-cost silica sand as well as improve the absorptance and stability of Carbo bauxite proppants. Gimeno-Furio *et al.* (*187*) used carbon black and thermally degraded glucose to coat silica sand to improve its solar absorptance from around 40% to 75-80%. However, the coating materials are not chemically stable at high temperatures. The maximum operating temperature of carbon back coated silica is limited to 645 ^{o}C while that for glucose-coated silica is only up to 441 ^{o}C. Recently, Gobereit *et al*. (*190*) modified the solar absorptivity of bauxite-derived proppants using various methods, including dip-coating of iron-manganese-oxide and high-temperature diffusion of transition metal ion from surface black paint coating into the bulk of bauxite proppants. However, it was found that the surface coating attained by dip-coating was not resistant to abrasion, presumably because the adhesion between the black coating and bauxite particles was weak. The coloring ions diffusion method could lead to stable and black bauxite proppants but the method was considered complicated and expensive (*190*), e.g., involving high-temperature (1200-1350 ^{o}C) annealing process for the ion diffusion. Alkan et al. (*191*) developed

a coating process by high-energy, high-speed dry mixing of bauxite proppants with fine black pigment followed by high-temperature annealing (1200 ^{o}C). The coating increased the solar-weighted absorptance of bauxite particles from 0.89 to 0.93 and was shown to be stable against thermal annealing and mechanical abrasion. The is a promising process to improve the performance and stability of bauxite particles, but the mixing and annealing processes are energy-intensive and could lead to high costs.

In this work, we aim to develop an inexpensive, facile, and scalable black coating on solid particles, including low-cost quartz sand, with high solar absorptance and thermal stability. We develop a coating solution containing black spinel oxide nanoparticles dispersed in a silicone-based resin. Upon curing at only ~ 50 ^{o}C, the resin turns into silica, providing good adhesion between the black oxide nanoparticles and the silica sand particles. This process is energy-efficient as it does not involve high-temperature thermal treatment process and is generally applicable to all types of solid particles. In the work, we demonstrate the process on quartz sand, effectively making these abundant and inexpensive solid particles suitable for direct solar absorption applications in CSP & TES. The black nanoparticles used for coating in this work are based on $Cu_{0.5}Cr_{1.1}Mn_{1.4}O_4$ and $CuCr_2O_4$ spinel oxides, made from two representative processes (solid-state reaction and hydrothermal, respectively) and with two average nanoparticle sizes (~ 500 nm vs. ~ 35 nm, respectively). The idea is also compatible with any black oxide nanoparticles, especially spinel oxides, many of which have been shown to possess high solar absorptance and excellent thermal stability at high temperatures in the air (e.g., 2000 hours at 800 ^{o}C (*192*)). We found that a thin layer of black coating significantly increases the solar absorptance of the quartz sands, from ~0.40 to ~0.90. Importantly, the morphologies and solar absorptance of the black-coated quartz sands remained unchanged after 100-hr isothermal

annealing at 800 ^{o}C in air. The preliminary abrasion resistance test shows that the coating on the quartz sand still maintains excellent uniformity after 24-hr ball mixing with Yttria Stabilized Zirconia (YSZ) grinding balls and the optical properties remained the same. We also measured the effective thermal conductivity (k_{eff}) of the particle beds of black-coated quartz sand. We found that k_{eff} of the coated quartz sand is comparable to that of uncoated sand as well as Carbo ceramic proppant particles of similar size. This work suggests that our coating process is an effective approach to increasing the solar absorptance of solid particles. In particular, the spinel oxide-coated quartz sands can serve as an excellent low-cost alternative, with comparable optical and thermal properties and better thermal stability, to the state-of-the-art Carbo ceramic proppants, as a solar absorbing heat transfer and TES medium for future CSP systems.

5.2. Materials and methods

5.2.1. Sample preparation

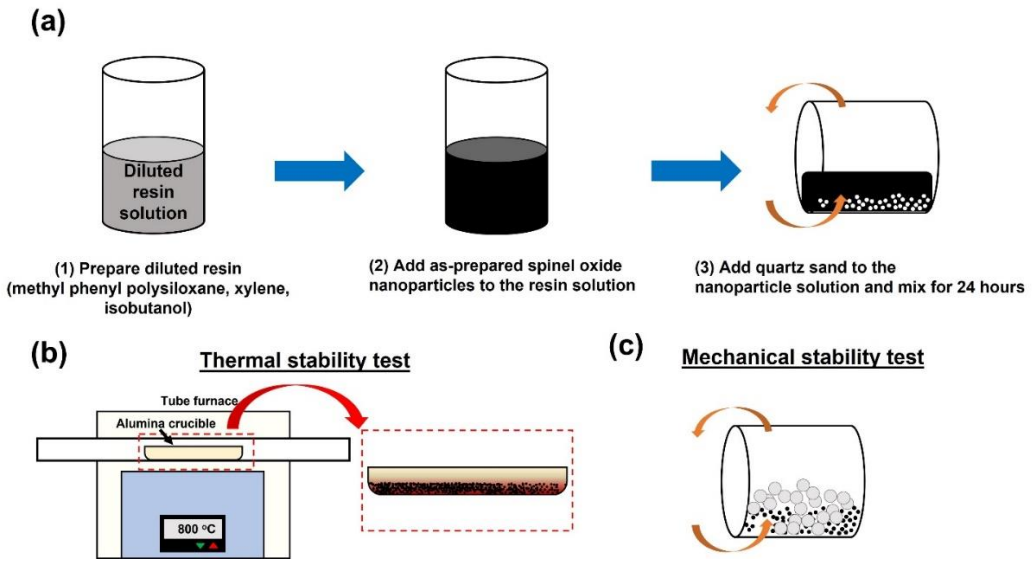

Figure 5.1 Schematic showing **(a)** the workflow of the coating process of quartz sand; **(b)** the thermal stability test of coated quartz sand; and **(c)** the ball mixing mechanical stability test with YSZ grinding balls

The quartz sands are *Northern White* silica sand 430 from Covia Corporation (sourced in St. Peter's Sandstone in Illinois). The median diameter of the sand is 407 μm. The main composition is SiO2 (> 99 %), with a trace amount of oxides of Al, Fe, Ti, Ca, etc (*182*). The spinel oxide nanoparticles for coating are $Cu_{0.5}Cr_{1.1}Mn_{1.4}O_4$ and $CuCr_2O_4$. The former is made from a traditional solid-state reaction method by mixing and sintering binary oxides followed by ball milling. These nanoparticles, with an average diameter of ~500 nm, are commercially available in large quantities (Foshan Huayi Ceramic Colours Co., LTD, Foshan, China). $CuCr_2O_4$ nanoparticles with an average diameter of 35 nm were synthesized using a hydrothermal process. The details of the hydrothermal process and the characterization of both types of nanoparticles were reported in our earlier work (*161*). To prepare the nanoparticle solution for coating, the nanoparticles were mixed with a 1:4 wt. ratio (nanoparticle: resin) in a solution containing a resin made of methyl phenyl polysiloxane (SILIKOPHEN P80/X, Evonik) diluted with iso-butanol and xylene. The quartz sand was then added to the nanoparticle solution with a 1:1 volume ratio. The resultant mixture was then mixed for 24 hours. **Figure 5.1a** shows the schematic of the coating process. The mixing process allowed the nanoparticles to uniformly distribute on the surfaces of the sand particles. After mixing, the coated quartz sand was extracted from the solution for drying in an oven at around 50 ^oC for 24 hr. To test the thermal stability of the coated quartz sand, the coated quartz sand was isothermally annealed at 800 ^oC for 100 hours in the air (**Figure 5.1b**). To further test the abrasion resistance of the coated quartz sand after the thermal treatment, the annealed coated sand was mixed with YSZ grinding balls of 3 mm in diameter (Inframat® Advanced Materials^{TM}) with a 1:3 wt. ratio, then undergoing an intensive ball mixing process for 24 hours in a ball milling machine (SHIMPO PTA-02, Nidec Corporation) with a

maximum shaft rotational speed of 247 rpm, in which the particles were expected to be constantly colliding with other particles and the YSZ balls (**Figure 5.1c**).

5.2.2. Material characterization and measurements

5.2.2.1. Scanning electron microscopy (SEM) and X-ray diffraction (XRD)

Scanning Electron Microscopy (SEM) equipped with Energy Dispersive X-Ray Spectroscopy (EDS) (FEI Quanta 250 scanning electron microscope) was used to image the surface morphology of the pristine and coated sand particles as well as the compositional homogeneity of the spinel oxide coating. The X-ray diffraction (XRD) pattern of each sample was characterized by Rigaku Smartlab X-ray diffractometer with Cu Kα (λ = 0.15418 nm) as the radiation source.

5.2.2.2. Differential scanning calorimetry

To confirm the thermal stability and thermal responses of the quartz sand samples, a differential scanning calorimeter (DSC) (404 F3 Pegasus®, NETZSCH) was used to measure the pristine and coated quartz sand samples. Each quartz sand sample was put into the alumina crucible and was heated from room temperature to 800 ^{o}C, with a heating rate of 10 K min^{-1}. During the measurements, nitrogen gas (N_2) was used as the protective gas. The DSC signals were recorded and then analyzed by using Proteus®, an analysis program provided by Netzsch.

5.2.2.3.UV-Vis-NIR spectrometry

The diffuse reflectance measurement of the quartz sands was performed using a UV-VIS-NIR spectrometer (PerkinElmer Lambda-1050 UV/Vis/NIR spectrophotometer) equipped with a 150 mm InGaAs integrating sphere in the wavelength range from 280 to 2500 nm. During the measurements, the quartz sand samples were confined in a quartz cuvette. The solar absorptance

α_s of the samples is defined as the spectral solar absorptivity weighted by the solar spectrum (ASTM G173), divided by the solar insolation,

$$\alpha_s = \frac{\int_0^\infty \alpha(\lambda) I_s(\lambda) d\lambda}{\int_0^\infty I_s(\lambda) d\lambda} \quad (5.1)$$

where $\alpha(\lambda)$ is the spectral solar absorptivity of the sample and $I_s(\lambda)$ is the spectral intensities of solar insolation. The spectral intensities of solar insolation for the weighted spectral solar absorptivity is based on ASTM G173 (*193*).

5.2.2.4. Effective thermal conductivity measurement

The effective thermal conductivity (k_{eff}) of the quartz sands was determined using a custom-made transient hot-wire (THW) apparatus. The quartz sand particles were filled into a mica THW holder ($11.6 \times 1.5 \times 0.97$ cm^3). The THW test section was placed in a tube furnace (GSL-1100X, MTI Corporation) equipped with N_2 gas supply and a pressure control system. The quartz sand samples were measured from room temperature to temperature (T) around 700 ^{o}C under N_2 gas environment at 760 Torr. In the THW measurements, k_{eff} of the samples was obtained from the transient temperature rise after applying a constant heat flux at time $t = 0$ with the assumption of a line heat source within an infinite medium:

$$k_{eff} = \frac{q'/4\pi}{d(\Delta T)/d(\ln t)} \quad (5.2)$$

where ΔT is the temperature rise of the Pt wire induced by the application of an electrical current I to it for a duration of time (t), q' is the heat rate per unit length of the Pt wire: $q' = I^2R/L$, where L is the length of the Pt wire, and R is the resistance of the Pt wire at the measurement temperature T. More details of the THW apparatus and the data analysis can be found in our previous work (*181, 194*).

5.3. Results and Discussion

5.3.1. Phase stability and surface morphology

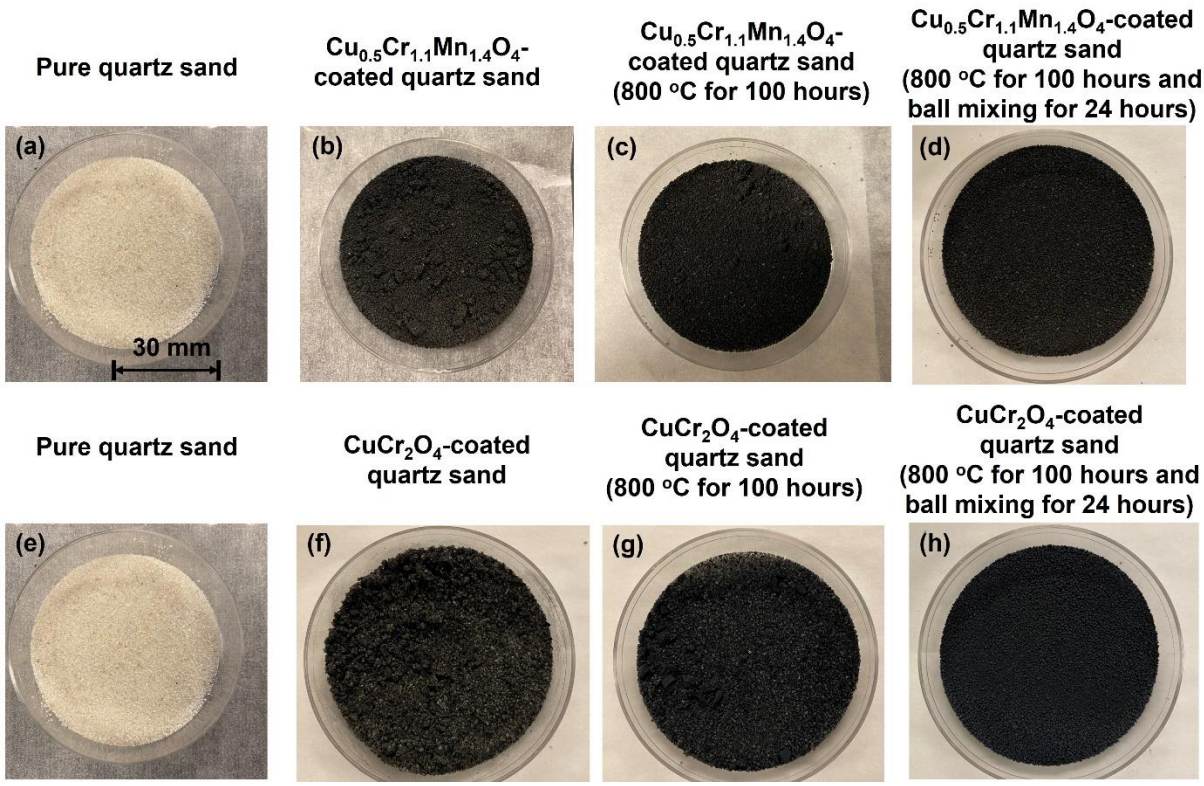

Figure 5.2 Photographs of **(a-d)** $Cu_{0.5}Cr_{1.1}Mn_{1.4}O_4$-coated quartz sand; and **(e-h)** $CuCr_2O_4$-coated quartz sand before coating, after coating, after isothermal annealing, and after isothermal annealing & ball mixing with YSZ grinding balls.

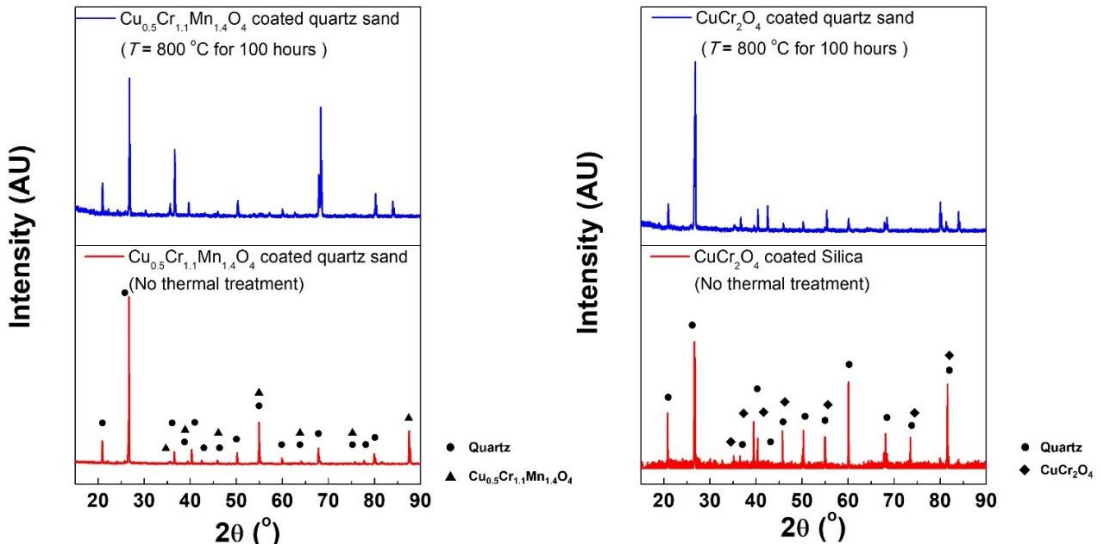

Figure 5.3 XRD patterns of **(a)** $Cu_{0.5}Cr_{1.1}Mn_{1.4}O_4$-coated quartz sand; and **(b)** $CuCr_2O_4$-coated quartz sand

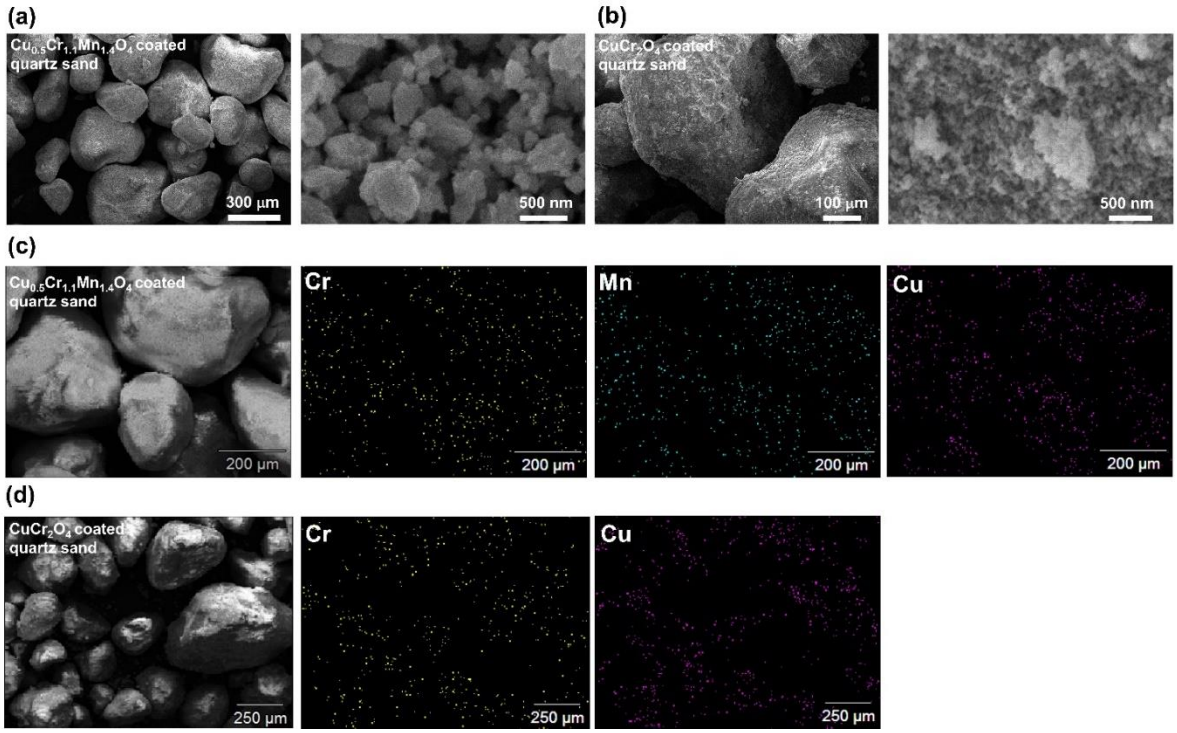

Figure 5.4 SEM images of **(a)** $Cu_{0.5}Cr_{1.1}Mn_{1.4}O_4$-coated quartz sand; and **(b)** $CuCr_2O_4$-coated quartz sand; EDS mapping results of **(c)** $Cu_{0.5}Cr_{1.1}Mn_{1.4}O_4$-coated quartz sand and **(d)** $CuCr_2O_4$-coated quartz sand

Figure 5.2 shows the photographs of quartz sand before coating, after coating, after thermal annealing, and after thermal annealing plus ball mixing with YSZ grinding balls. The uncoated quartz sand has a general white appearance. After coating with $Cu_{0.5}Cr_{1.1}Mn_{1.4}O_4$ or $CuCr_2O_4$ spinel oxide nanoparticles, the quartz sand turned black. The coated quartz sand still maintained its black color after 100-hr 800 ^oC thermal annealing in air and subsequent ball mixing with YSZ grinding balls for 24 hours. **Figures 5.3a** and **5.3b** show the XRD patterns of the quartz sand coated by $Cu_{0.5}Cr_{1.1}Mn_{1.4}O_4$ and $CuCr_2O_4$ respectively. The peaks of the XRD patterns are contributed by quartz sand and the spinel oxides, as labeled in **Figure 5.3**. The phases of the coated quartz sand remain unchanged after 800 ^oC isothermal annealing for 100 hours. It indicates the phase stability of the quartz sand as well as the spinel oxide coating. It is

also consistent with our previous results about the stability of the spinel oxide coating after 2000-hr annealing at 800 ^{o}C in the air (*161*). **Figures 5.4a** and **5.4b** show the SEM images of $Cu_{0.5}Cr_{1.1}Mn_{1.4}O_4$-coated quartz sand and $CuCr_2O_4$-coated quartz sand respectively. From the SEM images of each coated quartz sand, both $Cu_{0.5}Cr_{1.1}Mn_{1.4}O_4$ and $CuCr_2O_4$ nanoparticles were well-adhered to the surface of the quartz sand particles. As mentioned earlier, the adhesion was provided by the silicone resin that turned into silica upon curing. From the SEM images that display the local surface areas of the quartz sand, the nanoparticles of $Cu_{0.5}Cr_{1.1}Mn_{1.4}O_4$ and $CuCr_2O_4$ distributed uniformly on the particle surface. This can also be demonstrated from the EDS mapping results shown in **Figures 5.4c** and 5.**4d**. The individual elements of the spinel oxide nanoparticles were homogeneously distributed on the quartz sand surface. The surface morphology and the nanoparticle coatings of coated quartz sand after thermal treatment and ball mixing were also examined. They were included in **Figures 5.5** and **5.6**). According to the SEM and EDS analysis, $Cu_{0.5}Cr_{1.1}Mn_{1.4}O_4$ and $CuCr_2O_4$ show little changes in particle sizes after 800 ^{o}C isothermal annealing for 100 hours. This again is consistent with our previous observations regarding the thermal stability of these spinel oxide nanoparticles (Rubin *et al.* (*161*)). Like the surface morphology of the coated quartz sand before any thermal treatments, the nanoparticles were well-adhered to and uniformly distributed on the quartz sand particle surfaces. The experimental results support the idea that $Cu_{0.5}Cr_{1.1}Mn_{1.4}O_4$ and $CuCr_2O_4$ spinel oxide are thermally stable coating materials for sand particles at high temperatures. In addition, after the YSZ ball mixing test for 24 hours, the nanoparticle coatings remained largely the same, with only small amounts of nanoparticles transferred to the surface of the YSZ grinding balls. It demonstrates that the coated quartz sand can potentially withstand a certain extent of mechanical abrasion and attrition with other particles or particle containment surfaces in actual operational

conditions. Nevertheless, a more thorough and longer-term evaluation regarding the mechanical stability of the particles is needed in the future.

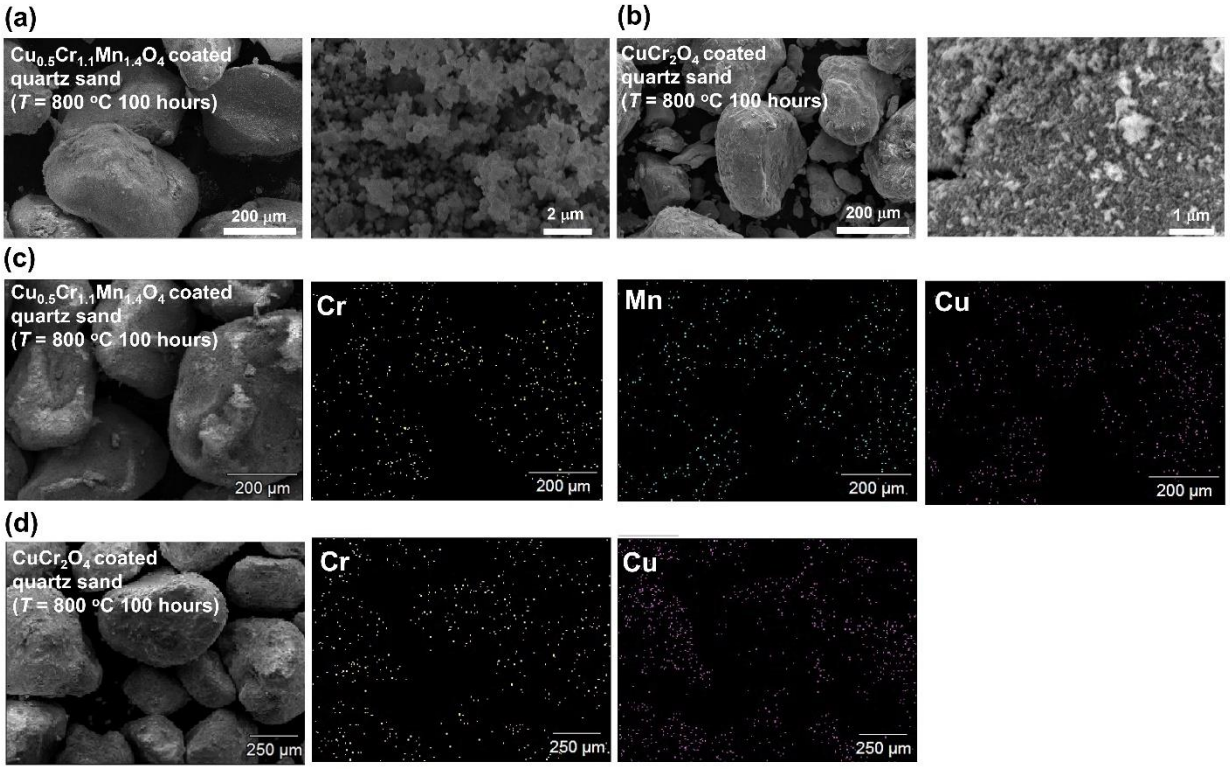

Figure 5.5 SEM images of coated sand samples after 800 °C thermal annealing for 100 hours in the air. **(a)** $Cu_{0.5}Cr_{1.1}Mn_{1.4}O_4$-coated quartz sand; and **(b)** $CuCr_2O_4$-coated quartz sand; EDS mapping results of **(c)** $Cu_{0.5}Cr_{1.1}Mn_{1.4}O_4$-coated quartz sand and **(d)** $CuCr_2O_4$-coated quartz sand.

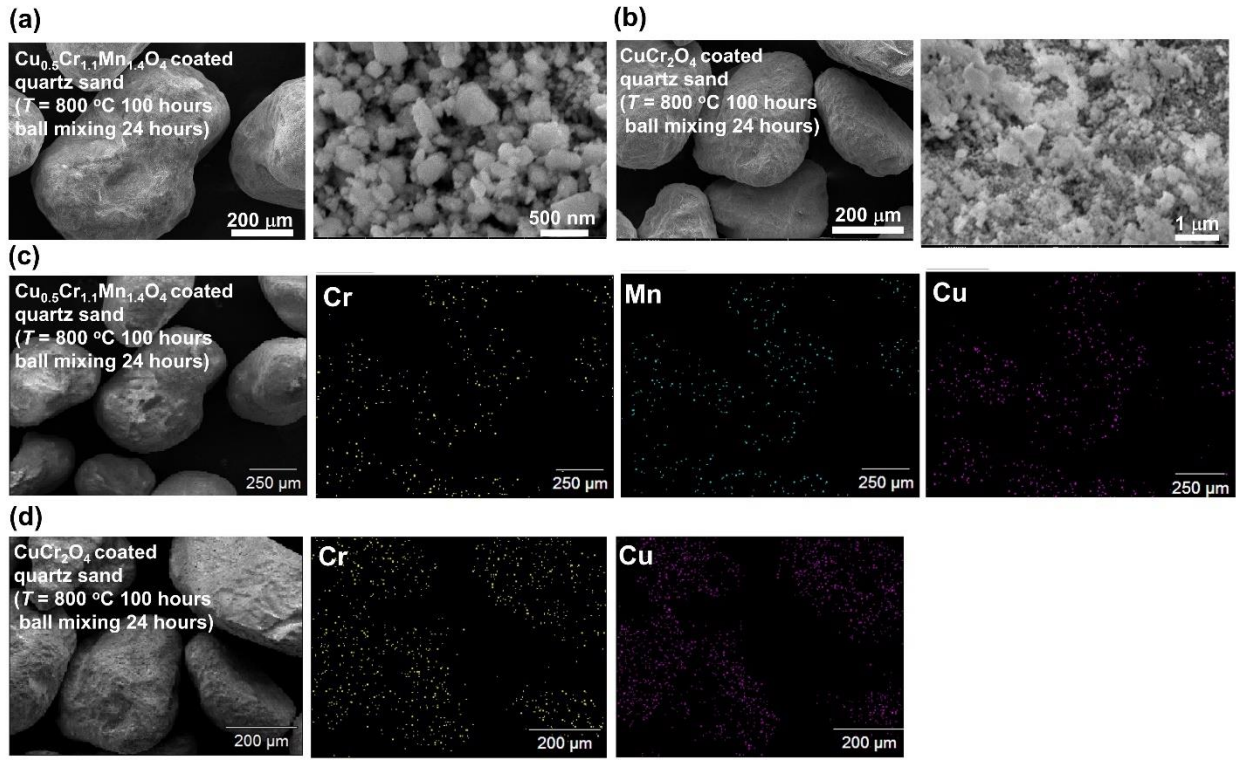

Figure 5.6 SEM images of coated sand samples after 800 °C thermal annealing for 100 hours in the air followed by ball milling for 24 hours. **(a)** $Cu_{0.5}Cr_{1.1}Mn_{1.4}O_4$-coated quartz sand; and **(b)** $CuCr_2O_4$-coated quartz sand; EDS mapping results of **(c)** $Cu_{0.5}Cr_{1.1}Mn_{1.4}O_4$-coated quartz sand and **(d)** $CuCr_2O_4$-coated quartz sand.

5.3.2. Thermal stability

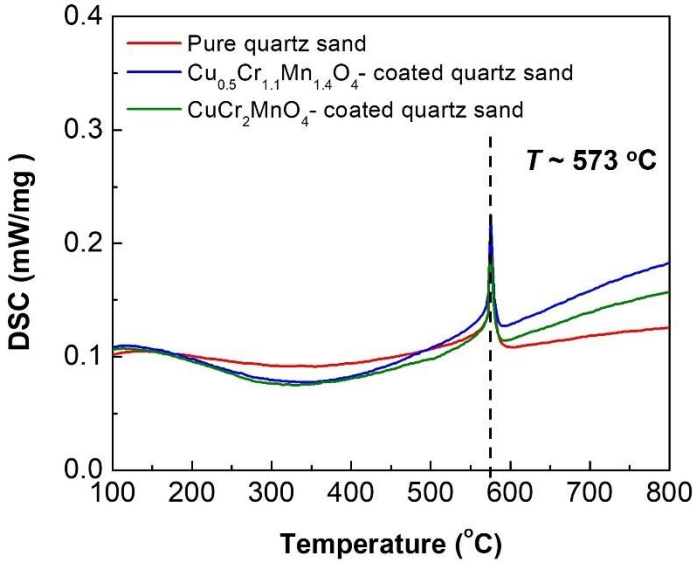

Figure 5.7 DSC curves of uncoated quartz sand and quartz sand coated with $Cu_{0.5}Cr_{1.1}Mn_{1.4}O_4$ and $CuCr_2O_4$

Figure 5.7 shows the DSC curves of quartz sand with and without the spinel oxide coatings. The quartz sand samples were heated from room temperature to 800 °C with a heating rate of 10 K min^{-1}. As shown in the figure, the DSC curves of each sample are similar. The only endothermic peak that emerges from each sample is at 573 °C, which corresponds to the phase transition of quartz from α- quartz to β- quartz (*195*). This phase transition of quartz is reversible in that upon cooling, the quartz sand sample transforms back to α- quartz. Other than the endothermic caused by the reversible phase transformation of quartz, there was no additional peak. It demonstrates that the spinel oxide coatings, $Cu_{0.5}Cr_{1.1}Mn_{1.4}O_4$ and $CuCr_2O_4$, are thermally stable in the temperature range we investigated (room temperature to 800 °C).

5.3.3. Enhancement of solar absorptance

Figure 5.8a shows the spectral absorptance of uncoated quartz sand, quartz sand coated with $Cu_{0.5}Cr_{1.1}Mn_{1.4}O_4$ or $CuCr_2O_4$ in the wavelength range from 280 to 2500 nm. The spectral absorptance of the uncoated quartz sand is around 40% in most of the wavelength range from 280 to 2500 nm. After coating with $Cu_{0.5}Cr_{1.1}Mn_{1.4}O_4$ or $CuCr_2O_4$, the spectral absorptance significantly increases. The absorptance of the coated quartz sand is mostly higher than 85% in the entire spectral range and is around 90% in the UV-Vis spectra (up to 750 nm). It indicates that spinel oxide coatings can significantly enhance the solar absorptance of solid particles. In general, the spectral absorptance curves of the coated quartz sand show little changes in the entire spectral range after the isothermal annealing and ball mixing tests. It is consistent with our microstructural observations in **Figure 5.2** as well as our SEM analysis of the coated quartz sand, which shows that the coatings are thermally and mechanically stable.

The solar-weighted absorptance (α_s) of pristine and coated quartz sand (before annealing, after 800 ^oC isothermal annealing, and after ball milling) was shown in **Figure 5.6b**. Before coating, the pristine sand has α_s of 0.426, similar to the results of Díaz-Heras *et al.*(*176*) and Palacios *et al.* (*183*). The solar-weighted absorptance of the $Cu_{0.5}Cr_{1.1}Mn_{1.4}O_4$ and $CuCr_2O_4$-coated quartz sand was increased to 0.893 and 0.888, respectively. After 100 hours of isothermal annealing at 800 ^oC, the solar-weighted absorptance of the coated sands remained nearly the same (0.890 and 0.881 for the $Cu_{0.5}Cr_{1.1}Mn_{1.4}O_4$- and $CuCr_2O_4$- coated sands respectively) after 100 hr isothermal annealing at 800 ^oC in air. More importantly, after the thermal annealing and ball milling, the solar-weighted absorptance also remained virtually the same (0.893 and 0.885 for the $Cu_{0.5}Cr_{1.1}Mn_{1.4}O_4$ and $CuCr_2O_4$- coated sands respectively). The experimental results

exhibit the excellent and stable solar absorptance of the coated sand particles after long-term thermal annealing and mechanical abrasion (tested with ball milling).

5.3.4. Effective thermal conductivity

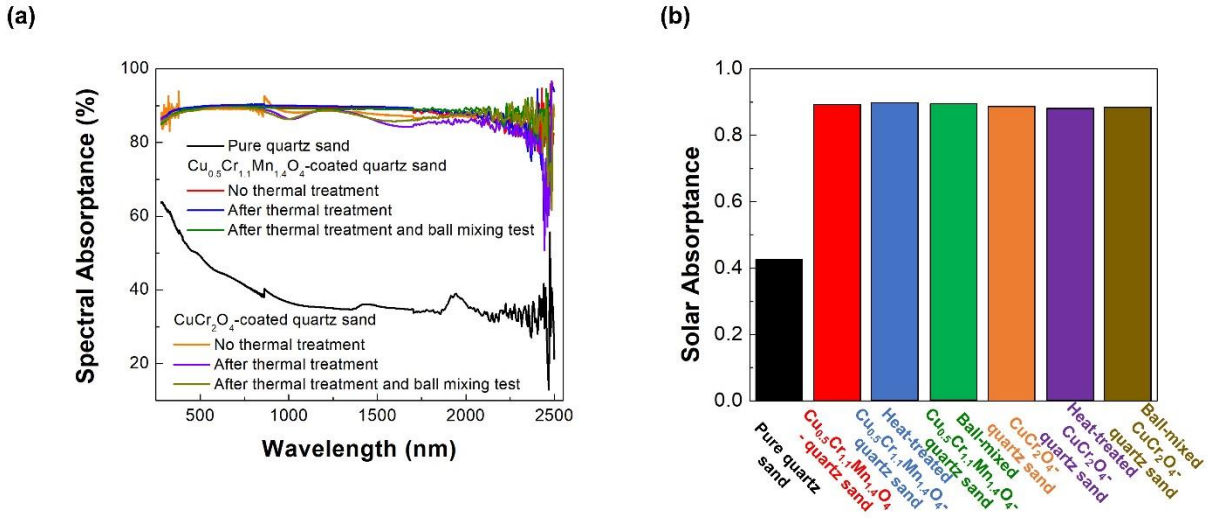

Figure 5.8 (a) Spectral absorptance (%) of uncoated quartz sand, quartz sand coated with $Cu_{0.5}Cr_{1.1}Mn_{1.4}O_4$ and $CuCr_2O_4$ in the wavelength from 280 to 2500 nm; and **(b)** the solar weighted absorptance of the quartz sand samples before and after isothermal annealing at 800 ^oC for 100 hours and ball mixing test with YSZ balls for 24 hours

We also aim to evaluate if the nanoparticle coating could impact, especially adversely, the thermal transport behavior of the particle beds. The effective thermal conductivity of each quartz sand sample was measured using the THW apparatus under N_2 gas environment at 760 Torr**. Figure 5.9** shows the effective thermal conductivity of uncoated, $Cu_{0.5}Cr_{1.1}Mn_{1.4}O_4$-coated, and $CuCr_2O_4$-coated sand beds as a function of temperature up to ~ 700 ^oC. k_{eff} of pristine quartz sand increases with temperature from 0.31 W m^{-1} K^{-1} at room temperature to 0.56 W m^{-1} K^{-1} at ~ 700 ^oC. The increase in k_{eff} with temperature originates from increasing gaseous thermal conductivity of air and radiative contribution, similarly observed in Carbo particles of HSP 40/70 and CP 40/100 we measured earlier (*181*). The coated quartz sand shows similar or

slightly lower k_{eff} at low-and-intermediate temperatures ($T \leq 400$ °C) but slightly higher k_{eff} at high temperatures ($T > 400$ °C). From 25 to 400 °C, $Cu_{0.5}Cr_{1.1}Mn_{1.4}O_4$-coated quartz sand has very similar k_{eff} to the pristine sand whereas the $CuCr_2O_4$-coated one has about ~10% lower k_{eff}. Above 400 °C, both coated sand samples have higher k_{eff} than that of the uncoated sand. At 700 °C, k_{eff} of the $Cu_{0.5}Cr_{1.1}Mn_{1.4}O_4$-coated and $CuCr_2O_4$-coated samples is about 0.65 and 0.61 W m^{-1} K^{-1} respectively, or about 16% and 10% higher than that of the uncoated sand. The measured k_{eff} values of both the coated sand samples are comparable to that of ceramic solid particles of similar sizes at low temperature but higher at high temperatures, such as Carbo HSP 40/70 (average diameter ≅ 404 μm, k_{eff} = 0.24 W m^{-1} K^{-1} at 25 °C and 0.51 W m^{-1} K^{-1} at 700 °C) and Carbo CP 40/100 (average diameter ≅ 275 μm, k_{eff} = 0.26 W m^{-1} K^{-1} at 25 °C and 0.47 W m^{-1} K^{-1} at 700 °C) (*181*). This result reveals that a thin black coating on the quartz does not significantly affect k_{eff} of the particle bed, and at high temperature, might moderately increase its k_{eff}.

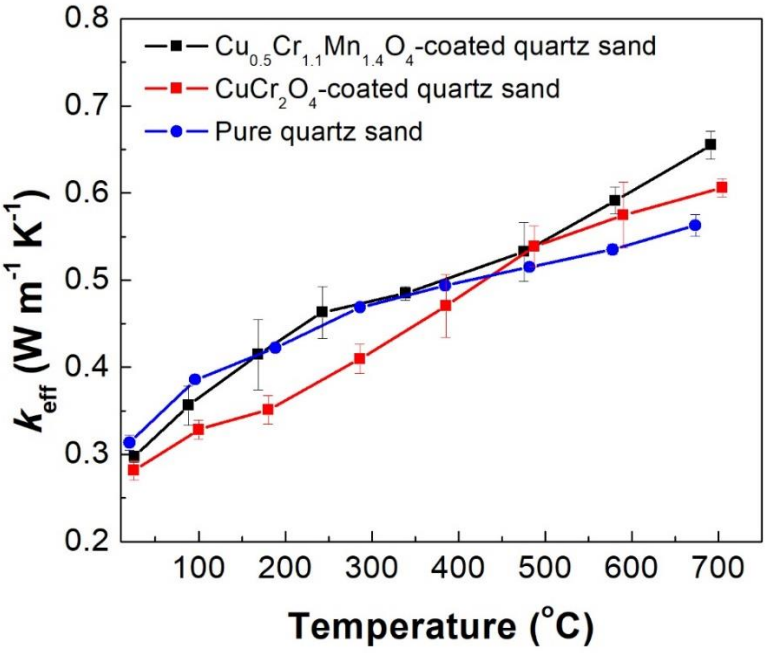

Figure 5.9 Effective thermal conductivity of uncoated quartz sand, $Cu_{0.5}Cr_{1.1}Mn_{1.4}O_4$-coated quartz sand and $CuCr_2O_4$-coated quartz sand as a function of temperature

The comparable or slight decrease in k_{eff} at low-and-intermediate temperatures and increased k_{eff} at high temperatures can be understood from the respective roles of different heat transfer pathways in particle beds, as we have studied in Carbo particles (*181*). At low temperature, k_{eff} is mainly contributed by gaseous conductions and to a much smaller extent by solid-solid contacts between particles. Both pathways depend on the exact contact geometries between the particles (e.g., contact area, and the thickness of the air layer near the contact points). The nanoparticle coatings on the large sand particles could have slightly changed the contact geometry, especially the ones with the small-diameter nanoparticles (~35 nm $CuCr_2O_4$ nanoparticles) which effectively increases the surface roughness of the sand particles thus reducing the solid-solid contact areas. On the other hand, at high temperatures, the radiative contribution to k_{eff} becomes more pronounced. From our solar absorptance measurements, the

solar absorptance of both coated sand samples (α_s = 0.89) is about twice of the pristine sand (α_s = 0.43). While we have not measured the thermal emissivity of the coated sand at 700 ^{o}C, it is reasonable to assume that it is quite high, probably around 0.9 based on our earlier measurement of planar coating of black spinel oxide (*161*). This is much higher than that of silica (~ 0.40 at 700 ^{o}C (*196, 197*)) because SiO_2 is transparent to photons of thermal wavelengths at 700 ^{o}C (2-5 μm). The higher emissivity can lead to higher radiative thermal conductivity in coated quartz sand and thus a higher overall k_{eff} (*198, 199*). It is worth investigating the modification and possibly enhancement of the optical and thermal transport properties of particle beds by utilizing coatings (*200*).

5.4. Conclusion

In conclusion, we report a convenient and cost-effective method to enhance the solar absorptance of low-cost quartz sand by coating it with black spinel oxide nanoparticles. The method is facile, energy-efficient, and cost-effective. It only involves gentle mixing and ~50 ^{o}C curing, without high-temperature thermal treatment or complicated chemical processing, making it a desirable method to enhance the solar absorptance of solid particles, especially low-cost silica sand. The solar absorptance of the coated quartz sand is improved to around 0.89, which is more than double of the original sand and comparable to that of Carbo proppants. The quartz sand coated with $Cu_{0.5}Cr_{1.1}Mn_{1.4}O_4$ and $CuCr_2O_4$ nanoparticles shows excellent thermal and mechanical stability. The coating is shown to be chemically stable and the solar absorptance remains high after 100-hr annealing at 800 ^{o}C in the air as well as abrasion test via 24-hr ball mixing with YSZ grinding balls. The effective thermal conductivity of the coated quartz sand is comparable to that of uncoated sands and Carbo ceramic proppant particles with similar from 25 to 400 ^{o}C. At higher temperatures (400-700 ^{o}C), the black-coated particles show moderately

higher thermal conductivity due to the higher thermal emissivity. Overall, the coated quartz sands shown here have similar or better optical and thermal properties and good stability compared to the Carbo ceramic particles, but with about one order of magnitude lower cost (30-50$/ton vs. ~1000 $/ton). The coating materials and processing are also low cost, low-energy, and scalable. Therefore, the black-coated quartz sand developed here could become a promising cost-effective HTM and TES material for CSP. It also opens the possibility of optimizing the optical and thermal properties of solid particles by coating them with suitable materials. Further work could focus on the application of the process to a large quantity of sand and a more thorough evaluation of its chemical thermal stability, abrasion resistance, and flowability (e.g., in a moving particle heat exchanger (*199*)).

Acknowledgements

Chapter 5 is a full reprint of **K. M. Chung**, and R. Chen. "Black coating of quartz sand towards low-cost solar-absorbing and thermal energy storage material for concentrating solar power." *Solar Energy* 249 (2023): 98-106. For this work, K. M. Chung performed experiments, data analysis and manuscript writing.

Chapter 6. Realizing ultra-low thermal conductivity and diffusivity at high temperatures using packed high-entropy spinel oxide nanoparticles

6.1. Introduction

Thermal insulation at high temperature is essential for performance, durability, and safety in various applications (*201*). For example, thermal barrier coatings (TBCs), mainly consisting of low-thermal conductivity metal oxides, are used as excellent thermal insulation layers to enable the operation of gas turbine engines for aerospace and electricity generation applications at high temperatures (i.e., > 1300 ^{o}C) (*202*). Thermal insulation for buildings is also critically important to reduce the increasing energy consumption for thermal comfort (*203, 204*). Low thermal conductivity and fire retardance are desirable for energy efficient and safe building envelops (*205*). Solid oxide fuel cells (SOFCs) are emerging electrochemical energy storage devices that generate electricity with zero-emission. Their principle relies on the catalytic redox reactions and ionic conduction across the electrolytes at high operating temperatures of 800-1000 °C (*206*). Excellent, insulation layers with high thermal and chemical stability are required to maintain the cells above their minimal operating temperatures. Thermal runaway in lithium-ion batteries (*207*) could lead to temperature as high as 1000 ^{o}C (*208*). One of the promising mitigation strategies is installing a thin thermal runway barrier material in the batteries to delay thermal propagation (*209, 210*). Other important applications include firefighting protective clothing (*211*), space re-entry vehicles (*212*), spacecrafts (e.g., Parker Solar Probe (*213*)).

A desirable thermal insulation material should exhibit as low as possible thermal conductivity and a promising mechanical behavior that can satisfy the technological requirements. In the last few decades, solid-like thermal insulation materials have been

fabricated to meet different thermal insulation requirements. They can be divided into dense and porous solids. Dense thermal insulation materials are usually metal oxides. Yttria-Stabilized Zirconia, with 7-8 mole % (7YSZ or 8YSZ) is a state-of-the-art dense thermal insulation material. It has a bulk thermal conductivity of around 3.0 W m^{-1} K^{-1} at room temperature and gradually decreases down to around 2.5 W m^{-1} K^{-1} at 1000 ^{o}C (*44, 214, 215*). The underlying thermal transport mechanism for achieving low thermal conductivity is phonon scattering. The phonon scattering in the materials can be increased by different means, for example, the introduction of complex compositions, doping of metal cations, and increasing the size and mass deviation of constitutional cations (*44, 46*). Porous solids are another type of promising thermal insulation material. They are two-phase effective media that consist of both solid and stagnant gas. The effective thermal conductivity of porous structures (κ) can be expressed in the general form (*44*):

$$\kappa = \kappa_{solid} + \kappa_{gas} + \kappa_{rad} \tag{6.1}$$

where κ_{solid} is the heat conduction through solid, κ_{gas} is the heat conduction through gas, and κ_{rad} is the heat conduction through thermal radiation, respectively. Aerogels (*216-228*), scaffolds (*229, 230*), fibers (*231*), porous refractory bricks (*43*), and foams (*232-234*) are representatives of porous thermal insulation materials. Introducing a high porosity to the materials, κ_{solid} can be greatly reduced by limiting the solid matrix contact areas and enhancing boundary scattering. On the other hand, heat conduction through gas becomes significantly more dominant. Those porous thermal insulation materials thus attain a more gas-like thermal conductivity, for instance, air thermal conductivity at room temperature (e.g., k_{air} = 0.026 W m^{-1} K^{-1}). The gas conduction in the porous materials can be further reduced when the pore size is comparable to the mean free path (MFP) of the stagnant gas, namely the Knudsen effect (*234-237*). It implies that thermal conductivity in porous structures can be further suppressed by

limiting the gas molecule propagation length. While both dense and porous thermal insulation materials can achieve low thermal conductivity by altering the thermal transport mechanisms through solid and gas pathways, however, there are scarce strategies to suppress the heat transfer through thermal radiation at high temperatures in the thermal insulation materials. The thermal conductivity of those insulation materials is anticipated to show a substantial increase in thermal conductivity at high temperatures due to thermal radiation, limiting their thermal insulation capabilities at high temperatures where heat transfer through thermal radiation is significant.

In 2006, Prasher (*238*) reported a theoretical prediction of low thermal conductivity using packed nanoparticles. The theoretical results show that by choosing nanoparticles with suitable physical properties, including particle sizes, bulk thermal conductivity, surface energy, etc., the packed nanoparticles can achieve thermal conductivity lower than that of air. In the following year, Hu, Prasher, and Lofgreen (*239*) experimentally showed a low thermal conductivity of packed alumina nanoparticles of 0.035 W m^{-1} K^{-1} at room temperature. It approaches air thermal conductivity without evacuation. It provides an alternative to ultra-low-thermal conductivity thermal insulation materials with low-cost, tunable thermal transport and mechanical properties.

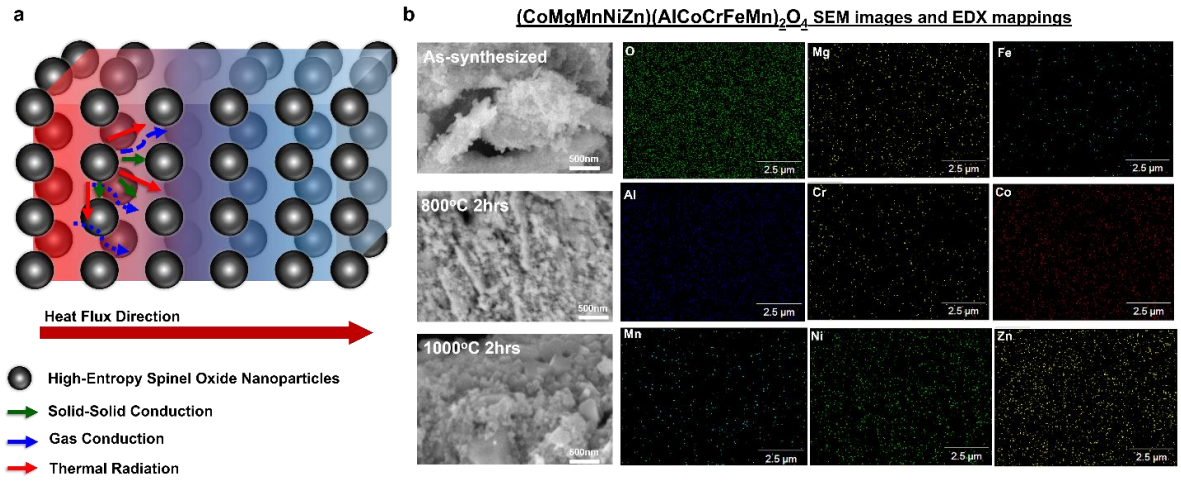

Figure 6.1 (a) Schematic of packed HESONPs and the heat transfer mechanisms (solid conduction, gas conduction, and thermal radiation) in the packed nanoparticle constriction. The heat transfer pathways, including solid-solid conduction, gas conduction, and thermal radiation, are suppressed, illustrated by the reduced pathways; **(b)** SEM Images and EDS mapping of HESO NPs showing its morphological changes upon thermal treatment at high temperatures (1000 ^{o}C) and its compositional homogeneity.

In this work, we report ultra-low thermal conductivity at high temperatures (0.080 W m^{-1} K^{-1} at 1000 ^{o}C) in ambient air using packed high-entropy spinel oxide nanoparticles (HESO NPs) with a composition of $(CoMgMnNiZn)(AlCoCrFeMn)_2O_4$. **Figure 6.1a** shows the concept and schematic of suppression in heat transfer pathways, including solid conduction, gas conduction, and thermal radiation, using packed nanoparticle constriction in our work. The thermal conductivity of packed HESO NPs from 300 to 1000 ^{o}C was measured using modulated photothermal radiometry (MPR). It shows a nearly constant thermal conductivity trend and a thermal conductivity that approaches air thermal conductivity at 1000 ^{o}C (0.080 W m^{-1} K^{-1}, at 1000 ^{o}C), and much lower than aerogel-based thermal insulation materials (0.21 W m^{-1} K^{-1}, at 1000 ^{o}C) (*240*). More importantly, due to its relatively high packing density, thermal diffusivity of packed HESO NPs is almost 1000-fold lower than that of air (0.0227 *vs.* 240.0 mm^2 s^{-1} at 1000 ^{o}C). HESO NPs in our work show excellent sintering resistance. Its thermal conductivity and particle size remain nearly unchanged after high-temperature thermal treatment. It further

demonstrates the HESO NPs as an excellent thermal insulation material with the capability of operating under extreme conditions. The work sheds new lights on the design of the next-generation thermal insulation materials. It, on the other hand, would be useful for various technologies such as gas turbine engines, buildings, and energy storage devices, where thermal insulations are critically important for safety and materials protection.

6.2.Experiment

6.2.1. Materials synthesis

$(CoMgMnNiZn)(AlCoCrFeMn)_2O_4$ HESO NPs with 8 different cations was prepared using hydrothermal synthesis (*161*). The constitutional water-soluble metal salts were weighted and dissolved in deionized (DI) water with specific mole concentrations. The as-prepared solutions were then mixed and stirred for 1 h to enable compositional uniformity. To form precipitates, 10 M NaOH was added to the resultant solutions until a pH level of 11.5 was reached. The viscous solution was further mixed. It was then put in Teflon-lined autoclaves for thermal treatment at 200 °C for 20 h in an oven. After that, the solid sample obtained was washed with DI water and further purified using a centrifuge. The as-obtained solid sample was dried overnight in an oven of around 70 ^oC. They were then heated in a box furnace at 550 °C for 5 h in air to remove any water crystallization. After the thermal treatment, the sample was around to obtain nanoparticles for thermal and materials characterization. For comparison, another type of high-entropy spinel oxide with five cations, $(CoCrFeMnNi)_3O_4$, and a simple spinel oxide, $CuCr_2O_4$ were synthesized using the same method (*161*).

6.2.2. Thermal conductivity measurement

The thermal conductivity of packed HESO NPs was determined using the MPR method which is a non-contact frequency-domain thermal characterization technique. The setup and experimental details of MPR measurements are documented in ref (*69*) (**Figure 6.3a**). The packed HESO NPs were first prepared using a cold-press method. A weighted amount of HESO NPs was filled into the designated MPR sample holder for high-temperature measurements up to 1000 ºC. The nanoparticles were pressed by a hydraulic press with an exerted pressure up to 40 MPa. The packed HESO NPs then formed a solid, robust bulk piece for measurement. Upon the measurements, the packed nanoparticles were heated by a modulated laser that provided a periodic heat flux of $q = q_0 e^{i\omega t}$, where q_0 is the amplitude of the heat flux and ω is the modulated angular frequency. The surface temperature oscillation of $\theta = \theta_0 e^{i(\omega t+\phi)}$, where θ_0 is the amplitude surface temperature oscillation and ϕ is the phase lag between the heating and the thermal response, was monitored by an ultra-fast Infrared (IR) detector and a high-temperature pyrometer. The voltage (V) reading from the IR detector was converted to the actual thermal response of the sample based on the established $|\theta_0| - V$ calibration curve. By utilizing the $|\theta_0| - \omega^{-\frac{1}{2}}$ data obtained from the measurements, the thermal conductivity of the sample can be obtained. The detailed heat transfer model for the MPR measurement is provided in ref (*69*). Briefly, the physical meaning of the slope of $|\theta_0| - \omega^{-\frac{1}{2}}$ plot (m) of a sample represents the inverse of its thermal effusivity (e), defined as $e = \sqrt{\rho c_p \kappa}$ where ρ, c_p and κ are density, specific heat capacity, and thermal conductivity , respectively. Using a differential method, the thermal effusivity of a sample can be obtained by comparing with the reference (*69, 70, 150*):

$$e = \frac{m_{ref}}{m} e_{ref} \tag{6.2}$$

where m_{ref} and e_{ref} are the slope of $|\theta_0| - \omega^{-\frac{1}{2}}$ plot for the reference and the thermal effusivity of reference, respectively. The measured e_s is then converted to k using the following relation:

$$\kappa = \frac{e^2}{\rho c_p} \tag{6.3}$$

Pyroceram 9606 was used as the reference because of its well-established thermophysical properties in the entire temperature range (*241*, *242*). The packing density was obtained directly by dividing the mass of particles loading and the volume of the sample holder filled by the packed nanoparticles. The Neumann-Kopp rule was used for c_p estimation (*159*, *160*). The thermal insulation capability of materials is also dictated by thermal diffusivity (α) which measures how fast thermal energy transfers to an object. It is given by:

$$\alpha = \frac{\kappa}{\rho c_p} \tag{6.4}$$

6.2.3. Thermal insulation test

A home-built thermal insulation setup was used to examine the flame resistance and the ability of the samples to delay thermal propagation. In the test, the samples were fixed by stands and clamps. To avoid the burning of the testing materials, a stainless-steel shim was mechanically attached to the front side of the samples. The front side (covered by the stainless-steel shim) of as-prepared packed HESO NPs (3 cm × 3 cm × 1 cm) housed in an Inconel sample holder, and fiberglass (10 cm × 10 cm × 1 cm), a commercially available thermal insulation materials, were subjected to propane blowtorch heating (~ 950 ^{o}C). The thermal insulation ability of ambient air was also tested using the same method. Two stainless-steel shims (10 cm × 10 cm × 100 μm) were separated by 1 cm which was for creating an air gap of 1 cm. The temperature

rise of the backside of the samples as a function of time was recorded using a high-temperature pyrometer (Lumasense Technologies IGA 320/23-LO).

6.2.4. Materials characterization

The surface morphology and compositional homogeneity of HESO NPs were examined by Scanning Electron Microscopy (SEM) (FEI Quanta 250 SEM) equipped with Energy-dispersive X-ray spectroscopy (EDS). The crystal structure of HESO NPs was confirmed using the Rigaku Smartlab X-ray diffractometer (Cu Kα, λ = 0.15418 nm) as the radiation source. Thermogravimetric Analysis (TGA) was performed to determine the thermal stability of HESO NP samples using a thermogravimetric analyzer (Pyris 1 TGA). The weight (%) of nanoparticles placed in an Alumina crucible was measured up to 1000 ^{o}C at a heating rate of 20 K min^{-1} in air.

6.3. Results and Discussion

6.3.1. Materials characterization

The packed HESO NPs were black in appearance before and after the MPR measurements with temperatures up to1000 ^{o}C (**Figure 6.2a**). The packed nanoparticles show no changes in appearance, revealing the optical, thermal, and mechanical stability of the packed HESONPs. They were further quantified by optical property and thermal stability measurements using diffusive reflectance measurement and TGA respectively. The surface morphology of the packed HESO NPs was examined under SEM. As shown in **Figures 6.1b** & **6.2b**, the particle sizes of HESO NPs were maintained at nano-sizes before and after the MPR measurements. The pore sizes between the particles are also of nano-size order. The chemical homogeneity of HESO NPs was confirmed using EDS mapping which shows that the 8 cations are uniformly distributed across the sample **(Figure 6.1b**).

Figure 6.2c shows the TGA results of HESO NPs before and after 1000 ^{o}C heat treatment for 2 h, presented as a plot of weight (%) as a function of temperature. The weight change of the samples is merely 1-2 % after the heat sweep to 1000 ^{o}C, with a heating rate of 20 K min^{-1}. It shows the excellence of HESO NPs to withstand high temperatures without degradation. HESO NPs also have high phase stability. It exhibits a single spinel structure upon synthesis and high-temperature treatment at 800 ^{o}C and 1000 ^{o}C (**Figure 6.2d**). The absorptance of the packed HESO NPs before and after 1000 ^{o}C thermal treatment for 2 h is shown in **Figure 6.2e**. The results show that HESONPs are highly absorptive. The absorptance did not change after the thermal treatment, revealing the optical stability of HESO NPs.

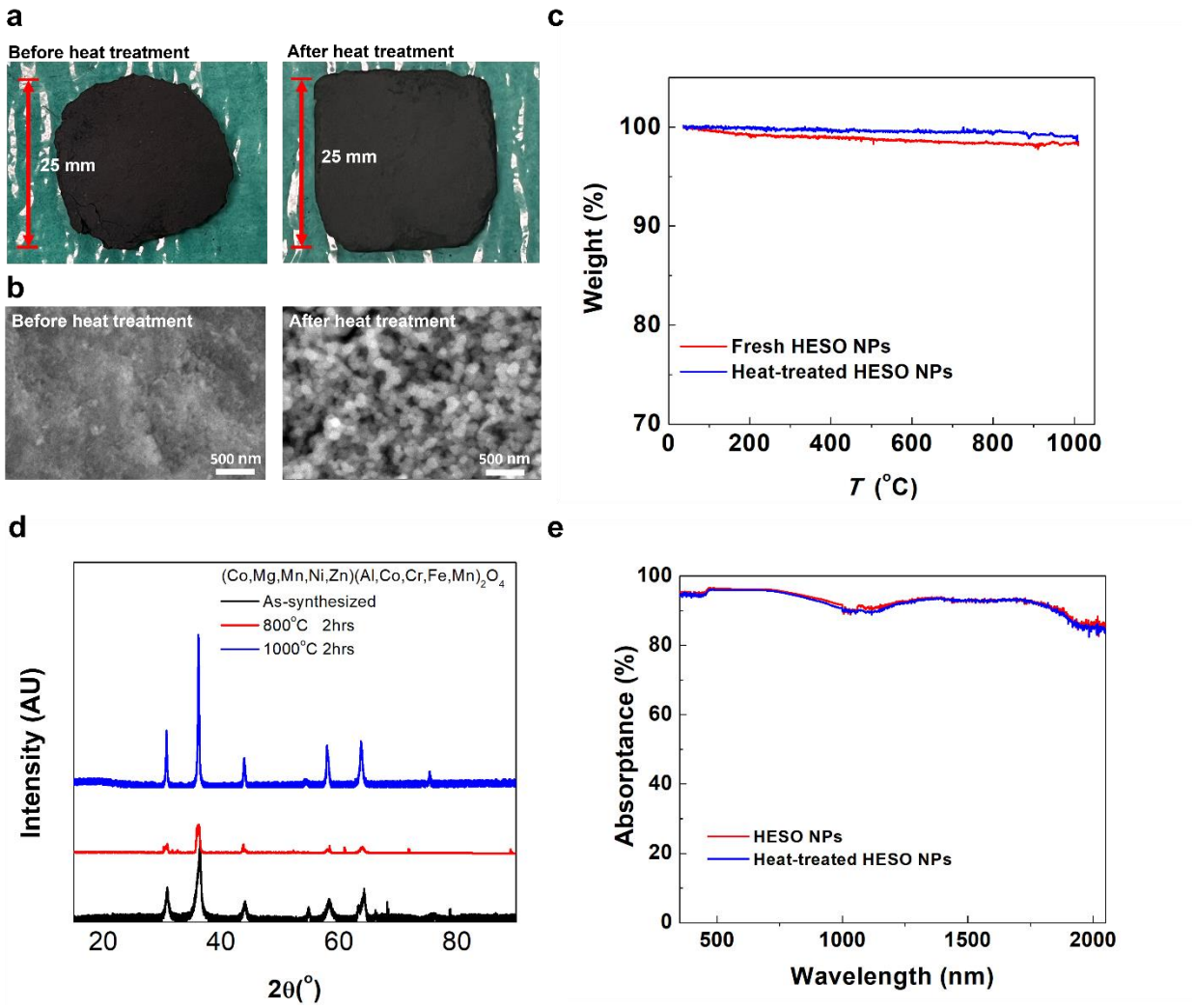

Figure 6.2 Materials characterization results: **(a)** digital photos of packed HESO NPs before and after the MPR measurements; **(b)** SEM images of the packed HESO NPs before and after high-temperature annealing. The particles maintained the nano sizes; **(c)** TGA results of HESO NPs up to 1000 ^{o}C showing their high thermal stability; **(d)** XRD patterns of HESONPs which shows single spinel-phase upon synthesis and thermal treatment at 800 and 1000 ^{o}C for 2 h, respectively; and **(e)** absorbance of packed HESO NPs in the wavelength from 350 nm to 2000 nm.

6.3.2. Thermal conductivity and thermal diffusivity results

Figure 6.3b shows the κ *vs.* T plot of packed HESO NPs and the other two types of packed spinel oxides nanoparticles, namely $(CoCrFeMnNi)_3O_4$ and $CuCr_2O_4$. The raw data of the MPR measurements of packed HESO NPs is included in **Figure 6.4**. The reported values of the state-of-the-art low-thermal conductivity materials or composites were plotted alongside for

comparison (*43, 220, 230*). When *T* increases from 300 to 1000 ^{o}C, κ of packed HESONPs show a small increase from 0.070 to 0.080 W m^{-1} K^{-1}. At the highest measurement temperature, packed HESO NPs show almost the same thermal conductivity as air (0.080 W m^{-1} K^{-1}). It is the first realization of high-temperature thermal insulation with a record low thermal conductivity that is comparable to that of air under an ambient environment. Heat-treated packed HESO NPs (at 1000 ^{o}C) show a very similar thermal conductivity trend as a function of temperature compared to the original packed HESO NPs, revealing the excellent thermal stability of the packed HESO NPs for thermal insulation applications at high temperatures without thermal degradation. It is consistent with the materials characterization results as shown in **Figure 6.2**. Packed HESO NPs have outstanding thermal insulation ability compared to state-of-the-art thermal insulation materials, for example, porous alumina refractory brick. It has a much lower thermal conductivity at high temperatures compared to the reported data of porous alumina refractory brick (0.080 *vs.* 0.32 W m^{-1} K^{-1} at 1000 ^{o}C) (*43*). The substantial increase in thermal conductivity of the porous alumina refractory brick at high temperatures is attributed to the thermal radiation contribution. Our packed HESO NPs are the only materials among the others for comparison, that show ultra-low and air-like thermal conductivity at high temperatures under ambient pressure. The realization of ultra-low thermal conductivity of HESO NPs is due to three reasons: (1) small contact between nanoparticles; (2) nanoscale pores formation with dimensions less than the mean free path of air; and (3) scattering of thermal radiation in packed nanoparticles. For the first two reasons, it has already been verified by both theoretical models and experimental results (*238, 239*). They are responsible for the reduction of solid-solid conduction and gas conduction. For the third reason, it is especially important for the reduction in thermal radiation. Both the metallic (absorptive) nature of the spinel oxides and the porous structure constructed by

nanoparticles provide highly effective absorption and scattering mechanisms for infrared photons, thus resulting in the elimination of thermal radiation contribution (*243*, *244*).

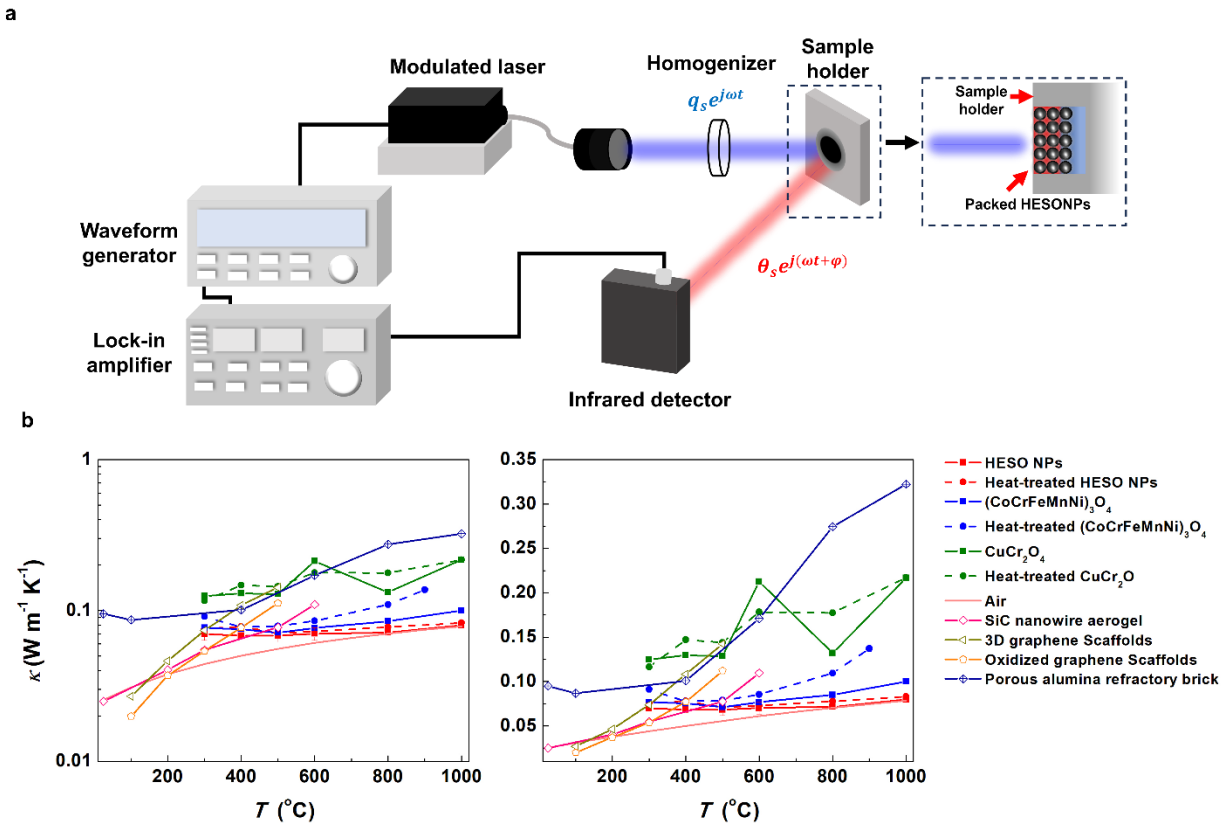

Figure 6.3 Thermal conductivity measurement results: **(a)** schematic of MPR measurement setup; **(b)** *κ vs. T* of packed HESONPs, packed $(CoCrFeMnNi)_3O_4$ and $CuCr_2O_4$ up to 1000 °C. The reported literature results of the other thermal insulation materials from refs (*43*, *220*, *230*) are plotted alongside for comparison. The LEFT panel is the *κ vs. T* plot on a logarithmic scale; the RIGHT panel is the enlarged *κ vs. T* plot on a linear scale.

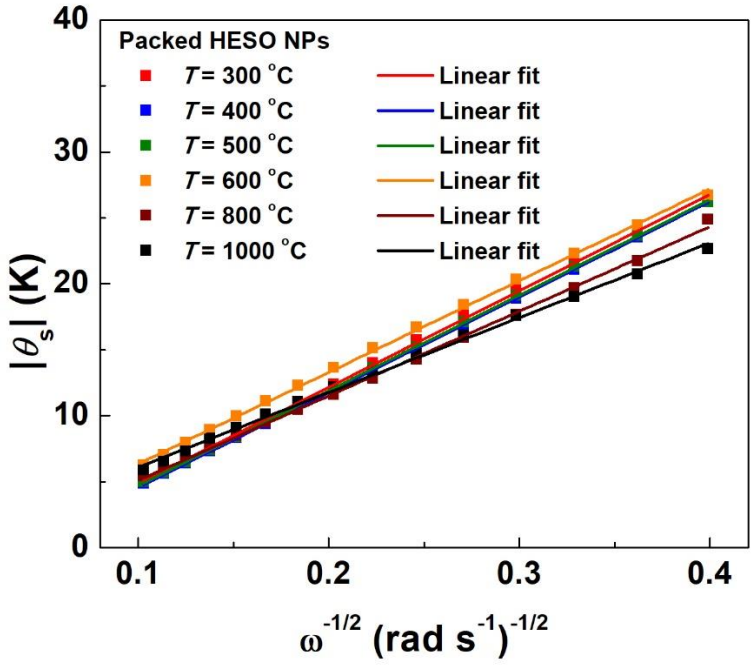

Figure 6.4 Raw data of MPR measurements of packed HESO NPs plotted as $|\theta_s|$ *vs.* $\omega^{-\frac{1}{2}}$

Both packed $(CoCrFeMnNi)_3O_4$ and $CuCr_2O_4$ show slightly higher κ compared to packed HESO NPs.Packed $CuCr_2O_4$ in general are higher in κ in the entire temperature range. Different from packed HESO NPs, packed $(CoCrFeMnNi)_3O_4$ shows flat thermal conductivity values of around 0.077 W m^{-1} K^{-1} from 300 to 600 ^oC. It then increases to 0.10 W m^{-1} K^{-1} at 1000 ^oC. Packed $CuCr_2O_4$, on the other hand, shows an almost linear increase in κ from 0.12 to 0.22 W m^{-1} K^{-1} from 300 to 1000 ^oC. The abnormal data point at 600 ^oC may be associated with the structural phase transition of $CuCr_2O_4$ (*245*). In the repeat measurements, both packed $(CoCrFeMnNi)_3O_4$ and $CuCr_2O_4$ show slight increases in thermal conductivity which is a sign of thermal insulation degradation. The difference in thermal conductivity of HESO NPs and the other two packed spinel oxide nanoparticles can be attributed to two factors, namely particle sintering upon high-temperature treatment and the difference in mechanical properties. It was

observed that $(CoCrFeMnNi)_3O_4$ and $CuCr_2O_4$ nanoparticles sintered and agglomerated to micro-sizes (**Figure 6.5**). In fact, thermal insulation materials lose their insulation capability upon sintering. When packed nanoparticles are sintered and agglomerated into large sizes, the particles have large contact areas for thermal transport. It, thus, increases thermal conductivity. Packed HESONPs show a unique thermal insulation capability compared to the other two spinel oxide nanoparticles owing to their sintering resistance. It makes them remain highly insulated even after high-temperature thermal treatment. The origin of the excellent sintering resistance of HESONPs is still unclear. Such sintering resistance can be observed in other high-entropy material systems (*246, 247*). There is still a lack of a unified theory to account for this phenomenon. One may suggest that it is associated with the sluggish effect of high-entropy materials (*248, 249*). However, it was reported that the number of components in the high-entropy materials do not affect the kinetic diffusion (*250-252*). The proposed sluggish effect may not be a convincing explanation. High-entropy grain boundary (HEGB) was first proposed in 2016 as the grain boundary counterpart to high-entropy materials (*253*). It explains the nanocrystalline stability at high temperatures from the point of view of interfacial thermodynamics. In general, grain growth of high-entropy materials can be inhibited via thermodynamic stabilization by reducing the grain boundary surface energy, and/ or kinetic stabilization by solute drag (*253*). Both thermodynamic and kinetic stabilizations are likely to contribute to the suppression of particle growth of HESONPs, enabling a stable surface of nanoparticles for high-temperature thermal insulations.

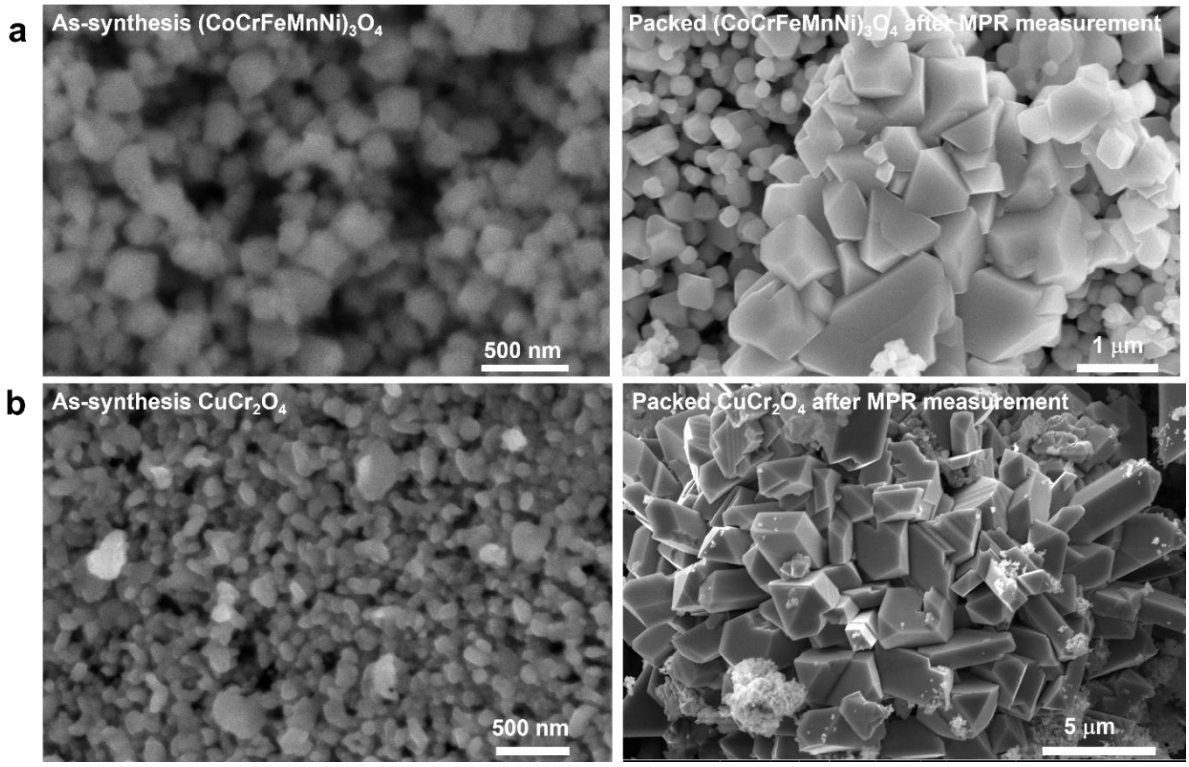

Figure 6.5 SEM images of **(a)** as-synthesis $(CoCrFeMnNi)_3O_4$ and packed $(CoCrFeMnNi)_3O_4$ after the MPR measurement, respectively; and **(b)** as-synthesis $CuCr_2O_4$ and packed $CuCr_2O_4$after the MPR measurement, respectively.

According to the result presented in **Figure 6.3b**, the thermal conductivity of the packed nanoparticles is given in the following descending order: $CuCr_2O_4$ > $(CoCrFeMnNi)_3O_4$ > $(CoMgMnNiZn)(AlCoCrFeMn)_2O_4$. The mechanical property deviation in those spinel oxide nanoparticles may be the explanation for this. It was predicted by Prasher (*238*) that the lower the surface energy of nanoparticles, the lower the thermal conductivity of the packed nanoparticles. Without a solid experimental foundation of the mechanical properties of the spinel oxide nanoparticles, we hypothesize that high-entropy ceramics show lower surface energy than that of simple ceramics and compositionally-less-complex ceramics. It is empirically true in some high-entropy ceramic systems (*254-256*). Using it as a rule of thumb, we can then explain the observed thermal conductivity of spinel oxide nanoparticles where the most compositionally complex one, $(CoMgMnNiZn)(AlCoCrFeMn)_2O_4$, attains the lowest thermal conductivity, while

packed $CuCr_2O_4$ displays the highest thermal conductivity. Substantial experimental work shall be made to verify the effect of the mechanical properties of nanoparticles on the thermal transport properties.

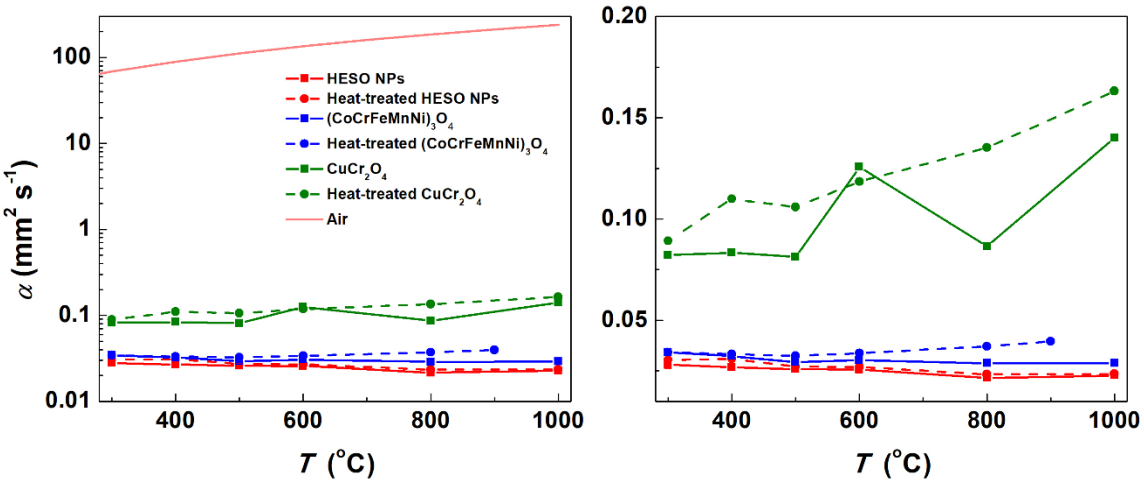

Figure 6.6 *α vs. T* of packed HESONPs, packed $(CoCrFeMnNi)_3O_4$ and $CuCr_2O_4$ up to 1000 °C. Thermal diffusivity of air is plotted alongside for comparison. The left panel is the *α vs. T* plot on a logarithmic scale; the right panel is the enlarged *α vs. T* plot on a linear scale.

Figure 6.6 summarizes the measured *α* of packed HESO NPs, $(CoCrFeMnNi)_3O_4$ and $CuCr_2O_4$ with the reported values of air for comparison. Packed HESO NPs show a constant *α* in the entire temperature range from 300 to 1000 °C. It is 1000 times lower than that of air (0.0227 *vs*. 240.0 $mm^2\ s^{-1}$ at 1000 °C). It is not surprising since packed HESO NPs have a high packing density (~ 2700 $kg\ m^{-3}$) which leads to a much lower *α* compared to air. The thermal diffusivity results reveal that a much longer time is needed for thermal energy to diffuse in packed HESO NPs while it is almost instantaneous for thermal energy to diffuse in an air gap with an equivalent thickness as packed HESO NPs. It can be further illustrated in the thermal insulation demonstration in *Section 6.3.3*. Although packed $(CoCrFeMnNi)_3O_4$ and $CuCr_2O_4$ exhibit similar packing densities compared to that of packed HESO NPs, they still have slightly higher *α*. It is consistent with their higher measured *κ* results (**Figure 6.3b)** attributing to the difference in

mechanical properties and their thermal insulation degradation upon sintering. To summarize, packed HESO NPs show ultra-low thermal diffusivity compared to air and other nano-constriction formed by spinel oxides. It shows a great potential of applying packed HESO NPs as an excellent thermal barrier material.

6.3.3. Thermal insulation test

The flame resistance and thermal insulation capability of samples were tested using a home-build setup (**Figure 6.7a**). Upon heating by a propane blowtorch, the stainless-steel shim inserted on the front side of samples experienced a temperature rise to ~ 950 ^{o}C in 15 secs. After the SS shim reached thermal equilibrium, the heat was then transferred to the samples, namely air gap, fiberglass, and packed HESO NPs. **Figure 6.7b** shows the backside temperature rise of the samples as a function of time. It is obvious that air and fiberglass quickly heated to their maximum temperature and plateaued in less than 3 mins. It is consistent with the fact of high thermal diffusivity of air and fiberglass. On the other hand, packed HESO NPs display a much slower temperature rise behavior. It took almost 20 mins for packed HESO NPs to reach the back temperature equilibrium. It aligned with our experimental results of packed HESO NPs that have a much lower thermal diffusivity.

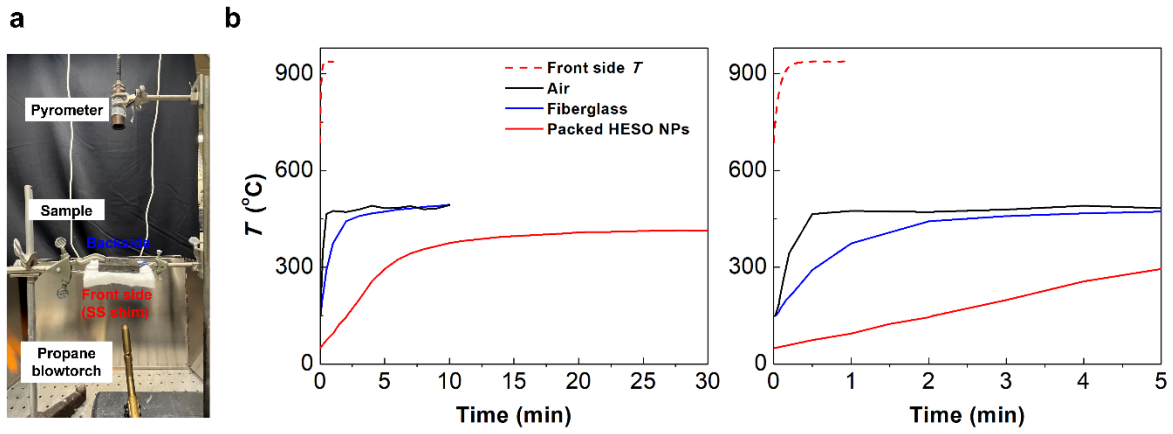

Figure 6.7 Thermal insulation demonstration: **(a)** digital photo of the thermal insulation demonstration setup with the key components labeled; **(b)** measured back side temperature as a function of time for different thermal insulation materials: air, fiberglass, and packed HESO NPs

The demonstration presented here provides strong evidence of the excellent thermal insulation capability of packed HESO NPs. The applications of packed HESO NPs, or in general nanoparticles with certain sintering resistance, are imperative for technologies that require intensive thermal insulation. For instance, thermal barrier materials are urgently needed to prevent TR propagation. However, the performance of commercial thermal barrier materials is still far from satisfactory owing to their limited capability to prevent thermal propagation and material degradation under extreme conditions (*208*). Our packed HESO NPs may open a new possibility of excellent thermal insulation for multiple critical areas, such as TR, with such nanocontrictions exhibiting ultra-low thermal conductivity and diffusivity.

6.4. Conclusion

In summary, here we report ultra-low thermal conductivity (0.080 W $m^{-1} K^{-1}$ at 1000 ^{o}C) and diffusivity (0.0227 mm^2 s^{-1} at 1000 ^{o}C). realized by using packed high-entropy spinel oxide nanoparticles (HESO NPs) under an ambient environment. Utilizing the unique features of the nanocontriction formed by HESO NPs, all three heat transfer mechanisms in porous structures, namely solid-solid conduction, gas conduction, and thermal radiation, are suppressed. An air-like

thermal conductivity of packed HESO NPs can, therefore, be achieved without evacuation. Moreover, owing to the high packing density of packed HESO NPs compared to traditional thermal insulation material with high porosities, it exhibits 1000 times lower thermal diffusivity. At a material level, taking advantage of the unusual material properties of high-entropy materials, HESO NPs show excellent sintering resistance and thermal stability. It makes it competitive to beat other traditional thermal insulation materials without the issues of degradation. The work can potentially have a game-changing impact on the design of the next-generation thermal barrier materials. It will be particularly useful for various technologies such as gas turbine engines, buildings, and energy storage devices, where thermal insulation is critically important for safety and materials protection.

Acknowledgements

Chapter 6 is currently being prepared for submission as **K. M. Chung**, S. R. Adapa, L. Chen, J. Luo, Z. Liu, R. Chen. "Realizing Ultra-low Thermal Conductivity and Diffusivity at High Temperatures using Packed High-Entropy Spinel Oxide Nanoparticles". *in Prep*.

Chapter 7. Conclusion and outlook

7.1. Summary

The next-generation CSP brings promising perspectives on providing reliable zero-carbon emission electricity supply by utilizing concentrated sunlight, high-temperature materials (including HTFs, TES materials, and TCMs), and efficient thermal infrastructure with excellent internal insulation. Yet, due to technological immaturity and the lack of our understanding of materials at high temperatures, research and development efforts must be devoted to enabling a decarbonized future world with the implementation of such solar-thermal technology. The research work presented in the previous chapters has provided possible solutions and future directions to the bottlenecks aforementioned.

7.1.1. Instrumentation and measurement

At instrumentation and measurement levels, a novel, non-contact, frequency-domain thermal characterization technique, MPR, was developed for measuring high-temperature HTFs, such as molten salts. It has been proven as a reliable tool for capturing the true thermal conductivity of molten salts, which is challenging to measure due to its corrosivity and measurement errors from natural convection and radiation. Beyond providing a thermal conductivity measurement technique, the MPR techniques can also serve as a diagnostic tool for monitoring dynamic thermal systems in real time. The systems include HTFs in flowing states and thermochemical reactions. By integrating the MPR setup into an existing lab-scale molten salt flow loop, we demonstrated the first in-situ thermal conductivity measurement of flowing chloride molten salts. It is the first realization of real-time monitoring of the heat transfer performance of flowing molten salts using an optical method. In addition, we exploited the MPR

techniques to monitor the kinetics of thermochemical reactions for TES and solar-thermochemical fuel production applications based on thermal response. It successfully correlated the thermal conductivity of TCMs with their reaction kinetics, providing the communities with a convenient and useful tool to study thermochemical reactions in the reactors during their operating conditions. In short, the instrumentation development and reliable thermophysical property data obtained in the study are useful and will contribute to the CSP and related research communities for further sophisticated development and implementation of the technology.

7.1.2. Materials design and engineering

At materials levels, we modified low-cost quartz sand using black spinel oxide coating. The proposed, black-coated quartz sand has comparable optical properties, thermal properties, and stability, but almost 20 times lower cost (30–50 $/ton vs ∼1000 $/ton) compared to the state-of-the-art ceramic particles used for the same purpose. The method in the work is also facile, energy-efficient, and cost-effective, making it competitive to extend it to a large-scale coating process. It can potentially be an alternative HTFs and TES materials for the next-generation CSP that can further lower the LCOE of the technology.

On the other hand, our hydrothermal synthesized HESO NPs, namely, $(CoMgMnNiZn)(AlCoCrFeMn)_2O_4$, show excellent thermal insulation ability at high temperatures (> 1000 ^oC). The pressed nano-constriction formed by the as-synthesis HESO NPs show ultra-low thermal conductivity (0.08 W m^{-1} K^{-1} at T = 1000 ^oC) and thermal diffusivity (0.023 mm^2 s^{-1} at T = 1000 ^oC). Owing to nano-constriction formed by the nanoparticles, suppress the heat transfer mechanisms of solid-solid conduction, gas conduction and convection, and thermal radiation. The realization of ultra-low thermal conductivity and diffusivity can be

applied to the internal insulation of the thermal infrastructure of CSP plants to improve the overall efficiency of the systems.

7.2. Future plans

7.2.1. Novel instrument for monitoring energy devices

Utilizing the features of the MPR technique, namely non-invasive monitoring, controllable thermal penetration depth, and high-throughput measurement, one can apply it to monitor energy devices, such as lithium-ion batteries (LIBs) and solid oxide fuel cells (SOFCs), for real-time evaluation of the energy devices. Despite the success of the commercialization of batteries, there are still safety concerns induced by abusive usage of the devices. When the batteries are abusively employed, a series of uncontrollable chain reactions occur and lead to explosive consequences, namely, thermal runaway (TR). The cause of thermal runaway is complex and still unclear. To enable the safe operation of the energy devices and provide a convenient diagnostic tool for studying the devices, including real-time monitoring, degradation mechanism study, and fundamental structure-property relationship investigation, we propose the use of the MPR technique to study the energy device. To be specific, the performance of the sub-components of energy devices can be correlated with their thermophysical properties. One can then predict and evaluate the performance of the devices.

7.2.2. Materials design for solar-thermochemical applications

Agglomeration and materials deactivation under high temperatures and hot-spot heating have long been the issue of redox-active materials (usually in particle forms with micro sizes) for solar-thermochemical fuel production. It leads to an efficient conversion, becoming one of the bottlenecks of technology. Inspired by the experimental realization of suppressed grain growth in

HECs (see Chapter 7), it suggests that the use of coating formed by HECs can act as a protective layer to eliminate or minimize agglomeration of the redox-active particles. In future research work, more effort will be made to investigate how HECs with slow or negligible can be applied to redox-active materials can eliminate particle agglomeration, which is the major cause of low conversion efficiency and materials degradation. HECs take advantage of possessing excellent and unique material properties and are highly versatile in modifying the materials system for a vast composition space, there are also great opportunities in designing HECs that contain redox-active cation species while showing the sluggish effect that helps maintain the materials with desirable particle sizes.

7.2.3. Thermal barrier materials for thermal runaway

Thermal runaway is a critical issue that is associated with the safe operation of battery systems. While tremendous research effort has been made to investigate the fundamental causes of TR, mitigation strategies are also necessitated to enable the safe operation of batteries. The usage of flame-retardant phase change materials (PCMs) is one of the potential solutions to TR which aims to delay thermal propagation by a rapid decrease in thermal conductivity upon phase change induced by the thermal excitation by TR (*209, 257*). Based on our study on (see Chapter 7) packed HESO NPs, nano-constriction provides not only ultra-low thermal conductivity but also low thermal diffusivity, which implies that they can provide transcending thermal insulation ability. It opens the possibility of introducing such nano-constriction layers to mitigate TR.

References

1. H. Lee, K. Calvin, D. Dasgupta, G. Krinmer, A. Mukherji, P. Thorne, C. Trisos, J. Romero, P. Aldunce, K. Barret, Synthesis report of the IPCC Sixth Assessment Report (AR6), Longer report. IPCC. (2023).
2. L. Hammarström, Overview: capturing the sun for energy production. *Ambio* **41**, 103-107 (2012).
3. International Energy Agency, (IEA), "Electricity Information" (IEA, 2023; https://www.iea.org/reports/electricity-information-overview)
4. Y.-L. He, Y. Qiu, K. Wang, F. Yuan, W.-Q. Wang, M.-J. Li, J.-Q. Guo, Perspective of concentrating solar power. *Energy* **198**, 117373 (2020).
5. M. T. Islam, N. Huda, A. Abdullah, R. Saidur, A comprehensive review of state-of-the-art concentrating solar power (CSP) technologies: Current status and research trends. *Renewable and Sustainable Energy Reviews* **91**, 987-1018 (2018).
6. S. Kuravi, J. Trahan, D. Y. Goswami, M. M. Rahman, E. K. Stefanakos, Thermal energy storage technologies and systems for concentrating solar power plants. *Progress in energy and combustion science* **39**, 285-319 (2013).
7. M. Mehos, C. Turchi, J. Vidal, M. Wagner, Z. Ma, C. Ho, W. Kolb, C. Andraka, A. Kruizenga, "Concentrating solar power Gen3 demonstration roadmap" (National Renewable Energy Lab.(NREL), Golden, CO (United States), 2017).
8. B. H. Mills, C. K. Ho, N. R. Schroeder, R. Shaeffer, H. F. Laubscher, K. J. Albrecht, Design evaluation of a next-generation high-temperature particle receiver for concentrating solar thermal applications. *Energies* **15**, 1657 (2022).
9. Solar Energy Technologies Office, (SETO), "2030 Solar Cost Targets" (SETO, 2021, https://www.energy.gov/eere/solar/articles/2030-solar-cost-targets)
10. A. Gunawan, B. K. Arkhurst, S. A. Brankovic, S. K. Yee, Gen3 CSP Materials: Critical Review of Limited Existing and New Survey Data. *Energy Sustainability* **83631**, V001T002A019 (2020).
11. K. Vignarooban, X. Xu, A. Arvay, K. Hsu, A. M. Kannan, Heat transfer fluids for concentrating solar power systems–a review. *Applied Energy* **146**, 383-396 (2015).
12. B. D'Aguanno, M. Karthik, A. Grace, A. Floris, Thermostatic properties of nitrate molten salts and their solar and eutectic mixtures. *Scientific Reports* **8**, 1-15 (2018).
13. T. Bauer, C. Odenthal, A. Bonk, Molten salt storage for power generation. *Chemie Ingenieur Technik* **93**, 534-546 (2021).
14. G. Chen, Perspectives on molecular-level understanding of thermophysics of liquids and future research directions. *Journal of Heat Transfer* **144**, 010801 (2022).
15. A. Z. Zhao, M. C. Wingert, J. E. Garay, Frequency-Domain Hot-Wire Measurements of Molten Nitrate Salt Thermal Conductivity. *Journal of Chemical & Engineering Data*, (2020).
16. A. Z. Zhao, J. E. Garay, High temperature liquid thermal conductivity: a review of measurement techniques, theoretical understanding, and energy applications. *Progress in Materials Science*, 101180 (2023).
17. C. D. Chliatzou, M. J. Assael, K. Antoniadis, M. L. Huber, W. A. Wakeham, Reference Correlations for the Thermal Conductivity of 13 Inorganic Molten Salts. *Journal of physical and chemical reference data* **47**, 033104 (2018).

18. D. Lilley, A. K. Menon, S. Kaur, S. Lubner, R. S. Prasher, Phase change materials for thermal energy storage: A perspective on linking phonon physics to performance. *Journal of Applied Physics* **130**, (2021).
19. P. K. Nick Auyeung. (CEP Special Issue on Climate, 2017), vol. 2014.
20. C. Agrafiotis, M. Roeb, M. Schmücker, C. Sattler, Exploitation of thermochemical cycles based on solid oxide redox systems for thermochemical storage of solar heat. Part 1: Testing of cobalt oxide-based powders. *Solar Energy* **102**, 189-211 (2014).
21. C. Agrafiotis, S. Tescari, M. Roeb, M. Schmücker, C. Sattler, Exploitation of thermochemical cycles based on solid oxide redox systems for thermochemical storage of solar heat. Part 3: Cobalt oxide monolithic porous structures as integrated thermochemical reactors/heat exchangers. *Solar Energy* **114**, 459-475 (2015).
22. C. Agrafiotis, M. Roeb, C. Sattler, Hybrid sensible/thermochemical solar energy storage concepts based on porous ceramic structures and redox pair oxides chemistry. *Energy Procedia* **69**, 706-715 (2015).
23. C. Agrafiotis, M. Roeb, C. Sattler, Exploitation of thermochemical cycles based on solid oxide redox systems for thermochemical storage of solar heat. Part 4: Screening of oxides for use in cascaded thermochemical storage concepts. *Solar Energy* **139**, 695-710 (2016).
24. C. Agrafiotis, T. Block, M. Senholdt, S. Tescari, M. Roeb, C. Sattler, Exploitation of thermochemical cycles based on solid oxide redox systems for thermochemical storage of solar heat. Part 6: Testing of Mn-based combined oxides and porous structures. *Solar Energy* **149**, 227-244 (2017).
25. F. Schaube, A. Wörner, R. Tamme, High temperature thermochemical heat storage for concentrated solar power using gas–solid reactions. (2011).
26. C. Ortiz. (MDPI, 2021), vol. 14, pp. 4336.
27. A. H Abedin, M. A Rosen, A critical review of thermochemical energy storage systems. *The open renewable energy journal* **4**, (2011).
28. G. Airò Farulla, M. Cellura, F. Guarino, M. Ferraro, A review of thermochemical energy storage systems for power grid support. *Applied Sciences* **10**, 3142 (2020).
29. B. Wang, Z. Wang, Y. Ma, Y. Liang, Heat transfer enhancement of indirect heat transfer reactors for $Ca(OH)_2/CaO$ thermochemical energy storage system. *Processes* **9**, 1136 (2021).
30. Y. A. Criado, M. Alonso, J. C. Abanades, Kinetics of the $CaO/Ca(OH)_2$ hydration/dehydration reaction for thermochemical energy storage applications. *Industrial & Engineering Chemistry Research* **53**, 12594-12601 (2014).
31. C. Zhao, J. Yan, X. Tian, X. Xue, Y. Zhao, Progress in thermal energy storage technologies for achieving carbon neutrality. *Carbon Neutrality* **2**, 10 (2023).
32. L. F. Cabeza, D. Vérez, G. Zsembinszki, E. Borri, C. Prieto, Key challenges for high temperature thermal energy storage in concrete—first steps towards a novel storage design. *Energies* **15**, 4544 (2022).
33. A. Palacios, L. Cong, M. Navarro, Y. Ding, C. Barreneche, Thermal conductivity measurement techniques for characterizing thermal energy storage materials–A review. *Renewable and Sustainable Energy Reviews* **108**, 32-52 (2019).
34. I. Ermanoski, N. P. Siegel, E. B. Stechel, A new reactor concept for efficient solar-thermochemical fuel production. *Journal of Solar Energy Engineering* **135**, 031002 (2013).

35. J. R. Scheffe, M. Welte, A. Steinfeld, Thermal reduction of ceria within an aerosol reactor for H_2O and CO_2 splitting. *Industrial & Engineering Chemistry Research* **53**, 2175-2182 (2014).
36. O. Hakami, Thermocatalytic and solar thermochemical carbon dioxide utilization to solar fuels and chemicals: A review. *International Journal of Energy Research* **46**, 19929-19960 (2022).
37. X. Li, X. Sun, Q. Song, Z. Yang, H. Wang, Y. Duan, A critical review on integrated system design of solar thermochemical water-splitting cycle for hydrogen production. *International Journal of Hydrogen Energy* **47**, 33619-33642 (2022).
38. V. K. Budama, J. P. R. Duarte, M. Roeb, C. Sattler, Potential of solar thermochemical water-splitting cycles: A review. *Solar Energy* **249**, 353-366 (2023).
39. R. Michalsky, B. J. Parman, V. Amanor-Boadu, P. H. Pfromm, Solar thermochemical production of ammonia from water, air and sunlight: Thermodynamic and economic analyses. *Energy* **42**, 251-260 (2012).
40. Z. Berquist, A. Davoodabadi, A. M. Manon, A. Lenert, TRANSPARENT AEROGEL MATERIALS IN SOLAR THERMAL DEVICES. *Annual Review of Heat Transfer* **25**, (2022).
41. K. McEnaney, L. Weinstein, D. Kraemer, H. Ghasemi, G. Chen, Aerogel-based solar thermal receivers. *Nano Energy* **40**, 180-186 (2017).
42. S. Riahi, M. Liu, R. Jacob, M. Belusko, C. Turchi, F. Bruno, in *AIP Conference Proceedings*. (AIP Publishing, 2020), vol. 2303.
43. T. Shimizu, K. Matsuura, H. Furue, K. Matsuzak, Thermal conductivity of high porosity alumina refractory bricks made by a slurry gelation and foaming method. *Journal of the European ceramic Society* **33**, 3429-3435 (2013).
44. S. Shin, Q. Wang, J. Luo, R. Chen, Advanced materials for high-temperature thermal transport. *Advanced Functional Materials* **30**, 1904815 (2020).
45. C. M. Rost, E. Sachet, T. Borman, A. Moballegh, E. C. Dickey, D. Hou, J. L. Jones, S. Curtarolo, J.-P. Maria, Entropy-stabilized oxides. *Nature communications* **6**, 8485 (2015).
46. A. J. Wright, Q. Wang, S.-T. Ko, K. M. Chung, R. Chen, J. Luo, Size disorder as a descriptor for predicting reduced thermal conductivity in medium-and high-entropy pyrochlore oxides. *Scripta Materialia* **181**, 76-81 (2020).
47. C. S. Turchi, J. Vidal, M. Bauer, Molten salt power towers operating at 600–650 °C: Salt selection and cost benefits. *Solar Energy* **164**, 38-46 (2018).
48. G. Wei, G. Wang, C. Xu, X. Ju, L. Xing, X. Du, Y. Yang, Selection principles and thermophysical properties of high temperature phase change materials for thermal energy storage: A review. *Renewable and Sustainable Energy Reviews* **81**, 1771-1786 (2018).
49. C. K. Ho, B. D. Iverson, Review of high-temperature central receiver designs for concentrating solar power. *Renewable and Sustainable Energy Reviews* **29**, 835-846 (2014).
50. A. Palacios, C. Barreneche, M. Navarro, Y. Ding, Thermal energy storage technologies for concentrated solar power–A review from a materials perspective. *Renewable Energy* **156**, 1244-1265 (2020).
51. M. Anderson, K. Sridharan, D. Morgan, P. Peterson, P. Calderoni, R. Scheele, A. Casekka, B. McNamara, "Heat Transfer Salts for Nuclear Reactor Systems-Chemistry Control, Corrosion Mitigation, and Modeling" (Univ. of Wisconsin, Madison, WI (United States); Univ. of California …, 2015).

52. J. Serp, M. Allibert, O. Beneš, S. Delpech, O. Feynberg, V. Ghetta, D. Heuer, D. Holcomb, V. Ignatiev, J. L. Kloosterman, The molten salt reactor (MSR) in generation IV: overview and perspectives. *Progress in Nuclear Energy* **77**, 308-319 (2014).
53. C. N. A. C. Z. Bahri, W. a. M. Al-Areqi, M. I. F. M. Ruf, A. A. Majid, in *AIP Conference Proceedings*. (AIP Publishing LLC, 2017), vol. 1799, pp. 040008.
54. V. Khokhlov, V. Ignatiev, V. Afonichkin, Evaluating physical properties of molten salt reactor fluoride mixtures. *Journal of fluorine chemistry* **130**, 30-37 (2009).
55. N. Pfleger, T. Bauer, C. Martin, M. Eck, A. Wörner, Thermal energy storage–overview and specific insight into nitrate salts for sensible and latent heat storage. *Beilstein journal of nanotechnology* **6**, 1487-1497 (2015).
56. T. Omotani, Y. Nagasaka, A. Nagashima, Measurement of the thermal conductivity of KNO_3-$NaNO_3$ mixtures using a transient hot-wire method with a liquid metal in a capillary probe. *International Journal of Thermophysics* **3**, 17-26 (1982).
57. X. Zhang, M. Fujii, Simultaneous measurements of the thermal conductivity and thermal diffusivity of molten salts with a transient short-hot-wire method. *International journal of thermophysics* **21**, 71-84 (2000).
58. H. Bloom, A. Doroszkowski, S. Tricklebank, Molten salt mixtures. IX. The thermal conductivities of molten nitrate systems. *Australian Journal of Chemistry* **18**, 1171-1176 (1965).
59. J. McDonald, H. T. Davis, Thermal conductivity of binary mixtures of alkali nitrates. *The Journal of Physical Chemistry* **74**, 725-730 (1970).
60. L. R. White, H. T. Davis, Thermal conductivity of molten alkali nitrates. *The Journal of Chemical Physics* **47**, 5433-5439 (1967).
61. V. D. Golyshev, M. A. Gonik, A standard reference material for thermal conductivity of semitransparent melts. *High Temperatures^ High Pressures* **33**, 639-646 (2001).
62. Y. Grosu, L. González-Fernández, U. Nithiyanantham, A. Faik, Wettability control for correct thermophysical properties determination of molten salts and their nanofluids. *Energies* **12**, 3765 (2019).
63. Y. Zhao, "Molten Chloride Thermophysical Properties, Chemical Optimization, and Purification" (National Renewable Energy Lab.(NREL), Golden, CO (United States), 2020).
64. J. Cape, G. Lehman, Temperature and finite pulse-time effects in the flash method for measuring thermal diffusivity. *Journal of applied physics* **34**, 1909-1913 (1963).
65. A. Philipp, J. F. Eichinger, R. C. Aydin, A. Georgiadis, C. J. Cyron, M. Retsch, The accuracy of laser flash analysis explored by finite element method and numerical fitting. *Heat and Mass Transfer* **56**, 811-823 (2020).
66. Y. Tada, M. Harada, M. Tanigaki, W. Eguchi, Laser flash method for measuring thermal conductivity of liquids—application to low thermal conductivity liquids. *Review of Scientific instruments* **49**, 1305-1314 (1978).
67. R. Coquard, B. Panel, Adaptation of the FLASH method to the measurement of the thermal conductivity of liquids or pasty materials. *International Journal of Thermal Sciences* **48**, 747-760 (2009).
68. A. Z. Zhao, M. C. Wingert, R. Chen, J. E. Garay, Phonon gas model for thermal conductivity of dense, strongly interacting liquids. *Journal of Applied Physics* **129**, 235101 (2021).

69. J. Zeng, K. M. Chung, Q. Wang, X. Wang, Y. Pei, P. Li, R. Chen, Measurement of High-temperature Thermophysical Properties of Bulk and Coatings Using Modulated Photothermal Radiometry. *International Journal of Heat and Mass Transfer* **170**, 120989 (2021).
70. J. Zeng, K. M. Chung, S. R. Adapa, T. Feng, R. Chen, In-situ thermal transport measurement of flowing fluid using modulated photothermal radiometry. *International Journal of Heat and Mass Transfer* **180**, 121767 (2021).
71. M. Assael, K. Gialou, K. Kakosimos, I. Metaxa, Thermal conductivity of reference solid materials. *International Journal of Thermophysics* **25**, 397-408 (2004).
72. M. Assael, S. Botsios, K. Gialou, I. Metaxa, Thermal conductivity of polymethyl methacrylate (PMMA) and borosilicate crown glass BK7. *International Journal of Thermophysics* **26**, 1595-1605 (2005).
73. M. N. Ozisik, *Inverse heat transfer: fundamentals and applications* (Routledge, 2018).
74. George W. Woodruff School of Mechanical Engineering, "Thermophysical Properties Database of Gen3 CSP Materials" (George W. Woodruff School of Mechanical Engineering, 2018, https://gen3csp.gatech.edu/)
75. X. Wang, J. D. Rincon, P. Li, Y. Zhao, J. Vidal, Thermophysical properties experimentally tested for NaCl-KCl-$MgCl_2$ eutectic molten salt as a next-generation high-temperature heat transfer fluids in concentrated solar power systems. *Journal of Solar Energy Engineering* **143**, 041005 (2021).
76. J. Eftekhar, A. Haji-Sheikh, D. Lou, Heat transfer enhancement in a paraffin wax thermal storage system. (1984).
77. A. El-Sharkawy, M. Dessouky, Measurement of thermal conductivity, heat capacity, and thermal diffusivity of sulfur and selenium in the liquid state. *International journal of thermophysics* **4**, 115-125 (1983).
78. B. Cheng, B. Lane, J. Whiting, K. Chou, A combined experimental-numerical method to evaluate powder thermal properties in laser powder bed fusion. *Journal of manufacturing science and engineering* **140**, 111008 (2018).
79. A. F. Mills, C. Coimbra, *Basic heat transfer* (Temporal Publishing, LLC, 2015).
80. A. Agarwal, R. Sarviya, Characterization of commercial grade paraffin wax as latent heat storage material for solar dryers. *Materials Today: Proceedings* **4**, 779-789 (2017).
81. V. Saydam, X. Duan, Dispersing different nanoparticles in paraffin wax as enhanced phase change materials. *Journal of Thermal Analysis and Calorimetry* **135**, 1135-1144 (2019).
82. A. Haji-Sheikh, J. Eftekhar, D. Lou, in *3rd Joint Thermophysics, Fluids, Plasma and Heat Transfer Conference*. (1982), pp. 846.
83. M.-C. Chang, M.-S. Jhon, Viscosity and thermodynamic properties of liquid sulfur. *Bulletin of the Korean Chemical Society* **3**, 133-139 (1982).
84. A. Eisenberg, The viscosity of liquid sulfur. A mechanistic reinterpretation. *Macromolecules* **2**, 44-48 (1969).
85. E. Lemmon, M. McLinden, D. Friend, P. LINSTROM, W. MALLARD. (Gaithersburg: NIST, 2011).
86. Y. Jin, J. Cheng, X. An, T. Su, P. Zhang, Z. Li, Accurate viscosity measurement of nitrates/nitrites salts for concentrated solar power. *Solar Energy* **137**, 385-392 (2016).

87. S. S. Parker, A. Long, C. Lhermitte, S. Vogel, M. Monreal, J. Jackson, Thermophysical properties of liquid chlorides from 600 to 1600 K: Melt point, enthalpy of fusion, and volumetric expansion. *Journal of Molecular Liquids* **346**, 118147 (2022).
88. M. O'neill, Measurement of Specific Heat Functions by Differential Scanning Calorimetry. *Analytical chemistry* **38**, 1331-1336 (1966).
89. J. Del Rincon, Experimental Measurements for Melting Point, Heat of Fusion and Heat Capacity of Several Eutectic Molten Salts by NaCl-KCl-$MgCl_2$. (2020).
90. A. Sugawara, Thermal conductivity of sulfur accompanying crystal transition and phase change. *Journal of Applied Physics* **36**, 2375-2377 (1965).
91. G. W. C. Kaye, W. Higgins, The thermal conductivity of solid and liquid sulphur. *Proceedings of the Royal Society of London. Series A, Containing Papers of a Mathematical and Physical Character* **122**, 633-646 (1929).
92. M. Wingert, A. Zhao, Y. Kodera, S. Obrey, J. Garay, Frequency-domain hot-wire sensor and 3D model for thermal conductivity measurements of reactive and corrosive materials at high temperatures. *Review of Scientific Instruments* **91**, 054904 (2020).
93. C. W. Bale, E. Bélisle, P. Chartrand, S. A. Decterov, G. Eriksson, A. Gheribi, K. Hack, I.-H. Jung, Y.-B. Kang, J. Melançon, Reprint of: FactSage thermochemical software and databases, 2010–2016. *Calphad* **55**, 1-19 (2016).
94. R. Tufeu, J. P. Petitet, L. Denielou, B. Le Neindre, Experimental determination of the thermal conductivity of molten pure salts and salt mixtures. *International Journal of Thermophysics* **6**, 315 (1985).
95. Y. Xiong, Z. Wang, M. Sun, Y. Wu, P. Xu, X. Qian, C. Li, Y. Ding, C. Ma, Enhanced thermal energy storage of nitrate salts by silica nanoparticles for concentrating solar power. *International Journal of Energy Research* **45**, 5248-5262 (2021).
96. S. Kitade, Y. Kobayashi, Y. Nagasaka, A. Nagashima, Measurement of the thermal conductivity of molten KNO_3 and $NaNO_3$ by the transient hot-wire method with ceramic-coated probes. *High Temperatures-High Pressures* **21**, 219-224 (1989).
97. T. Asahina, M. Kosaka, K. Tajiri, Thermal diffusivity measurement of molten nitrates by pulse-heated flat plate method. *Kagaku Kogaku Ronbunshu* **14**, 616-621 (1988).
98. O. Odawara, I. Okada, K. Kawamura, Measurement of the thermal diffusivity of HTS (a mixture of molten sodium nitrate-potassium nitrate-sodium nitrite; 7-44-49 mole%) by optical interferometry. *Journal of Chemical and Engineering Data* **22**, 222-225 (1977).
99. A. J. McGaughey, J. M. Larkin, Predicting phonon properties from equilibrium molecular dynamics simulations. *Annual review of heat transfer* **17**, (2014).
100. A. Anagnostopoulos, A. Alexiadis, Y. Ding, Molecular dynamics simulation of solar salt ($NaNO_3$-KNO_3) mixtures. *Solar Energy Materials and Solar Cells* **200**, 109897 (2019).
101. C. I. Maxwell, M. Saoudi, J. Pencer, Development of a Polarizable Interatomic Potential for Molten Lithium, Sodium, and Potassium Nitrate. *The Journal of Physical Chemistry B* **124**, 4751-4761 (2020).
102. Y. Wu, J. Li, M. Wang, H. Wang, Y. Zhong, Y. Zhao, M. Wei, Y. Li, Solar salt doped by MWCNTs as a promising high thermal conductivity material for CSP. *RSC advances* **8**, 19251-19260 (2018).
103. X. Wei, Y. Yin, B. Qin, J. Ding, J. Lu, Thermal conductivity improvement of liquid Nitrate and Carbonate salts doped with MgO particles. *Energy Procedia* **142**, 407-412 (2017).

104. R. Serrano-López, J. Fradera, S. Cuesta-López, Molten salts database for energy applications. *Chemical Engineering and Processing: Process Intensification* **73**, 87-102 (2013).
105. R. Tufeu, J. Petitet, L. Denielou, B. Le Neindre, Experimental determination of the thermal conductivity of molten pure salts and salt mixtures. *International journal of thermophysics* **6**, 315-330 (1985).
106. R. DiGuilio, A. S. Teja, A rough hard-sphere model for the thermal conductivity of molten salts. *International journal of thermophysics* **13**, 855-871 (1992).
107. A. E. Gheribi, J. A. Torres, P. Chartrand, Recommended values for the thermal conductivity of molten salts between the melting and boiling points. *Solar energy materials and solar cells* **126**, 11-25 (2014).
108. X.-H. An, J.-H. Cheng, H.-Q. Yin, L.-D. Xie, P. Zhang, Thermal conductivity of high temperature fluoride molten salt determined by laser flash technique. *International Journal of Heat and Mass Transfer* **90**, 872-877 (2015).
109. P. Baumli, G. Kaptay, Wettability of carbon surfaces by pure molten alkali chlorides and their penetration into a porous graphite substrate. *Materials Science and Engineering: A* **495**, 192-196 (2008).
110. T. Bauer, W.-D. Steinmann, D. Laing, R. Tamme, Thermal energy storage materials and systems. *Annual Review of Heat Transfer* **15**, (2012).
111. L. A. Weinstein, J. Loomis, B. Bhatia, D. M. Bierman, E. N. Wang, G. Chen, Concentrating solar power. *Chemical Reviews* **115**, 12797-12838 (2015).
112. R. Merchán, M. Santos, A. Medina, A. C. Hernández, High temperature central tower plants for concentrated solar power: 2021 overview. *Renewable and Sustainable Energy Reviews* **155**, 111828 (2022).
113. Y. Tian, C.-Y. Zhao, A review of solar collectors and thermal energy storage in solar thermal applications. *Applied energy* **104**, 538-553 (2013).
114. T. Bauer, N. Pfleger, D. Laing, W.-D. Steinmann, M. Eck, S. Kaesche, "High-temperature molten salts for solar power application" in *Molten salts chemistry* (Elsevier, 2013), pp. 415-438.
115. Q. Wang, C. Wu, X. Wang, S. Sun, D. Cui, S. Pan, H. Sheng, A review of eutectic salts as phase change energy storage materials in the context of concentrated solar power. *International Journal of Heat and Mass Transfer* **205**, 123904 (2023).
116. Y. Zhao, J. Vidal, Potential scalability of a cost-effective purification method for $MgCl_2$-Containing salts for next-generation concentrating solar power technologies. *Solar Energy Materials and Solar Cells* **215**, 110663 (2020).
117. P. Li, E. Molina, K. Wang, X. Xu, G. Dehghani, A. Kohli, Q. Hao, M. H. Kassaee, S. M. Jeter, A. S. Teja, Thermal and transport properties of NaCl–KCl–$ZnCl_2$ eutectic salts for new generation high-temperature heat-transfer fluids. *Journal of Solar Energy Engineering* **138**, (2016).
118. D. Langstaff, M. Gunn, G. N. Greaves, A. Marsing, F. Kargl, Aerodynamic levitator furnace for measuring thermophysical properties of refractory liquids. *Review of Scientific Instruments* **84**, 124901 (2013).
119. J. Hong, D. Kim, Measuring the thermal conductivity of flowing liquid samples using the three omega method. *Journal of Heat Transfer* **134**, 094502 (2012).

120. M. Mehrvand, S. A. Putnam, Probing the local heat transfer coefficient of water-cooled microchannels using time-domain thermoreflectance. *Journal of Heat Transfer* **139**, (2017).
121. Y. Zhang, X. Wang, Q. Hu, P. Li, Q. Liu, B. Xu, Experimental Study of Eutectic Molten Salts NaCl/KCl/$ZnCl_2$ Heat Transfer Inside a Smooth Tube for High-Temperature Application. *Journal of Solar Energy Engineering* **144**, 044501 (2022).
122. D. Ting, *Thermofluids: From Nature to Engineering* (Academic Press, 2022).
123. Y. Zeng, G. Cui, W. Wu, C. Xu, J. Huang, J. Wang, Z. Yang, Numerical Simulation Study on Flow Heat Transfer and Stress Distribution of Shell-and-Tube Superheater in Molten Salt Solar Thermal Power Station. *Processes* **10**, 1003 (2022).
124. O. Arora, B. Lancaster, S. R. Yang, R. Vaghetto, Y. Hassan, Advanced flow and temperature measurements in a forced convection molten salt test loop. *Annals of Nuclear Energy* **159**, 108269 (2021).
125. P. Sabharwall, M. Ebner, M. Sohal, P. Sharpe, "Molten Salts for High Temperature Reactors: University of Wisconsin Molten Salt Corrosion and Flow Loop Experiments--Issues Identified and Path Forward" (Idaho National Lab.(INL), Idaho Falls, ID (United States), 2010).
126. D. D. Gill, W. J. Kolb, R. J. Briggs, "An evaluation of pressure and flow measurement in the Molten Salt Test Loop (MSTL) system" (Sandia National Lab.(SNL-NM), Albuquerque, NM (United States), 2013).
127. H. Sun, J. Wang, Z. Li, P. Zhang, X. Su, Corrosion behavior of 316SS and Ni-based alloys in a ternary NaCl-KCl-$MgCl_2$ molten salt. *Solar Energy* **171**, 320-329 (2018).
128. S. Hasnain, Review on sustainable thermal energy storage technologies, Part I: heat storage materials and techniques. *Energy conversion and management* **39**, 1127-1138 (1998).
129. T. P. Farr, N. P. Nguyen, H. E. Bush, A. Ambrosini, P. G. Loutzenhiser, An A-and B-site substitutional study of $SrFeO_{3-\delta}$ perovskites for solar thermochemical air separation. *Materials* **13**, 5123 (2020).
130. H. E. Bush, N. P. Nguyen, T. Farr, P. G. Loutzenhiser, A. Ambrosini, Air separation via a two-step solar thermochemical cycle based on $(Ba, La)_xSr_{1-x}FeO_{3-\delta}$: Thermodynamic analysis. *Solid State Ionics* **368**, 115692 (2021).
131. S. Zhai, J. Rojas, N. Ahlborg, K. Lim, C. H. M. Cheng, C. Xie, M. F. Toney, I.-H. Jung, W. C. Chueh, A. Majumdar, High-capacity thermochemical CO_2 dissociation using iron-poor ferrites. *Energy & Environmental Science* **13**, 592-600 (2020).
132. Y. Gao, Y. Mao, Z. Song, X. Zhao, J. Sun, W. Wang, G. Chen, S. Chen, Efficient generation of hydrogen by two-step thermochemical cycles: Successive thermal reduction and water splitting reactions using equal-power microwave irradiation and a high entropy material. *Applied Energy* **279**, 115777 (2020).
133. X. Qian, J. He, E. Mastronardo, B. Baldassarri, C. Wolverton, S. M. Haile, Favorable redox thermodynamics of $SrTi_{0.5}Mn_{0.5}O_{3-\delta}$ in solar thermochemical water splitting. *Chemistry of Materials* **32**, 9335-9346 (2020).
134. T. Kodama, High-temperature solar chemistry for converting solar heat to chemical fuels. *Progress in energy and combustion science* **29**, 567-597 (2003).
135. T. Kodama, Y. Nakamuro, T. Mizuno, A two-step thermochemical water splitting by iron-oxide on stabilized zirconia. (2006).

136. W. C. Chueh, C. Falter, M. Abbott, D. Scipio, P. Furler, S. M. Haile, A. Steinfeld, High-flux solar-driven thermochemical dissociation of CO_2 and H_2O using nonstoichiometric ceria. *Science* **330**, 1797-1801 (2010).
137. A. Solé, I. Martorell, L. F. Cabeza, State of the art on gas–solid thermochemical energy storage systems and reactors for building applications. *Renewable and Sustainable Energy Reviews* **47**, 386-398 (2015).
138. E. Alonso, A. Gallo, C. Pérez-Rábago, E. Fuentealba, in *AIP Conference Proceedings*. (AIP Publishing, 2016), vol. 1734.
139. E. Alonso, C. Pérez-Rábago, J. Licurgo, E. Fuentealba, C. A. Estrada, First experimental studies of solar redox reactions of copper oxides for thermochemical energy storage. *Solar Energy* **115**, 297-305 (2015).
140. J. Liu, J. Baeyens, Y. Deng, X. Wang, H. Zhang, High temperature Mn_2O_3/Mn_3O_4 and Co_3O_4/CoO systems for thermo-chemical energy storage. *Journal of environmental management* **267**, 110582 (2020).
141. A. Solé, X. Fontanet, C. Barreneche, A. I. Fernández, I. Martorell, L. F. Cabeza, Requirements to consider when choosing a thermochemical material for solar energy storage. *Solar energy* **97**, 398-404 (2013).
142. J. E. Bird, T. D. Humphries, M. Paskevicius, L. Poupin, C. E. Buckley, Thermal properties of thermochemical heat storage materials. *Physical Chemistry Chemical Physics* **22**, 4617-4625 (2020).
143. A. F. Lele, K. E. N'Tsoukpoe, T. Osterland, F. Kuznik, W. K. Ruck, Thermal conductivity measurement of thermochemical storage materials. *Applied Thermal Engineering* **89**, 916-926 (2015).
144. K. Walayat, J. Duesmann, T. Derks, A. Houshang Mahmoudi, R. Cuypers, M. Shahi, Experimental and numerical investigations for effective thermal conductivity in packed beds of thermochemical energy storage materials. *Applied thermal engineering* **193**, 117006 (2021).
145. M. Hamidi, V. M. Wheeler, P. Kreider, K. Catchpole, A. W. Weimer, Effective thermal conductivity of a bed packed with granular iron–manganese oxide for thermochemical energy storage. *Chemical Engineering Science* **207**, 490-494 (2019).
146. J. Zeng, K. M. Chung, X. Zhang, T. Feng, S. Adapa, R. Chen, Characterization and Understanding of Thermal Transport in Stationary and Moving Particle Beds for Concentrating Solar Power. *Annual Review of Heat Transfer* **25**, (2022).
147. Q. Zheng, S. Kaur, C. Dames, R. S. Prasher, Analysis and improvement of the hot disk transient plane source method for low thermal conductivity materials. *International Journal of Heat and Mass Transfer* **151**, 119331 (2020).
148. S. Yamanaka, K. Kurosaki, T. Maekawa, T. Matsuda, S.-i. Kobayashi, M. Uno, Thermochemical and thermophysical properties of alkaline-earth perovskites. *Journal of Nuclear Materials* **344**, 61-66 (2005).
149. K. M. Chung, T. Feng, J. Zeng, S. R. Adapa, X. Zhang, A. Z. Zhao, Y. Zhang, P. Li, Y. Zhao, J. E. Garay, Thermal conductivity measurement using modulated photothermal radiometry for nitrate and chloride molten salts. *International Journal of Heat and Mass Transfer* **217**, 124652 (2023).
150. K. M. Chung, Y. Zhang, J. Zeng, F. Haddad, S. Adapa, T. Feng, P. Li, R. Chen, In-situ thermophysical measurement of flowing molten chloride salt using modulated photothermal radiometry. *Solar Energy* **265**, 112124 (2023).

151. H. U. Rammelberg, T. Schmidt, W. Ruck, Hydration and dehydration of salt hydrates and hydroxides for thermal energy storage-kinetics and energy release. *Energy procedia* **30**, 362-369 (2012).
152. N. P. Nguyen, T. P. Farr, H. E. Bush, A. Ambrosini, P. G. Loutzenhiser, Air separation via two-step solar thermochemical cycles based on $SrFeO_{3-\delta}$ and $(Ba, La)_{0.15}Sr_{0.85}FeO_{3-\delta}$ perovskite reduction/oxidation reactions to produce N 2: rate limiting mechanism (s) determination. *Physical Chemistry Chemical Physics* **23**, 19280-19288 (2021).
153. C. K. Ho, A. R. Mahoney, A. Ambrosini, M. Bencomo, A. Hall, T. N. Lambert, Characterization of Pyromark 2500 paint for high-temperature solar receivers. *Journal of Solar Energy Engineering* **136**, 014502 (2014).
154. M. W. Chase, N. I. S. Organization, *NIST-JANAF thermochemical tables* (American Chemical Society Washington, DC, 1998), vol. 9.
155. W. Wentworth, E. Chen, Simple thermal decomposition reactions for storage of solar thermal energy. *Solar Energy* **18**, 205-214 (1976).
156. A. Maruyama, R. Kurosawa, J. Ryu, Effect of lithium compound addition on the dehydration and hydration of calcium hydroxide as a chemical heat storage material. *ACS omega* **5**, 9820-9829 (2020).
157. S. Breuer, M. Schwotzer, S. Speziale, F. Schilling, Thermoelastic properties of synthetic single crystal portlandite $Ca(OH)_2$-Temperature-dependent thermal diffusivity with derived thermal conductivity and elastic constants at ambient conditions. *Cement and Concrete Research* **137**, 106199 (2020).
158. Y. Ma, S. Yang, K. He, C. Lu, First principles study of the lattice thermal conductivity of alkaline earth oxides. *Computational Materials Science* **210**, 111446 (2022).
159. J. Leitner, P. Voňka, D. Sedmidubský, P. Svoboda, Application of Neumann–Kopp rule for the estimation of heat capacity of mixed oxides. *Thermochimica Acta* **497**, 7-13 (2010).
160. I. Barin, G. Platzki, *Thermochemical data of pure substances* (Wiley Online Library, 1989), vol. 304.
161. E. B. Rubin, Y. Chen, R. Chen, Optical properties and thermal stability of Cu spinel oxide nanoparticle solar absorber coatings. *Solar Energy Materials and Solar Cells* **195**, 81-88 (2019).
162. L. D. Jaffe, Solar tests of aperture plate materials for solar thermal dish collectors. (1984).
163. M. Petrollese, M. Cascetta, V. Tola, D. Cocco, G. Cau, Pumped thermal energy storage systems integrated with a concentrating solar power section: Conceptual design and performance evaluation. *Energy* **247**, 123516 (2022).
164. F. Nie, F. Bai, Z. Wang, X. Li, R. Yang, Solid particle solar receivers in the next-generation concentrated solar power plant. *EcoMat*, e12207 (2022).
165. A. Calderón, A. Palacios, C. Barreneche, M. Segarra, C. Prieto, A. Rodriguez-Sanchez, A. I. Fernández, High temperature systems using solid particles as TES and HTF material: a review. *Applied Energy* **213**, 100-111 (2018).
166. C. Parrado, A. Girard, F. Simon, E. Fuentealba, 2050 LCOE (Levelized Cost of Energy) projection for a hybrid PV (photovoltaic)-CSP (concentrated solar power) plant in the Atacama Desert, Chile. *Energy* **94**, 422-430 (2016).

167. A. Boretti, S. Castelletto, Cost and performance of CSP and PV plants of capacity above 100 MW operating in the United States of America. *Renewable Energy Focus* **39**, 90-98 (2021).
168. P. Falcone, J. Noring, J. Hruby, "Assessment of a solid particle receiver for a high temperature solar central receiver system" (Sandia National Lab.(SNL-CA), Livermore, CA (United States), 1985).
169. C. K. Ho, K. J. Albrecht, L. Yue, B. Mills, J. Sment, J. Christian, M. Carlson, Overview and Design Basis for the Gen 3 Particle Pilot Plant (G3P3). *Aip Conf Proc* **2303**, (2020).
170. Solar Energy Technologies Office, (SETO), "Generation 3 Concentrating Solar Power Systems (Gen3 CSP) Phase 3 Project Selection" (SETO, 2021, https://www.energy.gov/eere/solar/generation-3-concentrating-solar-power-systems-gen3-csp-phase-3-project-selection)
171. T. Baumann, S. Zunft, Properties of granular materials as heat transfer and storage medium in CSP application. *Solar Energy Materials and Solar Cells* **143**, 38-47 (2015).
172. R. Tiskatine, R. Oaddi, R. A. El Cadi, A. Bazgaou, L. Bouirden, A. Aharoune, A. Ihlal, Suitability and characteristics of rocks for sensible heat storage in CSP plants. *Solar Energy Materials and Solar Cells* **169**, 245-257 (2017).
173. F. Nie, Z. Cui, F. Bai, Z. Wang, Properties of solid particles as heat transfer fluid in a gravity driven moving bed solar receiver. *Solar Energy Materials and Solar Cells* **200**, 110007 (2019).
174. A. Calderón, C. Barreneche, A. I. Fernández, M. Segarra, Thermal cycling test of solid particles to be used in concentrating solar power plants. *Solar Energy Materials and Solar Cells* **222**, 110936 (2021).
175. L. Sang, K. Wang, R. Zhang, Y. Wang, Y. Wu, Effective thermal conductivity and thermal cycling stability of solid particles for sCO_2 CSP applications. *Solar Energy Materials and Solar Cells* **242**, 111764 (2022).
176. M. Díaz-Heras, A. Calderón, M. Navarro, J. Almendros-Ibáñez, A. I. Fernández, C. Barreneche, Characterization and testing of solid particles to be used in CSP plants: Aging and fluidization tests. *Solar Energy Materials and Solar Cells* **219**, 110793 (2021).
177. O. A. Radwan, J. D. Humphrey, A. S. Hakeem, M. Zeama, Evaluating properties of Arabian desert sands for use in solar thermal technologies. *Solar Energy Materials and Solar Cells* **231**, 111335 (2021).
178. K. J. Albrecht, C. K. Ho, in *AIP Conference Proceedings*. (AIP Publishing LLC, 2018), vol. 2033, pp. 040003.
179. N. Siegel, M. Gross, C. Ho, T. Phan, J. Yuan, Physical properties of solid particle thermal energy storage media for concentrating solar power applications. *Energy Procedia* **49**, 1015-1023 (2014).
180. N. P. Siegel, M. D. Gross, R. Coury, The development of direct absorption and storage media for falling particle solar central receivers. *Journal of Solar Energy Engineering* **137**, (2015).
181. K. M. Chung, J. Zeng, S. R. Adapa, T. Feng, M. V. Bagepalli, P. G. Loutzenhiser, K. J. Albrecht, C. K. Ho, R. Chen, Measurement and analysis of thermal conductivity of ceramic particle beds for solar thermal energy storage. *Solar Energy Materials and Solar Cells* **230**, 111271 (2021).

182. P. Devanport, Z. W. Ma, W. Nationa, J. Schirck, A. Morris, M. Lambert, Thermal stability of silica for application in thermal energy storage. *AIP Conference Proceedings* **2445**, 160003 (2022).
183. A. Palacios, A. Calderon, C. Barreneche, J. Bertomeu, M. Segarra, A. I. Fernandez, Study on solar absorptance and thermal stability of solid particles materials used as TES at high temperature on different aging stages for CSP applications. *Sol Energ Mat Sol C* **201**, (2019).
184. N. Siegel, M. Gross, C. Ho, T. Phan, J. Yuan, Physical properties of solid particle thermal energy storage media for concentrating solar power applications. *Enrgy Proced* **49**, 1015-1023 (2014).
185. N. P. Siegel, M. D. Gross, R. Coury, The Development of Direct Absorption and Storage Media for Falling Particle Solar Central Receivers. *J Sol Energ-T Asme* **137**, (2015).
186. C. Chen, C. Yang, D. Ranjan, P. G. Loutzenhiser, Z. M. Zhang, Spectral radiative properties of ceramic particles for concentrated solar thermal energy storage applications. *International Journal of Thermophysics* **41**, 1-25 (2020).
187. A. Gimeno-Furio, L. Hernandez, R. Martinez-Cuenca, R. Mondragón, A. Vela, L. Cabedo, C. Barreneche, M. Iacob, New coloured coatings to enhance silica sand absorbance for direct particle solar receiver applications. *Renewable Energy* **152**, 1-8 (2020).
188. K. J. Albrecht, M. L. Bauer, C. K. Ho, Parametric Analysis of Particle Csp System Performance and Cost to Intrinsic Particle Properties and Operating Conditions. *Proceedings of the Asme 13th International Conference on Energy Sustainability, 2019*, (2019).
189. Solar Energy Technologies Office, (SETO), "2030 Solar Cost Targets" (SETO, 2021, https://www.energy.gov/eere/solar/articles/2030-solar-cost-targets)
190. B. Gobereit, L. Amsbeck, C. Happich, M. Schmücker, Assessment and improvement of optical properties of particles for solid particle receiver. *Solar Energy* **199**, 844-851 (2020).
191. G. Alkan, P. Mechnich, J. Pernpeintner, Improved Performance of Ceramic Solar Absorber Particles Coated with Black Oxide Pigment Deposited by Resonant Acoustic Mixing and Reaction Sintering. *Coatings* **12**, (2022).
192. E. B. Rubin, Y. M. Chen, R. K. Chen, Optical properties and thermal stability of Cu spinel oxide nanoparticle solar absorber coatings. *Solar Energy Materials and Solar Cells* **195**, 81-88 (2019).
193. A. Standard, G173-03 (reapproved 2012), standard tables for reference solar spectral irradiances: Direct normal and hemispherical on 37 tilted surface. *West Conshohocken, PA: ASTM International*, (2012).
194. J. Zeng, K. M. Chung, X. Zhang, S. Adapa, T. Feng, Y. Pei, R. Chen, Thermal conductivity modeling of monodispersed microspheres using discrete element method. *Journal of Applied Physics* **130**, 165104 (2021).
195. M. Akaogi, H. Yusa, K. Shiraishi, T. Suzuki, Thermodynamic properties of α-quartz, coesite, and stishovite and equilibrium phase relations at high pressures and high temperatures. *Journal of Geophysical Research: Solid Earth* **100**, 22337-22347 (1995).
196. Transmetra. (Transmetra Flurlingen, Switzerland, 2012).

197. J. M. Mayer, J. A. Abraham, B. Kinzer, R. B. Chandran, Temperature-Dependent Diffuse Reflectance Measurements of Ceramic Powders in the Near-and Mid-Infrared Spectra. *arXiv preprint arXiv:2204.06640*, (2022).
198. W. d. van Antwerpen, C. Du Toit, P. Rousseau, A review of correlations to model the packing structure and effective thermal conductivity in packed beds of mono-sized spherical particles. *Nuclear Engineering and design* **240**, 1803-1818 (2010).
199. K. J. Albrecht, C. K. Ho, Design and operating considerations for a shell-and-plate, moving packed-bed, particle-to-sCO_2 heat exchanger. *Solar Energy* **178**, 331-340 (2019).
200. S. Trevisan, W. Wang, B. Laumert, Coatings utilization to modify the effective properties of high temperature packed bed thermal energy storage. *Applied Thermal Engineering* **185**, 116414 (2021).
201. W. Villasmil, L. J. Fischer, J. Worlitschek, A review and evaluation of thermal insulation materials and methods for thermal energy storage systems. *Renewable and Sustainable Energy Reviews* **103**, 71-84 (2019).
202. D. R. Clarke, M. Oechsner, N. P. Padture, Thermal-barrier coatings for more efficient gas-turbine engines. *MRS bulletin* **37**, 891-898 (2012).
203. V. Gupta, C. Deb, Envelope design for low-energy buildings in the tropics: A review. *Renewable and Sustainable Energy Reviews* **186**, 113650 (2023).
204. K. D. Chandhran, S. Elavenil, A comprehensive state-of-the-art review of sustainable thermal insulation system used in external walls for reduction in energy consumption in buildings. *International Journal of Green Energy* **20**, 895-913 (2023).
205. Z. L. Yu, N. Yang, V. Apostolopoulou-Kalkavoura, B. Qin, Z. Y. Ma, W. Y. Xing, C. Qiao, L. Bergström, M. Antonietti, S. H. Yu, Fire-retardant and thermally insulating phenolic-silica aerogels. *Angewandte Chemie International Edition* **57**, 4538-4542 (2018).
206. P. Singh, N. Q. Minh, Solid oxide fuel cells: technology status. *International Journal of Applied Ceramic Technology* **1**, 5-15 (2004).
207. X. Feng, D. Ren, X. He, M. Ouyang, Mitigating thermal runaway of lithium-ion batteries. *Joule* **4**, 743-770 (2020).
208. P. Nambisan, H. Manjunatha, P. Ravadi, H. P. Reddy, G. Bharath, M. A. Kulkarni, S. Sundaram, Characterization of commercial thermal barrier materials to prevent thermal runaway propagation in large format lithium-ion cells. *Journal of Energy Storage* **74**, 109414 (2023).
209. J. Niu, S. Deng, X. Gao, H. Niu, Y. Fang, Z. Zhang, Experimental study on low thermal conductive and flame retardant phase change composite material for mitigating battery thermal runaway propagation. *Journal of Energy Storage* **47**, 103557 (2022).
210. L. Li, C. Xu, R. Chang, C. Yang, C. Jia, L. Wang, J. Song, Z. Li, F. Zhang, B. Fang, Thermal-responsive, super-strong, ultrathin firewalls for quenching thermal runaway in high-energy battery modules. *Energy Storage Materials* **40**, 329-336 (2021).
211. Z. Yu, Y. Wan, Y. Qin, J.-P. Guan, X.-W. Cheng, X. Wang, S. Ouyang, X. Qu, Z. Zhu, J. Wang, High fire safety thermal protective composite aerogel with efficient thermal insulation and reversible fire warning performance for firefighting clothing. *Chemical Engineering Journal* **477**, 147187 (2023).
212. O. Uyanna, H. Najafi, Thermal protection systems for space vehicles: A review on technology development, current challenges and future prospects. *Acta Astronautica* **176**, 341-356 (2020).

213. C. Ercol, E. Congdon, K. Balakrishnan, G. A. Holtzman. (51st International Conference on Environmental Systems, 2022).
214. K. Schlichting, N. Padture, P. Klemens, Thermal conductivity of dense and porous yttria-stabilized zirconia. *Journal of materials science* **36**, 3003-3010 (2001).
215. J. Wu, X. Wei, N. P. Padture, P. G. Klemens, M. Gell, E. García, P. Miranzo, M. I. Osendi, Low-thermal-conductivity rare-earth zirconates for potential thermal-barrier-coating applications. *Journal of the American Ceramic Society* **85**, 3031-3035 (2002).
216. X. Xu, Q. Zhang, M. Hao, Y. Hu, Z. Lin, L. Peng, T. Wang, X. Ren, C. Wang, Z. Zhao, C. Wan, H. Fei, L. Wang, J. Zhu, H. Sun, W. Chen, T. Du, B. Deng, G. J. Cheng, I. Shakir, C. Dames, T. S. Fisher, X. Zhang, H. Li, Y. Huang, X. Duan, Double-negative-index ceramic aerogels for thermal superinsulation. *Science* **363**, 723-727 (2019).
217. L. Wang, J. Feng, Y. Jiang, L. Li, J. Feng, Thermal conductivity of polyvinylpolymethylsiloxane aerogels with high specific surface area. *RSC advances* **9**, 7833-7841 (2019).
218. D. Shi, Y. Sun, J. Feng, X. Yang, S. Han, C. Mi, Y. Jiang, H. Qi, Experimental investigation on high temperature anisotropic compression properties of ceramic-fiber-reinforced SiO2 aerogel. *Materials Science and Engineering: A* **585**, 25-31 (2013).
219. C. Zhu, T. Y.-J. Han, E. B. Duoss, A. M. Golobic, J. D. Kuntz, C. M. Spadaccini, M. A. Worsley, Highly compressible 3D periodic graphene aerogel microlattices. *Nature communications* **6**, 6962 (2015).
220. L. Su, H. Wang, M. Niu, X. Fan, M. Ma, Z. Shi, S.-W. Guo, Ultralight, recoverable, and high-temperature-resistant SiC nanowire aerogel. *ACS nano* **12**, 3103-3111 (2018).
221. Y. Si, J. Yu, X. Tang, J. Ge, B. Ding, Ultralight nanofibre-assembled cellular aerogels with superelasticity and multifunctionality. *Nature communications* **5**, 5802 (2014).
222. G. Zu, J. Shen, L. Zou, W. Wang, Y. Lian, Z. Zhang, A. Du, Nanoengineering super heat-resistant, strong alumina aerogels. *Chemistry of materials* **25**, 4757-4764 (2013).
223. Y. Si, X. Wang, L. Dou, J. Yu, B. Ding, Ultralight and fire-resistant ceramic nanofibrous aerogels with temperature-invariant superelasticity. *Science advances* **4**, eaas8925 (2018).
224. J. Fricke, X. Lu, P. Wang, D. Büttner, U. Heinemann, Optimization of monolithic silica aerogel insulants. *International journal of heat and mass transfer* **35**, 2305-2309 (1992).
225. A. Bisson, A. Rigacci, D. Lecomte, P. Achard, Effective thermal conductivity of divided silica xerogel beds. *Journal of non-crystalline solids* **350**, 379-384 (2004).
226. J. Wang, J. Kuhn, X. Lu, Monolithic silica aerogel insulation doped with TiO2 powder and ceramic fibers. *Journal of non-crystalline solids* **186**, 296-300 (1995).
227. Y. Lu, X. Li, X. Yin, H. D. Utomo, N. F. Tao, H. Huang, Silica aerogel as super thermal and acoustic insulation materials. *Journal of Environmental Protection* **9**, 295-308 (2018).
228. K. Wu, Q. Zhou, J. Cao, Z. Qian, B. Niu, D. Long, Ultrahigh-strength carbon aerogels for high temperature thermal insulation. *Journal of Colloid and Interface Science* **609**, 667-675 (2022).
229. Y. Chen, O. Ola, G. Liu, L. Han, M. Z. Hussain, K. Thummavichai, J. Wen, L. Zhang, N. Wang, Y. Xia, Multifunctional porous SiC nanowire scaffolds. *Journal of the European Ceramic Society* **41**, 3970-3979 (2021).
230. Q. Zhang, M. Hao, X. Xu, G. Xiong, H. Li, T. S. Fisher, Flyweight 3D graphene scaffolds with microinterface barrier-derived tunable thermal insulation and flame retardancy. *ACS applied materials & interfaces* **9**, 14232-14241 (2017).

231. Y. Liu, Y. Liu, W. C. Choi, S. Chae, J. Lee, B.-S. Kim, M. Park, H. Y. Kim, Highly flexible, erosion resistant and nitrogen doped hollow SiC fibrous mats for high temperature thermal insulators. *Journal of Materials Chemistry A* **5**, 2664-2672 (2017).
232. J.-W. Wu, W.-F. Sung, H.-S. Chu, Thermal conductivity of polyurethane foams. *International journal of heat and mass transfer* **42**, 2211-2217 (1999).
233. B. Wicklein, A. Kocjan, G. Salazar-Alvarez, F. Carosio, G. Camino, M. Antonietti, L. Bergström, Thermally insulating and fire-retardant lightweight anisotropic foams based on nanocellulose and graphene oxide. *Nature nanotechnology* **10**, 277-283 (2015).
234. S. Liu, J. Duvigneau, G. J. Vancso, Nanocellular polymer foams as promising high performance thermal insulation materials. *European polymer journal* **65**, 33-45 (2015).
235. J. Liu, P. Buahom, C. Lu, H. Yu, C. B. Park, Microscopic revelation of the solid–gas coupling and Knudsen effect on the thermal conductivity of silica aerogel with inter-connected pores. *Scientific Reports* **12**, 21034 (2022).
236. K. Swimm, G. Reichenauer, S. Vidi, H.-P. Ebert, Impact of thermal coupling effects on the effective thermal conductivity of aerogels. *Journal of Sol-Gel Science and Technology* **84**, 466-474 (2017).
237. F. Hu, S. Wu, Y. Sun, Hollow-structured materials for thermal insulation. *Advanced Materials* **31**, 1801001 (2019).
238. R. Prasher, Ultralow thermal conductivity of a packed bed of crystalline nanoparticles: A theoretical study. *Physical Review B* **74**, 165413 (2006).
239. X. J. Hu, R. Prasher, K. Lofgreen, Ultralow thermal conductivity of nanoparticle packed bed. *Applied Physics Letters* **91**, (2007).
240. S. Yoon, G. D. Han, D. Y. Jang, J. W. Kim, D. H. Kim, J. H. Shim, Fabrication of yttria-stabilized zirconia aerogel for high-performance thermal barrier coating. *Journal of Alloys and Compounds* **806**, 1430-1434 (2019).
241. D. Salmon, R. Tye, Pyroceram 9606, a certified ceramic reference material for high-temperature thermal transport properties: Part 1—material selection and characterization. *International Journal of Thermophysics* **31**, 338-354 (2010).
242. D. Salmon, R. Brandt, R. Tye, Pyroceram 9606, A certified ceramic reference material for high-temperature thermal transport properties: part 2—certification measurements. *International Journal of Thermophysics* **31**, 355-373 (2010).
243. M. Tychanicz-Kwiecień, J. Wilk, P. Gil, Review of high-temperature thermal insulation materials. *Journal of Thermophysics and heat transfer* **33**, 271-284 (2019).
244. Y. Asakuma, Y. Kanazawa, T. Yamamoto, Thermal radiation analysis of packed bed by a homogenization method. *International Journal of Heat and Mass Transfer* **73**, 97-102 (2014).
245. J. Schorne-Pinto, P. Chartrand, A. Barnabé, L. Cassayre, Thermodynamic and Structural Properties of $CuCrO_2$ and $CuCr_2O_4$: Experimental Investigation and Phase Equilibria Modeling of the Cu–Cr–O System. *The Journal of Physical Chemistry C* **125**, 15069-15084 (2021).
246. Z. Zhao, H. Xiang, F.-Z. Dai, Z. Peng, Y. Zhou, $(La0.2Ce0.2Nd_{0.2}Sm_{0.2}Eu_{0.2})_2Zr_2O_7$: A novel high-entropy ceramic with low thermal conductivity and sluggish grain growth rate. *Journal of Materials Science & Technology* **35**, 2647-2651 (2019).
247. N. Zhou, T. Hu, J. Huang, J. Luo, Stabilization of nanocrystalline alloys at high temperatures via utilizing high-entropy grain boundary complexions. *Scripta Materialia* **124**, 160-163 (2016).

248. S. Hou, X. Ma, Y. Shu, J. Bao, Q. Zhang, M. Chen, P. Zhang, S. Dai, Self-regeneration of supported transition metals by a high entropy-driven principle. *Nature communications* **12**, 5917 (2021).
249. A. Mehta, Y. H. Sohn, Fundamental core effects in transition metal high-entropy alloys:"High-entropy" and "sluggish diffusion" effects. *Diffusion Foundations* **29**, 75-93 (2021).
250. W. Kucza, J. Dąbrowa, G. Cieślak, K. Berent, T. Kulik, M. Danielewski, Studies of "sluggish diffusion" effect in Co-Cr-Fe-Mn-Ni, Co-Cr-Fe-Ni and Co-Fe-Mn-Ni high entropy alloys; determination of tracer diffusivities by combinatorial approach. *Journal of Alloys and Compounds* **731**, 920-928 (2018).
251. J. Dąbrowa, M. Zajusz, W. Kucza, G. Cieślak, K. Berent, T. Czeppe, T. Kulik, M. Danielewski, Demystifying the sluggish diffusion effect in high entropy alloys. *Journal of Alloys and Compounds* **783**, 193-207 (2019).
252. D. B. Miracle, O. N. Senkov, A critical review of high entropy alloys and related concepts. *Acta Materialia* **122**, 448-511 (2017).
253. J. Luo, N. Zhou, High-entropy grain boundaries. *Communications Materials* **4**, 7 (2023).
254. S. Zenkin, A. Gaydaychuk, A. Mitulinsky, S. Linnik, in *Proceedings of 8th International Congress on Energy Fluxes and Radiation Effects*. (2022), pp. 1014-1021.
255. R.-Z. Zhang, M. J. Reece, Review of high entropy ceramics: design, synthesis, structure and properties. *Journal of Materials Chemistry A* **7**, 22148-22162 (2019).
256. M. Ma, X. Hu, H. Meng, Z. Zhao, K. Chang, Y. Chu, High-entropy metal carbide nanowires. *Cell Reports Physical Science* **3**, (2022).
257. F. Liu, J. Wang, F. Wang, H. Liu, Q. Du, Y. Li, B. Chen, H. Gu, N. Yang, Battery thermal safety management with form-stable and flame-retardant phase change materials. *International Journal of Heat and Mass Transfer* **218**, 124764 (2024).